The Dissertation Committee for Eric Christopher Spivey Certifies that this is the approved version of the following dissertation:

Multiphoton Lithography of Mechanically and Functionally Tunable Hydrogels

Committee:

Jason B. Shear, Supervisor

Christine E. Schmidt, Co-Supervisor

Krishnendu Roy

Andrew K. Dunn

James W. Tunnell

Multiphoton Lithography of Mechanically and Functionally Tunable Hydrogels

by

Eric Christopher Spivey, B.S.E., M.S.E.

Dissertation

Presented to the Faculty of the Graduate School of

The University of Texas at Austin

in Partial Fulfillment

of the Requirements

for the Degree of

Doctor of Philosophy

The University of Texas at Austin

May 2012

Dedication

I dedicate this work to my wife, Wendy, who has been steadfast in her support and encouragement throughout the entirety of my studies; and to my parents, Christopher and Mary Ann, who instilled in me a love of learning, and encouraged my curiosity and skepticism in equal measure.

Acknowledgements

I would like to thank my advisor, Prof. Jason Shear, for all his support and guidance during my tenure at UT, and for giving me the freedom to become a self-sufficient and independent scholar. I would also like to thank my co-advisor, Prof. Christine Schmidt, for keeping me on track, and for her constant encouragement and faith in my abilities. I would like to thank the rest of my committee, Profs. Andrew Dunn, Krishnendu Roy and James Tunnell for their patience and valuable advice throughout all phases of my graduate education. I thank the alumnae of the Shear and Schmidt labs, especially Drs. Rex Nielson, Bryan Kaehr, Stephanie Seidlits and Eric Ritschdorff, without whom my work could not have been accomplished, and the current members of the labs, especially Jodi Connell, Derek Hernandez, Dr. Zin Khaing. Dr. John Hardy, Todd Hoppe, Maryam Ali, Mike Robinson and Sarah Stuart. Thanks also to the undergraduate researchers that helped me in my work, especially Chris McLennon. Finally, I would like to thank my financial supporters, especially Dr. Sam Y. Zamrik who has contributed generously to my work through the Cockrell School of Engineering Endowed Presidential Scholarship. Generous funding from the National Science Foundation, the Welch Foundation, the National Institutes of Health and the Department of Veteran's Affairs has also been greatly appreciated.

Multiphoton Lithography of Mechanically and Functionally Tunable Hydrogels

Publication No._____

Eric Christopher Spivey, Ph.D.

The University of Texas at Austin, 2012

Supervisor: Jason B. Shear

Co-Supervisor: Christine E. Schmidt

As one of the few 3D microfabrication techniques available to researchers, multiphoton lithography (MPL) has generated considerable interest in the scientific community. By allowing researchers to localize photochemistry to a femtoliter volume, MPL has permitted the fabrication of intricate, 3D microstructures from a range of materials, including protein hydrogels. MPL can be used to fabricate functional hydrogels on the scale of 100 μm, with features on the order of 1 μm. This dissertation examines existing MPL techniques to discover ways in which current processes can be modified to produce hydrogel products that are more useful for biomedical applications like tissue engineering. A new material is introduced that enables the fabrication of fully unconstrained hydrogel microstructures. In this context, A structure can be classified as "unconstrained" when it is free to translate and rotate without hindrance in three dimensions, and is not attached to the substrate or any other structure. New processes are

demonstrated that permit the fabrication of larger MPL hydrogels without sacrificing feature resolution. This allows the fabrication of millimeter-scale, high aspect ratio structures with features smaller than 10 μm. Methods are described for tuning and measuring the mechanical properties of MPL-fabricated hydrogels, and ways of tuning the functional properties of the hydrogels are also examined.

Table of Contents

List of Figures

Chapter 1: Introduction

As one of the few 3D microfabrication techniques available to researchers, multiphoton lithography (MPL) has generated considerable interest in the scientific community. By allowing researchers to localize photochemistry to a femtoliter volume element (voxel), MPL has permitted fabrication of intricate, 3D microstructures from a range of materials, including protein hydrogels [1, 2]. Other techniques, like stereolithography [3] can be used to fabricate microstructures from similar materials, however the minimum feature size of the resulting structures is greater than 10 μm due to fundamental limitations of the technique. Etching with focused beams of high-energy particles like electrons or ions produces structures with features on the order of 10 nm [4, 5], however these methods are only useful for the surface patterning of existing micron-scale structures. Deep reactive ion etching, which combines the capabilities of focused ion beam etching with the ability to penetrate the substrate to depths up to approximately 500 μm, allows milling of structures from a solid substrate [6]. However, this process has not been successfully applied using hydrogels.

MPL can be used to fabricate functional hydrogels on the scale of 100 μm, with features on the order of 1 μm. This dissertation examines existing MPL techniques to discover ways in which current processes can be modified to produce hydrogel products that are more useful for biomedical applications like tissue engineering. New processes are demonstrated that permit the fabrication of larger MPL hydrogels without sacrificing feature resolution. This allows the fabrication of millimeter-scale, high aspect ratio structures with features smaller than 10 μm. Methods are described for tuning and measuring the mechanical properties of MPL-fabricated hydrogels, and ways of tuning the functional properties of the hydrogels are also examined.

1.1 MULTIPHOTON LITHOGRAPHY

1.1.1 Covalent crosslinking using multiphoton excitation

Multiphoton excitation occurs when the energy state of a molecule transitions from the ground state to an excited state due to the absorption of two or more photons. This process is extremely rare under normal conditions, and is also subject to complex selection rules, so it is almost never observed naturally [7]. Since the probability of a two-photon interaction is dependent on the light intensity squared, one can achieve significant TPE by focusing pulsed laser light through high numerical aperture (NA) microscope objectives. Since very high photon densities are required, the best light sources are pulsed lasers with high (kJ) peak energy and femtosecond pulse durations. This allows the high photon flux needed, while keeping the average power of the laser at manageable (mW) levels.

Once excited, the photosensitizer relaxes to its ground state, releasing energy that can cause crosslinking between nearby molecules via one of two general mechanisms: Type I, in which the excited sensitizer reacts with the substrate or solvent to produce a free radical, or Type II, in which the sensitizer reacts with oxygen to create a singlet oxygen [8].

So far, there has been little direct chemical analysis of the crosslinked products of MPL, but it is hypothesized that the chemistry is similar to that which occurs during single photon, UV-excited crosslinking. Several studies have been conducted in this area, to help predict damage to tissue during photodynamic therapy. Working primarily with the photosensitizers rose bengal and flavin mononucleotide, members of the Kopaček lab studied copolymers of histidine (His), lysine (Lys), and tyrosine (Tyr), and concluded that the photooxidizable residues His and Tyr can form crosslinks with each other [9, 10] and with the non-photooxidizable residue Lys [9]. Furthermore, Tyr-Tyr bonds were

formed primarily through Type I reactions [10], and form at least three isoforms as products [11]. His-His was predominantly formed through Type II reactions [12]. Taken together, their results imply that between whole proteins, crosslinking interactions between amino acid residues are likely to be diverse and numerous.

Multiphoton lithography of biological hydrogels has been accomplished using several different proteins, including bovine serum albumin (BSA), avidin, lyzosyme, cytochrome-c [13], collagen [14], and fibronectin [15], and it is theoretically possible to use many other proteins.

In addition to proteins, polyethylene glycol diacrylate (PEGDA) has been used in multiphoton lithography [16], and there is reason to believe that other acrylated biopolymers could also be used. In Chapters 3 & 4, a methacrylated form of hyaluronic acid is combined in a precursor solution with either PEGDA or BSA, and the solutions are used to fabricate hybrid hydrogels.

1.1.2 Fabrication techniques

By scanning the focal volume through a solution of concentrated protein and a photosensitizer, researchers have fabricated hydrogels either by moving the microscope stage or scanning the laser through the precursor solution [17, 18]. By stepping the stage height or objective focus during beam scanning or stage scanning, some have also created 3-D blocks and suspended cables of matrix material [13, 18]. Most recently, dynamic photomasks have been employed with beam scanning to fabricate complex and detailed 3D hydrogel structures, using a simple computer-aided design (CAD) interface [1, 19].

The work described in the following chapters employs both stage scanning and beam scanning methods to generate raster patterns that are used to make more complicated structures. A brief description of each follows, along with a discussion of the

general limitations of each scan method. It should be noted that most recent MPL techniques combine some element of both scanning methods. For example, the dynamic masking technique described below in Paragraph 1.1.2.2 steps the stage along the optical axis in coordination with beam scanning in order to achieve layer-by-layer fabrication of 3D hydrogels. Other examples of this will be seen in Chapter 2.

1.1.2.1 Stage scanning method

The stage scanning method employs a microscope stage moved by programmable actuators, typically coupled with a computer-controlled shutter that is operated in coordination with the stage movement to selectively expose the precursor solution to the focused laser light (Figure 1.1). With the assistance of CAD programs, this method can be employed to generate complex 2D and 3D structures, depending on the sophistication of the stage hardware and programming [20, 21].

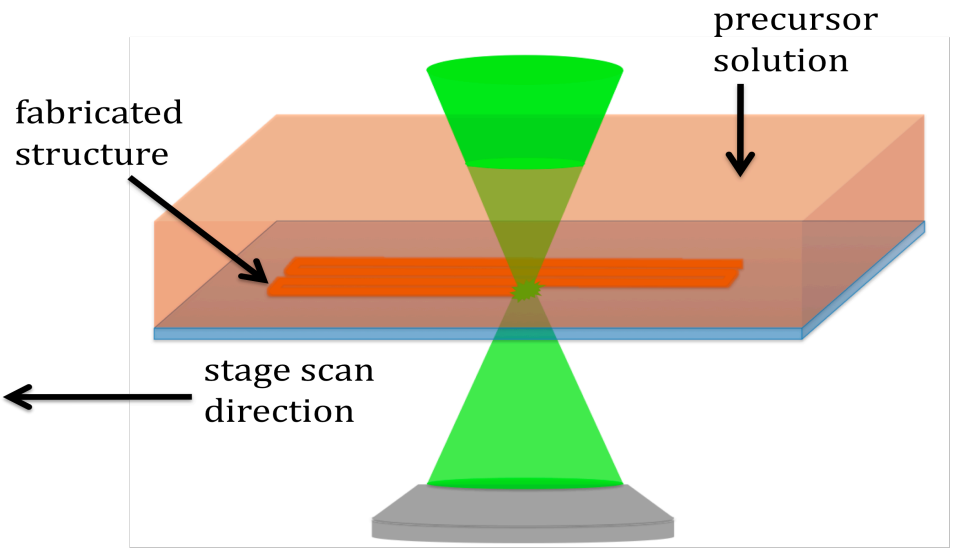

Figure 1.1 – Stage scanning fabrication method. Pulsed laser light (green) is focused through a high numerical aperture microscope objective (gray) into a precursor solution on a transparent substrate. The absorption of multiple photons by photosensitizers in the solution initiates crosslinking reactions between proteins in the solution, generating a solid hydrogel matrix in a focal volume centered on the focal point of the objective. When the microscope stage is scanned in a raster pattern, a solid block of hydrogel can be fabricated on the substrate.

The stage scanning method is very useful for making larger structures, since the size of a structure is only limited by the travel of the stage (which can be on the order of centimeters), and the time required for fabrication. Because stage scanning is normally much slower than beam scanning, scanning even very simple structures on the centimeter scale is a process of hours. Also worth considering is the cost of a scanning stage, which increases with the precision, travel, velocity, and the number of axes required.

1.1.2.2 Beam scanning method

The beam scanning method requires the use of a variable position mirror or mirrors, usually controlled by a pair of galvanometers, to scan the laser beam. In most configurations, a scan pattern is projected onto the surface of some intermediate optic (in

the simplest case, a mirror), where the surface of the optic is a conjugate plane of the focal plane of the objective. When this optic is aligned properly with the microscope objective, the scan pattern of the scanning mirror is translated into a solid object fabricated in the focal plane of the objective.

If the intermediate optic used is a digital micromirror device (DMD), a dynamic masking method can be employed (Figure 1.2). This technology was developed in the Shear lab [1, 22], and continues to be used to fabricate intricate 3D structures from a range of materials [1, 2]. Most of the structures fabricated for examination in the following chapters were fabricated using beam scanning coupled with dynamic masking.

Beam scanning is generally a more rapid fabrication method than stage scanning because galvanometers can scan a given area in the precursor solution more rapidly than most stage actuators. Also, beam scanning usually produces more homogenous structures, due to the absence of effects caused by stage motion artifacts (hysteresis, jitter, etc.). A disadvantage of beam scanning is the limited scale of the objects fabricated – typically no larger than the effective field of view of the objective.

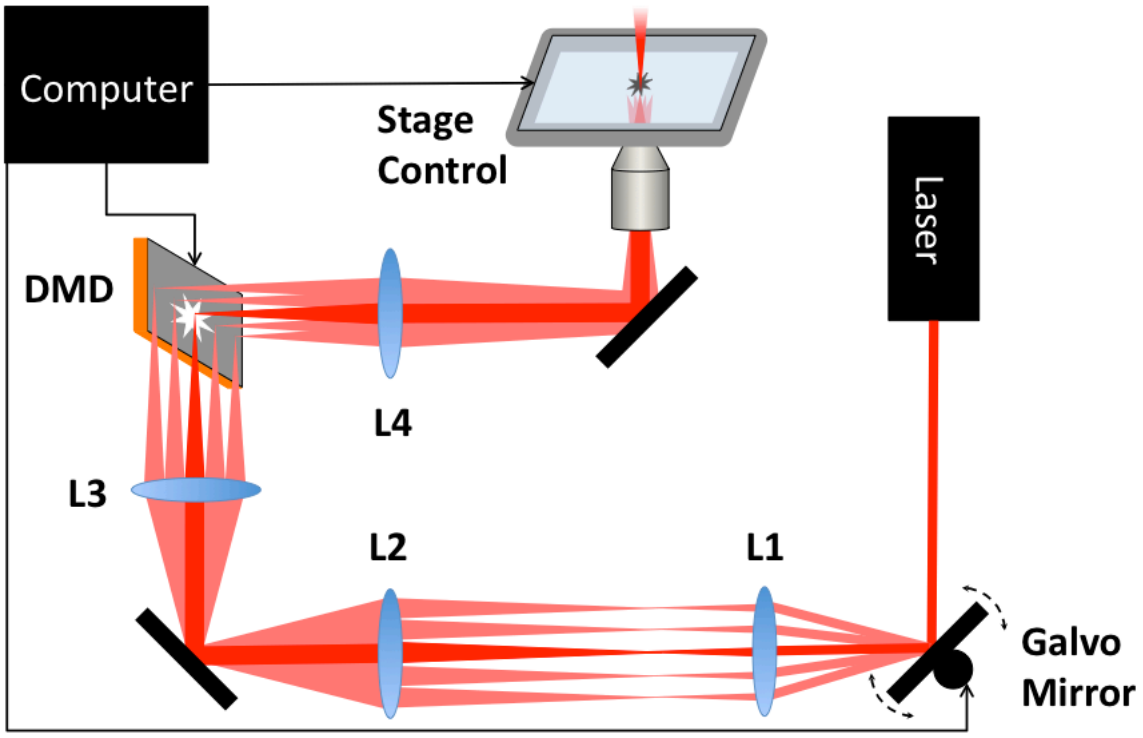

Figure 1.2 – Dynamic masking technique. A collimated beam from a pulsed laser is directed onto a galvanometer-driven oscillating mirror, and scans a raster pattern on lens L1. The placement of L1 – one focal length from the oscillating mirror, and the sum of focal lengths ($f_{L1}+f_{L2}$) from lens L2 – relays the raster pattern to L2 while simultaneously expanding the beam diameter (by f_{L2}/f_{L1}) and collimating the beam. Lens L3 is placed so that it is the sum of focal lengths ($f_{L2}+f_{L3}$) from L2, and one focal length from the DMD. While the beam diameter does not change between L2 and L3, the size of the raster scan is magnified (f_{L3}/f_{L2}) so that it overfills the DMD. Lens L3 relays the raster pattern and focuses the beam onto the DMD, allowing dynamic, virtual masking of the raster pattern. The white portions of the binary DMD mask reflect the focused beam onto lens L4. This lens is placed one focal length from the DMD, and one focal length from the back aperture of the objective. The objective focuses the beam into the precursor solution, and a micron-scale hydrogel is fabricated, a 1:1 replica of the shape displayed on the DMD. Computer coordination of the laser scanning parameters, DMD display, and stage height allow the fabrication of 3D microstructures.

1.2 MULTIPHOTON LITHOGRAPHY FOR TISSUE ENGINEERING*

Based on the limitations imposed by the available scan methods, significant challenges remain to be addressed before MPL can be of practical use in tissue engineering applications. On one hand, the stage scanning method may provide structures of an appropriate length, but the fabrication time are prohibitively long and the spatial resolution of the resulting structure may not be sufficiently small. On the other hand, using the beam scanning method may provide micron-scale topography, but the structures fabricated are only on the order of 100 μm long, far shorter than what is needed for tissue engineering.

Attempts have recently been made to address this problem. Ritschdorff et al. found that by scanning multiple laser beams and aligning them through the same objective, they could almost double the useable fabrication area in the objective field of view. By using an actuated stage with this augmented beam scan technique, the authors were able to fabricate large 2D structures (~210 μm by 135 μm) by automated tiling of the overlapping fabrication planes [23]. This combined stage and beam scan approach can be further developed to address the issues related to the application of MPL to the fabrication of peripheral nerve guides, and will be discussed more thoroughly in Chapter 2.

The problems associated with designing a more effective peripheral nerve guide provide a useful case study of the challenges that exist when designing materials that must interact with cells in a way that mimics their natural microenvironment. As such, the problems that are identified in the sections below can be applied more broadly to a range of biomedical applications.

---

* Section adapted from Spivey et al. **Biomaterials** 33(12). 2012.

Although a clear and compelling need exists for strategies that can restore motor and sensory nerves following injury, clinical technologies for promoting nerve regeneration remain limited [24]. Despite an improved understanding of the natural process of peripheral nerve regeneration and the availability of sophisticated biomaterials and fabrication techniques, no artificial nerve guide has been developed that approaches the "gold standard" for peripheral nervous system (PNS) repair, the autologous nerve graft ("autograft"). The autograft has been successful at effecting regeneration, but leaves patients with functional deficits caused by removal of the graft nerve from the donor site, particularly in cases where defects extend over several centimeters or more [25].

In an effort to avoid the problems associated with the autograft, several artificial nerve guides have been developed and approved for clinical use. In a recent review of these clinically approved nerve guides [26], the authors summarize criteria for an idealized guide based on the results of current research. Among the stated criteria, the authors conclude that the guide should be biocompatibile and nonimmunogenic, selectively biodegradable over the time period required for regeneration, flexible, soft, and semi-permeable. The most commonly used artificial nerve guide in clinical use is NeuraGen® (a product of Integra Lifesciences), which is a hollow, resorbable collagen tube. Although NeuraGen® meets the above-mentioned criteria, and is quite successful for short defects (< 20 mm) [27], it is limited in its utility for longer defects. As a result, artificial nerve guides like NeuraGen® are not a viable alternative for the autograft, except for short nerve defects.

The most successful clinical alternative to the autograft is a processed allograft*, Avance® (a product of AxoGen, Inc.) [26, 28], which uses (in part) a process to

* An *allograft* is tissue transplanted from a donor organism of the same species, a term needed in this context to differentiate the tissue from autograft tissue.

decellularize nerve tissue via a series of detergent washes [29]. The graft is unique because, while rendered acellular by the process, the microstructure of the extracellular matrix (ECM) remains relatively undisturbed after chemical processing [30]. This remaining microstructure is likely key to the success of the Avance® nerve graft. When compared to an allograft prepared using a different decellularization method (labeled "Sondell" in the graph [31]) that does not preserve the nano- and microstructure of the ECM, the "optimized acellular" (labeled "OA") graft with more preserved ECM supports the growth of significantly more neurons after 84 days [30]. It is important to note that the Sondell and optimized acellular allografts are nearly identical in terms of ECM composition – they only differ significantly in terms of the preservation of their micron-scale features.

As further evidence for the clinical requirement for cell-scale topography, it was found that the Avance® graft is better than NeuraGen®, but not as effective as the autograft. For both 14 mm and 28 mm defects, the Avance® allograft contained significantly more nerve fibers than the NeuraGen® graft at all time points examined. This relative success is attributed to the presence of mostly intact basal laminae in the Avance® allograft. Also, in a recent clinical study, 90% of patients (n = 26) receiving the Avance® allograft to repair nerve defects 30-50 mm long experienced meaningful recovery [28]. Nevertheless, when compared with fresh nerve, the Avance® graft does display noticeable disruptions that are attributed to the decellularization process [32]. Therefore, it is important to continue lines of investigation that will lead to an alternative scaffold to bridge nerve defects, particularly large nerve defects, where the Avance® graft may not be appropriate.

1.2.1 Overview of nerve injury and regeneration

Peripheral nerve injury (PNI) is a general term applied to a class of injuries that vary greatly in terms of their severity. Because less severe injuries do not usually require implants or surgery, we will only consider complete transection of the nerve trunk (Sunderland Grade 5) [33]. Following injuries of this kind, the initial physical response is clot formation, which stabilizes the injury and allows macrophages to remove dead tissue. Schwann cells then migrate from both the proximal and distal stumps to form a continuous band that bridges the defect [34]. Axonal sprouts then extend from the neuronal somata in the proximal stump, along the same general path as the Schwann cells, and reestablish contact with the distal stump. Schwann cells then re-myelinate the regenerated axon [35].

If the injury to the nerve is small (i.e., the gap between the two cut ends are <6 mm), regeneration occurs spontaneously when the nerve ends are sutured [36]. However, if the injury results in a larger gap (>6 mm), tension in the sutured nerve degrades the quality of regeneration. In this case, some type of "bridge" (usually an autologous graft or nerve guide) is needed in order to support functional recovery.

1.2.2 Role of basal laminae in PNS regeneration

A plausible explanation for the limited efficacy of current artificial nerve guides over longer distances is the absence of physical guidance for the cells at a relevant scale, that is, features that are cell-sized and smaller (< 50 μm). A good example of naturally occurring physical guidance at this scale is the Schwann cell basal lamina. This basal lamina consists of generally continuous tubes of laminin ~10 μm diameter, embedded in extracellular matrix (ECM). The laminae and ECM are the non-cell components that, together with Schwann cells and axons, comprise the endoneurium and form nerve fascicles.

Intact Schwann cell basal laminae appear to be critical for effective nerve regeneration. Research has shown (in a murine model) that when the structure of nerve tissue, including the basal laminae, is preserved during a crush-type axotomy, regenerating motor axons retrace their original pathways to re-establish neuromuscular junctions at the original sites with very little variation [37]. Other studies that support the importance of basal lamina-like guidance cues conclude that regenerating axons in rat spinal cord are more efficient when presented with smaller diameter tube structures [38], and that axons are generally sensitive to substrate curvature, demonstrating more directional extension when exposed to a smaller radius of curvature [39].

Based on this evidence, one can hypothesize that, as a prerequisite for efficient axon extension, the next generation nerve guides should incorporate cell-scale topography consisting of continuous, tube-like, micron-scale structures that are both linear and aligned over macroscopic distances. For the purposes of this work, microtopography is defined as physical features 100 nm - 50 μm. Although the primary interest in improving nerve guides is to enable functional repair in long defect (> 20 mm) scenarios, the inclusion of tube-like, cell-scale topography in scaffolds would also improve the speed and efficiency of nerve regeneration over shorter distances.

1.2.3 Effect of microtopography on nerve cell behavior

It is important to first consider some of the fundamental research on neurons and Schwann cells that point to the importance of microtopography on cell contact guidance, and how that influences nerve regeneration. *Contact guidance* is a term used to describe the influence of physical contact with an environmental object (typically another cell or feature of the extracellular matrix) on cell projection or movement. All evidence suggests that it plays an important role in both the development and repair of the PNS [40-43].

What this research can tell us about the limitations of effective contact guidance is of primary importance, both in terms of what kind of physical features affect cells, and also how time constraints may be affecting cell sensitivity to these features.

1.2.3.1 Importance of topography at a cellular level

Substrate topography can play a significant role on cell morphology and behavior, cell-substrate interaction, and cell-cell interactions [25, 44-47]. Effects of topography at all scales have been shown on many different cell types including cells of the central and peripheral nervous systems [25, 47, 48].

Recently, Hurtado et al. developed a platform consisting of ~1.5 μm diameter poly-L-lactic acid fibers organized in either aligned or in random configuration. These platforms were used as experimental substrates for neurons cultured from rodent dorsal root ganglia (DRG) [48]. The authors found that neurites from neurons grown on aligned fibers extended* to significantly greater distances (~1.7 mm) compared to randomly aligned fibers (~0.9 mm). Interestingly, the authors also examined whether the topography of any fibers (random or aligned) can make a difference in neurite extension by comparing neurite growth on both types of fibers with growth on PLA films. In this case, they found that on random fibers, DRG neurons produce a denser network of neurites than those cultured on films. However, the maximum extension distance reached by neurites was similar in both cases. This implies that neurites benefit from the presence of microtopography in terms of stimulating growth, but that only aligned substrates significantly improve the extension length. Also, it appears that although the path of DRG neurite growth is more circuitous on randomly aligned fibers compared to aligned

* In the context of this study, neuron "extension" is the straight line distance from the cell body to the end of the neurite, whereas neuron "length" is the length of a curve that follows the same path as the neurite from the cell body to the end of the neurite

fibers, the neurites themselves are of comparable length. So it is likely that aligned substrates do not inherently stimulate the growth of longer neurites, they simply maximize neurite extension by limiting or restricting the direction of axonal growth, ensuring more efficient growth and longer extension over a given time period.

It is evident then, that microtopography can act to increase the directional efficiency neurite extension. Taken on its own, this finding implies that scaffolds without aligned cell-scale topography should work as well as those with aligned topography, given enough time. Since that does not appear to be the case [Hsu, 2009], there must another feature of peripheral nerve regeneration that must be considered when evaluating the need for cell-scale topography in nerve guides.

1.2.3.2 Time limit on regeneration

The notion that neurons have time-limited regenerative capacity is not new [49]. "Conditioning lesion" is a paradigm in which a minor lesion to the peripheral nerve is performed before a major lesion or cut to the axons in the dorsal root region. This process results in a more accelerated regeneration [50]. This type of observation suggested to researchers that injury to the peripheral axons causes changes within the neuronal cell bodies of these neurons, which result in more accelerated axonal growth once the axons of the nerve are cut. This type of conditioning lesion has been used as a model to study intrinsic regenerative potential. Further conditioning lesion studies showed that inflammatory cells in the injured areas may enhance axonal regeneration [51], and that there may be a time limit in the conditioning lesion's ability to enhance axonal regeneration of central nervous system axons [52]. These results suggest that although conditioning lesions can increase intrinsic regenerative capacity of central axons, this effect is time dependent.

1.2.3.3 Implications for nerve guide design

Taken together, these two concepts – that microtopography increases neurite extension by improving directional efficiency, and that the regenerative capabilities of neurons are limited in duration – have profound implications. If the concepts are as broadly valid as the studies mentioned above suggest, appropriate cell-scale topography is not only important for achieving functional recovery, it becomes critical for any recovery as the nerve defect increases in length.

1.2.3.4 Current graft technologies

Current *in vivo* research on materials being considered for use in nerve guides offer some perspective on how the particular microtopography of the materials affects the efficiency and quality of functional recovery. Results of this research can be used to draw some general conclusions about which types of microtopography are most efficient at guiding axon extension.

Most experimental nerve grafts that include microtopography use bundles of aligned microfiliments, often inserted into a hollow conduit, to provide guidance for axons. Most commonly, this is accomplished using microfibers produced via extrusion [53], electrospinning [48] or by processing animal tissue [54]. Linear contact guidance, similar to that which is provided by microfibers, is important to all migratory cells. In their work with fibroblasts and epithelial cells, Doyle et al. demonstrated that cell motility mechanisms of linear migration were more similar to mechanisms involved with 3D migration than with 2D migration [55]. Furthermore, the most rapid cellular motility occurred when the cells were exposed to a linear environment. For a given fibronectin surface density, migration of human epidermal keratinocytes along a 1.5 μm wide line of fibronectin was three-fold faster than migration of the same cell type on fibronectin-coated glass. With this in mind, the use of aligned micron-scale fibers to provide

guidance cues to axons and Schwann cells in a scaffold seems a reasonable approach to repairing long defects. Many investigators have taken this approach [46, 54, 56], and some have reported significant improvement *in vivo* over nerve guides without guidance cues.

Considering the nature of packed fibers, while the fibers themselves serve to guide cells in the regenerating tissue, the axons extend (and Schwann cells migrate) into the voids between the fibers. Because the fibers are not perfectly aligned, the resulting voids do not form continuous tube-like spaces. Consequently, fewer axons would ultimately extend throughout the length of the nerve guide, and those that did would take longer to get there, in comparison to an autograft. Fibers, therefore, do not provide the ideal microtopography for axon extension.

One solution to this problem is to use micron-scale tubes instead of fibers to provide directional microtopography, but it is important that the tubes be of a relevant, cellular scale. Some recent research, which subdivided hollow conduits into multiple channels via membranes [57] or molded sub-conduits [58], found that these features offered no real benefit when compared to single channel conduits, after implantation in relatively short (<15 mm) rat sciatic nerve defects. However, the smallest channel in these studies was a sub-conduit that was 410 μm in diameter. From a cellular perspective, a channel of this size would be essentially the same as the lumen of a single channel conduit [39].

The value of having truly micron-scale tubes is more clearly shown in work by Toba et al. During their examination of long (80 mm) canine peroneal nerve defects, they found that polylactic acid conduits filled with a freeze-dried collagen sponge material coated with laminin worked as well as laminin-coated collagen fibers after 12 months [59]. However, axons at the distal end of both the fiber and sponge nerve guides were

smaller in diameter, with thinner myelin sheathes. Because functional recovery of the test animals was not formally evaluated, and no one has attempted to replicate the work using nerve defect lengths of such magnitude, it is difficult to gauge the full impact of the results. However, other studies with similar nerve guides also succeeded in restoring function over shorter distances [60, 61], so the collagen sponge approach may bear further study due to its simplicity and effectiveness.

Using a patented freeze-dry process that produces more ordered and oriented voids in collagen [62], several recent studies have demonstrated the value of the resulting micron-scale tubes using various neuronal cell types [63-67]. This experimental oriented collagen nerve guide, seeded with Schwann cells, was recently used by Bozkurt et al. to repair 20 mm defects in rat sciatic nerve. Within 6 weeks, the Schwann cell seeded graft was statistically identical to the autograft in terms of axon density, diameter, and myelination. This demonstrates the potential of a material that effectively combines nano- and microtopography to efficiently guide neurons across a peripheral nerve defect [68]. However, as the authors of this study point out in their conclusion, "it is important to realize that the ideal alternative for the autograft should perform better than the autograft." One area that could still be improved, which is illustrated in the results of the study, is the longitudinal continuity of the tubes along the full length of the nerve guide.

1.2.3.5 Lessons learned from in vivo research

The research reviewed here strengthens the hypothesis that tube-like microtopography increases the effectiveness of nerve guides; however, more direct evidence is available, data that show the specific value of intact basal laminae during regeneration. When Nguyen et al. compared the regeneration of axons after either a crush injury or transection, they noted that, compared to the crush injury, the transection was

correlated both with delayed axon regeneration and reduced specificity of the regenerating axons with respect to retracing their original path [37]. The authors hypothesize that this discrepancy may be related to the integrity of the endoneurial sheath (basal lamina), and that the disruption of this integrity in a cut nerve contributes to the observed delay in regeneration. In light of this finding, the microchannels in freeze-dried collagen sponge are less than ideal, because they are not continuous [66]. Nevertheless, this methodology does offer significant improvements over the other engineered nerve guides that are currently available.

1.2.4 Other design considerations for peripheral nerve guides

The topography of scaffold materials is of fundamental importance to cell behavior in most scenarios, and is a prerequisite for desired cell behavior in applications like peripheral nerve graft, as discussed above. However, other design characteristics such as the rigidity or chemical functionality of the substrate are of broad general importance, and must also be considered when attempting to engineer biomimetic cell scaffolds for any application.

1.2.4.1 Effect of Young's modulus on nerve cell behavior

The rigidity of a substrate, usually quantified in terms of either Young's modulus or shear modulus, can have a substantial impact on cell behavior. Research has shown that differentiation of neural progenitor cells into either neural or glial cells can be controlled by tuning the Young's modulus of the hydrogel substrate [69-71]. The range of hydrogel moduli used in these studies ranged from ~1-10 kPa, which is on the same order as neural tissue from the central nervous system. For many proposed peripheral nerve graft techniques that incorporate live cells [68, 72], differentiated Schwann cells are used,

so cell differentiation may not be of immediate concern. However, substrate modulus also appears to modulate axon extension.

The general finding has been that substrates with lower Young's modulus* ($E \approx 1$ kPa) allow neurons to extend longer axons. For example, neurons from the DRG of embryonic rat grown on a 870 Pa polyacrylamide substrate extend axons that are significantly longer than those grown on a 13 kPa substrate after 72 hours [73]. Likewise, axons from mouse hippocampal neurons grown on 500 Pa polyacrylamide gels are significantly longer than those grown on 4 or 7.5 kPa gels [74]. This generality is subject to limitations – neuron-like PC-12 cells grown on a 20 Pa polyacrylamide gel extended significantly shorter neurites than cells grown on 570 or 6000 Pa gels [75]. Also, sensitivity to softer substrates does not appear to extend to all neurons. Rat cortical neurons, for example, do not show significant differences in axon length for cells grown on acrylamide substrates ranging from 0.26-13 kPa [73]. These results suggest that caution should be employed when making generalizations about cellular responses to substrate modulus. Also, because the research here mentioned does not account for porosity, which is very difficult to quantify in hydrogels, additional caution must be exercised.

Although the modulus of peripheral nerve has been measured [76], the measurements were made on sections of whole nerve, and do not account for the existence of micron-scale variations in modulus implied by the intricate microanatomy of the tissue. While this type of holistic measurement may be valuable for other aspects of nerve guide design, it does not offer the best guide for determining the ideal modulus of a scaffold material at the cellular scale. In this case, at least, the data from the *in vitro*

* All following moduli are Young's moduli, in some cases values have been converted from shear moduli, assuming an elastic material.

experiments discussed above appears to offer better information for determining the design modulus of an experimental scaffold material.

1.2.4.2 Effect of chemical cues on nerve cell behavior

The importance of chemical cues to cell differentiation, migration, and almost any other aspect of cell behavior, cannot be overstated. Nerve cells are no exception, and are subject to a wide range of both ECM-bound and diffusible factors. With respect to diffusible factors, engineered scaffold materials must be designed in such a way as to allow controlled diffusion of these factors to the cells. Parameters of a hydrogel scaffold material that would most affect diffusion, such as the charge or hydrophilicity of the polymer used, or the pore size of the hydrogel, should be selected with care, but are usually easy to establish in such a way as to allow acceptable levels of factor diffusion to and from the cells. More difficult to accomplish is the appropriate placement of bound factors, which seem to be particularly important for cell migration and process extension. Various studies have reported increased glial migration speed and neuronal outgrowth in the presence of immobilized ECM components [77, 78]. Although the simple presence of these cues in a regeneration matrix can enhance outgrowth, there is strong evidence that gradients of certain bound factors also stimulate neurite outgrowth [79] and glial migration [80]. So far, these gradients have been linear only, predominantly created on 2D substrates. Although 2D models have been effective in clarifying some migratory behaviors, they often do not accurately recapitulate the more complex, *in vivo*, 3D environment of tissue [55]. Axon extension in particular is sensitive to a range of bound factors, the most important of which is laminin [81]. As discussed above, regenerating axons preferentially extend into intact basal laminae, which, in addition to the topographic features already discussed, are predominantly composed of laminin.

Therefore, as a design goal, cell scaffolds for a peripheral nerve guide should incorporate laminin or laminin derivatives into the material used. More ambitious approaches may seek to improve on natural tissue by discovering and exploiting any improvements to the rate axon extension brought on by selective 3D patterning of laminin or other bound factors.

1.3 Overview of Chapters

This chapter has been an introduction to multiphoton excitation and MPL, discussing general characteristics of MPL with respect to how it can be applied as a technique to fabricate scaffolds for tissue engineering applications, and some of the remaining challenges to implementation. It concluded with a brief overview of work that justifies the need for microtopography in peripheral nerve guides, and a review of other parameters critical to the effective guidance of neuronal cells like scaffold modulus and chemical functionality.

Chapter 2 will explore new MPL fabrication techniques that overcome some of the limitations discussed above. New techniques for controlling and integrating opto-mechanical components of the dynamic mask fabrication system will be introduced, as well as a novel material designed to fully exploit the inherent 3D capabilities of MPL. Preliminary results will be discussed based on current research, and remaining challenges will be addressed.

The mechanical properties of MPL-fabricated hydrogels will be discussed in Chapter 3. Cell behavior can be significantly influenced by the elasticity of the substrate; as a result, it is important to examine the elasticity of hydrogels fabricated for use in cell scaffolds. Techniques for tuning and measuring the Young's moduli of MPL-fabricated

hydrogels are explored, and results from experiments conducted on hybrid hydrogels using these techniques are presented.

Chapter 4 will introduce work on the micron-scale functionalization of hydrogels using multiphoton excitation. Chemical stimulation is still the most used, and in some ways best understood method for controlling the behavior of cells. Using a photolabile biotin conjugate, a functionalization technique that can produce arbitrary patterns of select chemicals on hydrogels is introduced and demonstrated on MPL-fabricated hydrogels.

In Chapter 5, a summary of the progress described in the earlier chapters will be presented, and questions suggested by the results will be posed to guide future work, along with some discussion of preliminary results for future work.

1.4 References

1. Nielson R., Kaehr B., Shear J.B., Microreplication and Design of Biological Architectures Using Dynamic-Mask Multiphoton Lithography. *Small* **5**, 120-125 (2009).
2. Ritschdorff E.T., Shear J.B., Multiphoton Lithography Using a High-Repetition Rate Microchip Laser. *Analytical Chemistry* **82**, 8733-8737 (2010).
3. Chan V., Jeong J.H., Bajaj P., Collens M., Saif T., Kong H., Bashir R., Multi-material bio-fabrication of hydrogel cantilevers and actuators with stereolithography. *Lab on a Chip* **12**, 88 (2012).
4. Rundqvist J., Hoh J.H., Haviland D.B., Directed immobilization of protein-coated nanospheres to nanometer-scale patterns fabricated by electron beam lithography of poly (ethylene glycol) self-assembled monolayers. *Langmuir* **22**, 5100-5107 (2006).
5. Hong Y., Krsko P., Libera M., Protein surface patterning using nanoscale PEG hydrogels. *Langmuir* **20**, 11123-11126 (2004).
6. Klaassen E.H., Petersen K., Noworolski J.M., Logan J., Maluf N.I., Brown J., Storment C., McCulley W., Kovacs G.T.A., Silicon fusion bonding and deep reactive ion etching: a new technology for microstructures. *Sensors and Actuators A: Physical* **52**, 132-139 (1996).
7. Shear J.B., Multiphoton-excited fluorescence in bioanalytical chemistry. *Analytical Chemistry* **71**, 598A-605A (1999).
8. Foote C.S., Definition of type I and type II photosensitized oxidation. *Photochemistry and Photobiology* **54**, 659-659 (1991).

9. Shen H.R., Spikes J.D., Kopečeková P., Kopeček J., Photodynamic crosslinking of proteins. I. Model studies using histidine-and lysine-containing N-(2-hydroxypropyl) methacrylamide copolymers. *Journal of Photochemistry and Photobiology B: Biology* **34**, 203-210 (1996).
10. Spikes J.D., Shen H.R., Kopečeková P., Kopeček J., Photodynamic crosslinking of proteins. III. Kinetics of the FMN- and rose bengal-sensitized photooxidation and intermolecular crosslinking of model tyrosine-containing N-(2-Hydroxypropyl)methacrylamide copolymers. *Photochemistry and Photobiology* **70**, 130-137 (1999).
11. Shen H.R., Spikes J.D., Smith C.J., Kopeček J., Photodynamic cross-linking of proteins V. Nature of the tyrosine-tyrosine bonds formed in the FMN-sensitized intermolecular cross-linking of N-acetyl-l-tyrosine. *Journal of Photochemistry & Photobiology, A: Chemistry* **133**, 115-122 (2000).
12. Shen H.R., Spikes J.D., Smith C.J., Kopeček J., Photodynamic cross-linking of proteins IV. Nature of the His-His bond (s) formed in the rose bengal-photosensitized cross-linking of N-benzoyl-L-histidine. *Journal of Photochemistry & Photobiology, A: Chemistry* **130**, 1-6 (2000).
13. Hill R.T., Shear J.B., Enzyme-Nanoparticle Functionalization of Three-Dimensional Protein Scaffolds. *Analytical Chemistry* **78**, 7022-7026 (2006).
14. Pitts J., Howell A., Taboada R., Banerjee I., Wang J., Goodman S., Campagnola P., New Photoactivators for Multiphoton Excited Three-dimensional Submicron Cross-linking of Proteins: Bovine Serum Albumin and Type 1 Collagen. *Photochemistry and Photobiology* **76**, 135-144 (2002).
15. Basu S., Campagnola P.J., Properties of crosslinked protein matrices for tissue engineering applications synthesized by multiphoton excitation. *Journal of Biomedical Materials Research Part B: Applied Biomaterials* **71**, 359-368 (2004).
16. Jhaveri S.J., McMullen J.D., Sijbesma R., Tan L.S., Zipfel W., Ober C.K., Direct three-dimensional microfabrication of hydrogels via two-photon lithography in aqueous solution. *Chemistry of Materials* **21**, 2003-2006 (2009).
17. Campagnola P.J., Delguidice D.M., Epling G.A., Hoffacker K.D., Howell A.R., Pitts J.D., Goodman S.L., 3-dimensional submicron polymerization of acrylamide by multiphoton excitation of xanthene dyes. *Macromolecules* **33**, 1511-1513 (2000).
18. Allen R., Nielson R., Wise D.D., Shear J.B., Catalytic three-dimensional protein architectures. *Analytical Chemistry* **77**, 5089-5095 (2005).
19. Khripin C.Y., Brinker C.J., Kaehr B., Mechanically tunable multiphoton fabricated protein hydrogels investigated using atomic force microscopy. *Soft Matter* **6**, 2842-2848 (2010).
20. Kuebler S.M., Rumi M., Watanabe T., Braun K., Cumpston B.H., Heikal A.A., Erskine L.L., Thayumanavan S., Barlow S., Marder S.R., Perry J.W., Optimizing Two-Photon Initiators and Exposure Conditions for Three-Dimensional Lithographic Microfabrication. *Journal of Photopolymer Science and Technology* **14**, 657-668 (2001).

21. Li L., Gattass R.R., Gershgoren E., Hwang H., Fourkas J.T., Achieving λ/20 Resolution by One-Color Initiation and Deactivation of Polymerization. *Science*, (2009).
22. Kaehr B., Shear J.B., Mask-directed multiphoton lithography. *Journal of the American Chemical Society* **129**, 1904-1905 (2007).
23. Ritschdorff E.T., Nielson R.Y., Shear J.B., Multifocal Multiphoton Lithography. *Lab on a Chip* **12**, 867-871 (2012).
24. Schlosshauer B., Dreesmann L., Schaller H.-E., Sinis N., Synthetic Nerve Guide Implants in Humans: A Comprehensive Survey. *Neurosurgery* **59**, 740-748 (2006).
25. Schmidt C.E., Leach J.B., Neural tissue engineering: Strategies for repair and regeneration. *Annual Review of Biomedical Engineering* **5**, 293-347 (2003).
26. Kehoe S., Zhang X.F., Boyd D., FDA approved guidance conduits and wraps for peripheral nerve injury: A review of materials and efficacy. *Injury* **In Press**, 1-20 (2011).
27. Wangensteen K.J., Kalliainen L.K., Collagen Tube Conduits in Peripheral Nerve Repair: A Retrospective Analysis. *Hand* **5**, 273-277 (2009).
28. Brooks D.N., Weber R.V., Chao J.D., Rinker B.D., Zoldos J., Robichaux M.R., Ruggeri S.B., Anderson K.A., Bonatz E.E., Wisotsky S.M., Cho M.S., Wilson C., Cooper E.O., Ingari J.V., Safa B., Parrett B.M., Buncke G.M., Processed nerve allografts for peripheral nerve reconstruction: A multicenter study of utilization and outcomes in sensory, mixed, and motor nerve reconstructions. *Microsurgery* **32**, 1-14 (2011).
29. Hudson T.W., Liu S.Y., Schmidt C.E., Engineering an improved acellular nerve graft via optimized chemical processing. *Tissue Engineering* **10**, 1346-1358 (2004).
30. Hudson T.W., Zawko S., Deister C., Lundy S., Hu C.Y., Lee K., Schmidt C.E., Optimized Acellular Nerve Graft Is Immunologically Tolerated and Supports Regeneration. *Tissue Engineering* **10**, 1641-1651 (2004).
31. Sondell M., Lundborg G., Kanje M., Regeneration of the rat sciatic nerve into allografts made acellular through chemical extraction. *Brain Research* **795**, 44-54 (1998).
32. Whitlock E.L., Tuffaha S.H., Luciano J.P., Yan Y., Hunter D.A., Magill C.K., Moore A.M., Tong A.Y., Mackinnon S.E., Borschel G.H., Processed allografts and type I collagen conduits for repair of peripheral nerve gaps. *Muscle & Nerve* **39**, 787-799 (2009).
33. Sunderland S., A classification of peripheral nerve injuries producing loss of function. *Brain : a journal of neurology* **74**, 491-516 (1951).
34. Perry V.H., Brown M.C., Gordon S., The macrophage response to central and peripheral nerve injury. A possible role for macrophages in regeneration. *The Journal of Experimental Medicine* **165**, 1218-1223 (1987).

35. Deumens R., Bozkurt A., Meek M.F., Marcus M.A.E., Joosten E.A.J., Weis J., Brook G.A., Repairing injured peripheral nerves: Bridging the gap. *Progress in Neurobiology* **92**, 245-276 (2010).
36. Sunderland I.R.P., Brenner M.J., Singham J., Rickman S.R., Hunter D.A., Mackinnon S.E., Effect of Tension on Nerve Regeneration in Rat Sciatic Nerve Transection Model. *Annals of Plastic Surgery* **53**, 382 (2004).
37. Nguyen Q.T., Sanes J.R., Lichtman J.W., Pre-existing pathways promote precise projection patterns. *Nature Neuroscience* **5**, 861-867 (2002).
38. Krych A.J., Rooney G.E., Chen B., Schermerhorn T.C., Ameenuddin S., Gross L., Moore M.J., Currier B.L., Spinner R.J., Friedman J.A., Yaszemski M.J., Windebank A.J., Relationship between scaffold channel diameter and number of regenerating axons in the transected rat spinal cord. *Acta Biomaterialia* **5**, 2551-2559 (2009).
39. Smeal R.M., Rabbitt R., Biran R., Tresco P.A., Substrate Curvature Influences the Direction of Nerve Outgrowth. *Annals of Biomedical Engineering* **33**, 376-382 (2005).
40. Dodd J., Jessell T.M., Axon guidance and the patterning of neuronal projections in vertebrates. *Science* **242**, 692-699 (1988).
41. Culotti J.G., Kolodkin A.L., Functions of netrins and semaphorins in axon guidance. *Current Opinion in Neurobiology* **6**, 81-88 (1996).
42. Kuan C.Y.K., Tannahill D., Cook G.M.W., Keynes R.J., Somite polarity and segmental patterning of the peripheral nervous system. *Mechanisms of Development* **121**, 1055-1068 (2004).
43. Parker R.J., Auld V.J., Signaling in glial development: differentiation migration and axon guidance. *Biochemistry and Cell Biology* **82**, 694-707 (2004).
44. Brown R.A., Phillips J.B., Cell responses to biomimetic protein scaffolds used in tissue repair and engineering. *International Review of Cytology* **262**, 75-150 (2007).
45. Gomez N., Lu Y., Chen S., Schmidt C.E., Immobilized nerve growth factor and microtopography have distinct effects on polarization versus axon elongation in hippocampal cells in culture. *Biomaterials* **28**, 271-284 (2007).
46. Cao J., Sun C., Zhao H., Xiao Z., Chen B., Gao J., Zheng T., Wu W., Wu S., Wang J., Dai J., The use of laminin modified linear ordered collagen scaffolds loaded with laminin-binding ciliary neurotrophic factor for sciatic nerve regeneration in rats. *Biomaterials* **32**, 3939-3948 (2011).
47. Hoffman-Kim D., Mitchel J.A., Bellamkonda R.V., Topography, Cell Response, and Nerve Regeneration. *Annual Review of Biomedical Engineering* **12**, 203-231 (2010).
48. Hurtado A., Cregg J.M., Wang H.B., Wendell D.F., Oudega M., Gilbert R.J., McDonald J.W., Robust CNS regeneration after complete spinal cord transection using aligned poly-l-lactic acid microfibers. *Biomaterials* **32**, 6068-6079 (2011).
49. Richardson P.M., Issa V.M., Peripheral injury enhances central regeneration of primary sensory neurones. *Nature* **309**, 791-793 (1984).

50. Richardson P.M., Verge V.M.K., Axonal regeneration in dorsal spinal roots is accelerated by peripheral axonal transection. *Brain Research* **411**, 406-408 (1987).
51. Lu X., Richardson P.M., Inflammation near the nerve cell body enhances axonal regeneration. *The Journal of Neuroscience* **11**, 972-978 (1991).
52. Forman D.S., McQuarrie I.G., Labore F.W., Wood D.K., Stone L.S., Braddock C.H., Fuchs D.A., Time course of the conditioning lesion effect on axonal regeneration. *Brain Research* **182**, 180-185 (1980).
53. Long Y., Zhang N., Huang Y., Wen X., Formation of Highly Aligned Grooves on Inner Surface of Semipermeable Hollow Fiber Membrane for Directional Axonal Outgrowth. *Journal of Manufacturing Science and Engineering* **130**, 021011 (2008).
54. Yoshii S., Oka M., Shima M., Taniguchi A., Akagi M., Bridging a 30-mm nerve defect using collagen filaments. *Journal of Biomedical Materials Research Part B: Applied Biomaterials* **67A**, 467-474 (2003).
55. Doyle A.D., Wang F.W., Matsumoto K., Yamada K.M., One-dimensional topography underlies three-dimensional fibrillar cell migration. *The Journal of Cell Biology* **184**, 481-490 (2009).
56. Corey J.M., Lin D.Y., Mycek K.B., Chen Q., Samuel S., Feldman E.L., Martin D.C., Aligned electrospun nanofibers specify the direction of dorsal root ganglia neurite growth. *Journal of Biomedical Materials Research Part B: Applied Biomaterials* **83A**, 636-645 (2007).
57. Clements I.P., Kim Y.-t., English A.W., Lu X., Chung A., Bellamkonda R.V., Thin-film enhanced nerve guidance channels for peripheral nerve repair. *Biomaterials* **30**, 3834-3846 (2009).
58. Yao L., de Ruiter G.C.W., Wang H., Knight A.M., Spinner R.J., Yaszemski M.J., Windebank A.J., Pandit A., Controlling dispersion of axonal regeneration using a multichannel collagen nerve conduit. *Biomaterials* **31**, 5789-5797 (2010).
59. Toba T., Nakamura T., Shimizu Y., Matsumoto K., Ohnishi K., Fukuda S., Yoshitani M., Ueda H., Hori Y., Endo K., Regeneration of canine peroneal nerve with the use of a polyglycolic acid-collagen tube filled with laminin-soaked collagen sponge: a comparative study of collagen sponge and collagen fibers as filling materials for nerve conduits. *Journal of Biomedical Materials Research Part B: Applied Biomaterials* **58**, 622-630 (2001).
60. Nakamura T., Inada Y., Fukuda S., Yoshitani M., Nakada A., Itoi S.-i., Kanemaru S.-i., Endo K., Shimizu Y., Experimental study on the regeneration of peripheral nerve gaps through a polyglycolic acid-collagen (PGA-collagen) tube. *Brain Research* **1027**, 18-29 (2004).
61. Ichihara S., Inada Y., Nakada A., Endo K., Azuma T., Nakai R., Tsutsumi S., Kurosawa H., Nakamura T., Development of New Nerve Guide Tube for Repair of Long Nerve Defects. *Tissue Engineering Part C: Methods* **15**, 387-402 (2009).

62. Schoof H., Apel J, Heschel I., Rau G., Control of pore structure and size in freeze-dried collagen sponges. *Journal of Biomedical Materials Research Part B: Applied Biomaterials* **58**, 352-357 (2001).
63. Bozkurt A., Brook G.A., Möllers S., Lassner F., Sellhaus B., Weis J., Wöltje M., Tank J., Beckmann C., Fuchs P., Damink L.O., Schügner F., Heschel I., Pallua N., In Vitro Assessment of Axonal Growth Using Dorsal Root Ganglia Explants in a Novel Three-Dimensional Collagen Matrix. *Tissue Engineering* **13**, 2971-2979 (2007).
64. Bozkurt A., Deumens R., Beckmann C., Olde Damink L., Schügner F., Heschel I., Sellhaus B., Weis J., Jahnen-Dechent W., Brook G.A., In vitro cell alignment obtained with a Schwann cell enriched microstructured nerve guide with longitudinal guidance channels. *Biomaterials* **30**, 169-179 (2009).
65. Möllers S., Heschel I., Damink L.H.H.O., Schügner F., Deumens R., Müller B., Bozkurt A., Nava J.G., Noth J., Brook G.A., Cytocompatibility of a Novel, Longitudinally Microstructured Collagen Scaffold Intended for Nerve Tissue Repair. *Tissue Engineering Part A* **15**, 461-472 (2009).
66. Führmann T., Hillen L.M., Montzka K., Wöltje M., Brook G.A., Cell-Cell interactions of human neural progenitor-derived astrocytes within a microstructured 3D-scaffold. *Biomaterials* **31**, 7705-7715 (2010).
67. Hu X., Huang J., Ye Z., Xia L., Li M., Lv B., Shen X., Luo Z., A Novel Scaffold with Longitudinally Oriented Microchannels Promotes Peripheral Nerve Regeneration. *Tissue Engineering Part A* **15**, 3297-3308 (2009).
68. Bozkurt A., Lassner F., O'Dey D., Deumens R., Böcker A., Schwendt T., Janzen C., Suschek C.V., Tolba R., Kobayashi E., Sellhaus B., Tholl S., Eummelen L., Schügner F., Olde Damink L., Weis J., Brook G.A., Pallua N., The role of microstructured and interconnected pore channels in a collagen-based nerve guide on axonal regeneration in peripheral nerves. *Biomaterials* **33**, 1363-1375 (2012).
69. Saha K., Keung A.J., Irwin E.F., Li Y., Little L., Schaffer D.V., Healy K.E., Substrate modulus directs neural stem cell behavior. *Biophysical Journal* **95**, 4426-4438 (2008).
70. Banerjee A., Arha M., Choudhary S., Ashton R.S., Bhatia S.R., Schaffer D.V., Kane R.S., The influence of hydrogel modulus on the proliferation and differentiation of encapsulated neural stem cells. *Biomaterials* **30**, 4695-4699 (2009).
71. Seidlits S.K., Khaing Z.Z., Petersen R.R., Nickels J.D., Vanscoy J.E., Shear J.B., Schmidt C.E., The effects of hyaluronic acid hydrogels with tunable mechanical properties on neural progenitor cell differentiation. *Biomaterials* **31**, 3930-3940 (2010).
72. Lohmeyer J.A., Shen Z.L., Walter G.F., Berger A., Bridging extended nerve defects with an artifcial nerve graft containing Schwann cells pre-seeded on polyglactin filaments. *International journal of artificial organs* **30**, 64-74 (2007).
73. Norman L.L., Aranda-Espinoza H., Cortical Neuron Outgrowth is Insensitive to Substrate Stiffness. *Cellular and Molecular Bioengineering* **3**, 398-414 (2010).

74. Kostic A., Sap J., Sheetz M.P., RPTPalpha is required for rigidity-dependent inhibition of extension and differentiation of hippocampal neurons. *Journal of Cell Science* **120**, 3895-3904 (2007).
75. Leach J.B., Brown X.Q., Jacot J.G., Dimilla P.A., Wong J.Y., Neurite outgrowth and branching of PC12 cells on very soft substrates sharply decreases below a threshold of substrate rigidity. *Journal of Neural Engineering* **4**, 26-34 (2007).
76. Borschel G.H., Kia K.F., Kuzon W.M., Dennis R.G., Mechanical properties of acellular peripheral nerve. *Journal of Surgical Research* **114**, 133-139 (2003).
77. Anton E.S., Weskamp G., Reichardt L.F., Matthew W.D., Nerve growth factor and its low-affinity receptor promote Schwann cell migration. *Proceedings of the National Academy of Sciences* **91**, 2795 (1994).
78. Bailey S.B., Eichler M.E., Villadiego A., Rich K.M., The influence of fibronectin and laminin during Schwann cell migration and peripheral nerve regeneration through silicon chambers. *Journal of Neurocytology* **22**, 176-184 (1993).
79. Dertinger S.K.W., Jiang X., Li Z., Murthy V.N., Whitesides G.M., Gradients of substrate-bound laminin orient axonal specification of neurons. *Proceedings of the National Academy of Sciences* **99**, 12542-12547 (2002).
80. McCarthy J.B., Palm S.L., Furcht L.T., Migration by haptotaxis of a Schwann cell tumor line to the basement membrane glycoprotein laminin. *Journal of Cell Biology* **97**, 772 (1983).
81. Wang G.Y., Hirai K.I., Shimada H., The Role of Laminin, a Component of Schwann-Cell Basal Lamina, in Rat Sciatic-Nerve Regeneration Within Antiserum-Treated Nerve Grafts. *Brain Research* **570**, 116-125 (1992).

Chapter 2: Engineered microtopography of hydrogels fabricated using multiphoton lithography*

2.1 INTRODUCTION

The fabrication of micron-scale engineered materials is crucial in fields as diverse as optics [1], semiconductor design [2], and cell biology [3]. Although recent progress in these fields has been dramatic, most techniques cannot produce structures with micron-scale resolution in all three spatial dimensions. Also, many techniques are only compatible with a small number of materials, which limits the possible range of mechanical and functional properties.

Hydrogels are a useful class of materials with a wide range of biomedical applications including drug delivery [4], tissue engineering [5] and bacterial biology [6]. Recent research to functionalize [7] and tune the modulus [8] and transport properties [9] of hydrogels further extends their potential usefulness for biomedical applications. Currently, most macroscopic hydrogels are fabricated via wide-field photochemical [10] or chemical crosslinking [11], or thermal gelling [12]. While techniques exist for generating micron scale features using these gels [13, 14], none offers the possibility of explicitly designing these features in 3D. Processing hydrogels via wet lithography techniques such as stamping or injection molding have been used to fabricate micron-scale hydrogel structures [15, 16], but these methods cannot produce unattached hydrogel structures, or structures with enclosed voids or overhangs. Electrospinning and extrusion

* Adapted from EC Spivey, ET Ritschdorff, JL Connell, CA McLennon, CE Schmidt and JB Shear **Advanced Functional Materials** (in review). 2012. ETR built the fabrication instrument and aided in experimental design. JLC performed bacterial culture experiments. CAM provided technical assistance for select experiments. CES is the author's academic co-advisor, she offered supervisory support. JBS is the author's academic advisor, he provided guidance on the selection of experiments and extensive editorial support.

methods have been used to fabricate hydrogel cell scaffolds [17, 18], but these methods can only be used to fabricate filaments of specific diameter and orientation.

It has been shown that intricate, micron-scale hydrogel structures can be fabricated using multiphoton lithography (MPL) [19], and that these structures can be used to influence cellular microenvironments [20, 21]. Unlike most other photolithographic methods, MPL offers the ability to fabricate truly three-dimensional micron-scale structures with sub-micron features [22]. Most MPL techniques require that structures be fabricated from the surface of the substrate. This is necessary because in liquid precursor solutions, significant drift of fabricated solids can occur in the time required to fabricate a single layer. The resulting microstructures are therefore constrained to certain shapes and orientations.

Nevertheless, some investigators have successfully used multiphoton lithography to fabricate partially constrained microstructures (e.g., spinning gears on a spindle) from acrylic resin solutions that have high inherent viscosities [23, 24]. In another approach, Kuebler et al. found that careful combination of specific acrylic polymers dissolved in dioxane and then allowed to set by slow evaporation (over 72 hours) produced a solid precursor film. During fabrication, this film allowed no movement of layers as they were fabricated, permitting the creation of partially constrained objects. After fabrication, the film was dissolved with dimethylformamide, leaving the fabricated structure. Using this method, they were able to fabricate linked chain structures [25].

In this chapter, an MPL method is introduced that uses a controlled drying process to produce a solid, un-crosslinked protein hydrogel, or "protogel". The protogel provides a medium that enables the fabrication of unconstrained and partially constrained*

* A structure can be classified as "unconstrained" when it is free to translate and rotate without hindrance in three dimensions, and is not attached to the substrate or any other structure. A structure is classified as

crosslinked hydrogel microstructures via 3D laser scanning. The protogel is mechanically stable enough that it allows unsupported layer-by-layer assembly of microstructures. Several different proteins have been used to make protogels; when tested, functionality of the proteins does not appear to be considerably affected.

The ability to fabricate such structures from proteins rather than resins represents a significant step in how they can interact with biological systems. In particular, the ability to fabricate complex microstructures that are independent of the substrate provides the possibility for creating objects that could be useful as therapeutic devices. For example, macrophages clear microparticles from circulation via phagocytosis, which is an obstacle to drug delivery in some cases [26]. However, recent research has shown that particle shape significantly influences the rate of phagocytosis [27]. It is therefore reasonable to propose that by optimizing the shape of a particle used for drug delivery, one could extend the circulating half-life of the encapsulated drug. In other cases, it may be desirable to target macrophages for drug delivery, as they are key constituents in some disease states [26]. In this case, particles could be optimized for rapid phagocytosis to deliver drugs directly to the macrophage.

In the context of developing a scaffold material for peripheral nerve guides, protogels offer the ability to fabricate structures without embedding them in lower-density hydrogels, as was the case in Seidlits et al. [21]. However, there is still the problem associated with fabricating structures that are long enough (centimeter-scale) to be useful in peripheral nerve guides while maintaining the necessary micron-scale resolution required for effective interaction with the neurons and Schwann cells. As discussed in Chapter 1, others in the Shear lab have partially addressed this problem by

---

"partially constrained" if, as an independent structure, it is constrained by linkage with its neighbor and, ultimately, the substrate.

tiling and stacking 2D substructures to make larger 2D and 3D objects [28]. This is a conceptually simple solution, but in practice requires difficult coordination and calibration of movement on all stage axes. Moreover, the resulting objects can have noticeable seams where the substructures overlap; these defects could potentially interrupt the continuity of structures when they are millimeters or centimeters long. A solution demonstrated here partially dispenses with the need for substructures allowing one to fabricate layer-by-layer 3D structures with very high aspect ratio (~100:1) features. This approach makes MPL a more viable fabrication method for a wider range of biomedical applications, including peripheral nerve guidance.

2.2 MATERIALS AND METHODS

2.2.1 Protogel preparation

A 20 mM HEPES (L6876, Sigma) buffered saline (HBS) solution containing 100 mM NaCl (buffered to pH 7.3) was prepared as a solvent for the precursor solution. A concentrated solution of either 25 mM rose bengal (330000, Aldrich), 25 mM eosin (230251, Aldrich) or 15 mM methylene blue (M9140, Sigma-Aldrich) was prepared in DMSO (less than 4% H_2O, confirmed by refractometry [29]) and added to HBS so that the final weight percentage of DMSO was 21%* after the addition of protein. Lyophilized BSA (BAH-64, Equitech-Bio) was then added dry to the photosensitizer solution at a weight percentage of 29%. In some experiments, lyophilized avidin (A887, Molecular Probes) or lysozyme (L6876, Sigma) was used instead of BSA. Samples were left on a rotating mixer for up to 12 hours to ensure complete dissolution of the protein. Some BSA protogels were made using a precursor solution that contained 5% biotin-BSA

* All following percentages represent the weight of the stated solute divided by the weight of the solution (w/w) x 100%, unless otherwise noted

conjugate (b-BSA) and 24% unlabeled BSA, which provided the ability to fabricate avidin-binding BSA microstructures. The b-BSA was conjugated from BSA and biotin-succinimidyl ester (M0785, Marker Gene Technologies Inc.) using standard protocols from the manufacturer. For some experiments, 700 Da polyethylene glycol diacrylate (PEGDA, Aldrich 455008) was also added to BSA solutions, to a final weight percentage of 5%. In these experiments, the weight percentage of BSA was reduced to 24%.

Discs of cured polydimethylsiloxane (PDMS), 1 mm thick 1 cm in diameter, with 8mm diameter center holes, were used as wells to hold the precursor solution. The wells were cleaned thoroughly using a glass detergent, then dried and adhered to either #0 or #1 thickness coverslip. A micropipette was used to load 15-20 μL of precursor solution into the well on the coverslip. The coverslip with the solution was then placed into a drying chamber and the solution was allowed to dry for 10-15 minutes under a constant flow (~20 mL s^{-1}) of dry nitrogen. The drying chamber consisted of a 50 mL plastic test tube with an entrance port drilled to admit a flexible hose connected to a calibrated, controlled source of dry nitrogen. The cap of the tube was drilled with five 2 mm diameter holes to allow nitrogen to leave the chamber. In some cases, in order to calculate the final weight percentage of BSA and DMSO in the protogel, the precursor solution was weighed before drying and compared with the protogel weight after drying. After drying, the wells containing the protogel were covered with 1 cm diameter circular coverslips to prevent additional drying during fabrication.

2.2.2 Dynamic mask multiphoton lithography

The dynamic mask-based MPL technique used in this chapter is described in detail in Ritschdorff et al. [30]. The system described in that study produced overlapping laser scan fields – in this chapter only one scan field was used. Figure 1.2 in the previous

chapter illustrates the process. Briefly, the collimated output beam of a mode-locked titanium:sapphire laser, tuned to 740 nm (Coherent Mira 900), was focused onto an electrically actuated scan mirror that scanned the beam in a raster pattern through a series of lenses onto a 800 x 600 (SVGA) digital micromirror device (DMD). The DMD was controlled by a computer displaying binary mask images, where micromirrors on the DMD corresponding to the white pixels of the mask image directed the beam into the back aperture of a 100X (1.3 NA) Zeiss Fluar oil microscope objective. Due to this selective exposure, only the areas of the focal plane corresponding to the white areas of the mask resulted in photocrosslinking within the protogel. Three-dimensional objects were fabricated inside the protogel in a layer-by-layer process, by coordinating optical axis step movements of the stage with changes in mask presentation.

The average laser power was adjusted using a half-wave plate/polarizer pair to provide 15-25 mW at the back aperture of the objective. The raster scan was established to generate a fast-axis (x-axis) scan velocity of ~ 7 mm s^{-1}, and a slow-axis (y-axis) velocity of ~6 μm s^{-1}. Relative scan speeds were selected so that the lines of crosslinked protein overlapped to produce a continuous plane. Both the raster scan and optical axis stage movements were controlled and coordinated by a computer using LabView (v 8.2, National Instruments).

Digital masks for each layer were generated by slicing 3D rendered virtual objects using ImageJ software (v 1.44o, Wayne Rasband, Natl. Inst. Health). The 3D rendered objects were typically generated using the ImageJ macro language (http://rsbweb.nih.gov/ij/developer/macro/macros.html). The masks were organized as a stack of images in which each consecutive image represented a sequential layer of the desired structure. In the plane of the mask, an 8-pixel distance on the DMD corresponded to 1 μm in the structure. Each image in the mask represented a 0.33 μm or 0.5 μm slice of

the structure (depending on the desired optical axis resolution). The stage was three-axis translational stage (model 562, Newport) driven by motorized actuators (model LTA-HS and model ESP300 motion controller/driver, Newport).

Rehydration of all protogels was accomplished by applying 50 μL of HBS to the top surface of the protogel. After 10 minutes at room temperature, the rehydrated solution was removed using a micropipette, and the structures were rinsed 10 times with 50 μL HBS.

Structures fabricated from protogels containing b-BSA were incubated in HBS for >12 hours at room temperature (RT) to allow for more thorough diffusion of photosensitizer from the structures. The structures were then incubated with fluorescently-labeled NeutrAvidin at 20 μg mL^{-1} in HBS for >12 hours at RT. NeutrAvidin was labeled with either tetramethylrhodamine (A6373, Invitrogen) or Oregon Green (A6374, Invitrogen). Structures were then rinsed 10 times with 50 μL HBS and incubated for >12 hours at RT prior to imaging.

Structures fabricated from avidin protogels were incubated in HBS for 24 hours at RT to allow for more thorough diffusive removal of photosensitizer from the structures. The structures were then incubated with biotin-fluorescein conjugate (B1370, Invitrogen) at 20 μg mL^{-1} in HBS for 24 hours at RT. Structures were then rinsed 10 times with 50 μL HBS and incubated for 24 hours at RT prior to imaging.

2.2.3 Combined scan multiphoton lithography for high aspect ratio features

To fabricate large structures with high aspect ratio features, an altered dynamic mask procedure was used. The dynamic mask method previously described fabricated a single layer of a 3D object using a sequence of 2D mask images displayed on a DMD. The resulting 3D structure is limited in size by the field of view of the microscope

objective (on the order of 100 μm x 100 μm). The alternative "combined scan" method scans the fabrication laser in a linear pattern over a timed sequence of linear masks displayed on a DMD. When coordinated with stage scanning (Figure 2.1), this method can be used to fabricate millimeter-scale 3D structures.

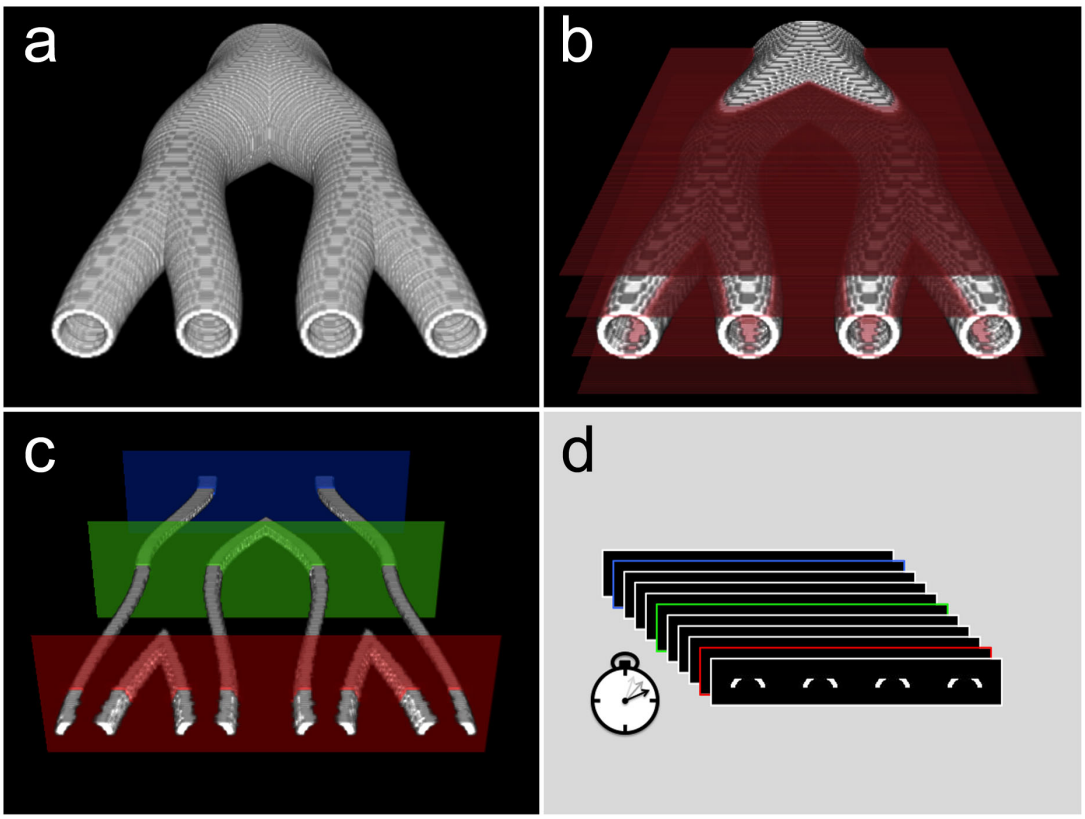

Figure 2.1 – Generating a mask for combined scan fabrication. (a) A 3D-rendered object, in this case a branching tube. (b) The object is virtually sliced into 2D sections. (c) Each slice is further cross-sectioned into a sequence of images. (d) The sequence of images is assembled into a single movie (.avi) file. Note: the colors used to illustrate selected orthogonal planes in "c" are shown as border colors on corresponding images in the sequence shown in "d".

The laser beam was linearly scanned over timed sequences of line masks displayed on the DMD, while the stage axis orthogonal to the line scan was activated to

move at a rate coordinated with the timing of the mask sequence (Figure 2.2). The resulting 2D structure formed one layer of the 3D structure, which could be fabricated from the top-down (Figure 2.2 b). Fabricating these structures from the top-down allows each new layer to be fabricated without the presence of previously fabricated layers in the beam path of the fabrication layer. This in turn allows the fabrication of structures with larger optical axis dimensions.

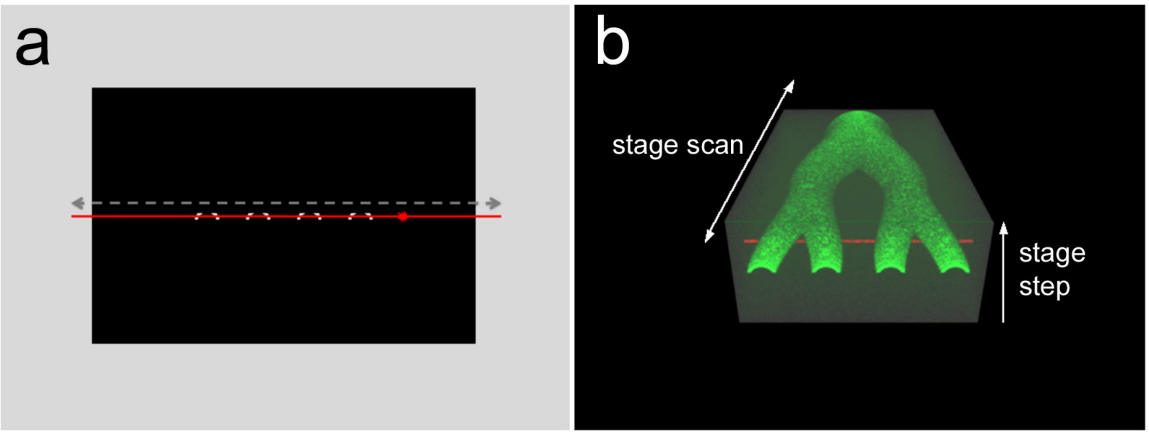

Figure 2.2 – Combined scan fabrication. (a) The DMD (represented by the black field) displays the timed sequence of masks, described in Fig 2.1. The red line represents the appearance of the linearly scanned laser beam when the beam focal point is rapidly scanned (~100 Hz) along the path described by the gray arrow. White-colored portions of each mask frame cause the laser beam to be reflected so that the displayed pattern is replicated as photocrosslinked hydrogel in the protogel. (b) By scanning the stage at a rate and direction coordinated with the sequenced display of the linear masks, millimeter-scale structures with high aspect ratio features can be fabricated layer-by-layer. When each layer is completed, the stage reverses direction along the stage scan axis and steps a predetermined distance along the optical axis, so that the next layer can be fabricated.

For the combined scan method, a 40x (0.95 NA) Olympus PlanApo microscope objective was used. Average laser power was 50 mW, measured at the back aperture of

the objective. The linear scan was established to generate an x-axis scan velocity of ~ 7 mm s^{-1}. The y-axis stage scan velocity was set to be 15 μm s^{-1}. These relative velocities were selected to ensure continuous fabrication in each layer. Both the raster scan and stage axis movements were controlled and coordinated by a computer using LabView.

As discussed previously, masks were generated by virtually slicing and cross-sectioning 3D rendered objects using ImageJ software. The masks consisted of a movie (.avi) file in which each frame represented a cross-section of a 2D layer of a 3D rendered object. The 3D rendered objects were typically generated using the ImageJ macro language. In the plane of the mask, 6 pixels distance on the DMD corresponded to 1 μm on the structure. The incremental optical axis steps between fabricated layers were 1 μm. Step size could have been smaller, but would have lengthened the time required for fabrication in proportion (0.5 μm steps would take twice as long, 0.33 μm steps would take 3 times longer, etc.).

2.2.4 Confocal image acquisition

Confocal image stacks were acquired using a Leica SP2 AOBS confocal microscope and either a 63X (1.4 NA) oil objective, a 63X (1.3 NA) water objective, or a 20X (0.7 NA) objective. Spacing between confocal planes was adjusted based on minimum feature size, and ranged from 0.1-1.0 μm. All images were processed using ImageJ software. Volume and isosurface 3D representations of confocal stacks and mask stacks were constructed using the "3D viewer" plugin (open source code, written by Benjamin Schmid).

2.2.5 Scanning electron microscopy

Scaning electron micrographs were acquired using an FEI Quanta 650 FEG Scanning electron microscope (SEM) in high vacuum (HV) mode. Protein hydrogel microstructures were prepared for imaging by soaking in HBS at room temperature for 24 hours, followed by 15 minute incubation in 5% (v/v) glutaraldehyde (18426, Ted Pella, Inc.) to further crosslink partially uncrosslinked protein. Structures were then washed sequentially in a 10 cm Petri dish with 20 mL each of deionized water, a 1:1 mixture of ethanol and deionized water, ethanol, a 1:1 mixture of ethanol and methanol, and methanol (each wash lasting 15 minutes). After the methanol was removed, protein microstructures were placed in a drying oven at 70° C for 15 minutes, then in a dessicator for 3 hours. The microstructures were sputter coated to a nominal thickness of 20 nm with Pt-Pd alloy using a Cressington 208 benchtop sputter coater.

2.2.6 Environmental scanning electron microscopy

Scanning electron micrographs were also acquired using the FEI Quanta 650 FEG SEM in environmental (ESEM) mode. Protein hydrogel microstructures were prepared by soaking in distilled, deionized water for 1 hour to reduce the concentration of buffer salts in the hydrogel. Microstructures were placed in the well of a Peltier-cooled stage with a small volume (< 100 μL) of deionized water. The stage was then placed in the SEM and brought to a temperature of 4 ºC. Pressure was adjusted in the SEM chamber to bring the relative humidity in the chamber to 80-90%. Images were acquired using the gaseous secondary electron detector (GSED), which was optimized for environmental (low-vacuum, high humidity) conditions.

2.2.7 Bacterial cell culture

Pseudomonas aeruginosa PA01 cells carrying the pMRP9-1 gfp plasmid were grown to saturation aerobically at 37 ºC overnight in tryptic soy broth (TSB) containing 300 mg mL^{-1} carbenicillin (for plasmid maintenance). An aliquot from the culture was then diluted and grown to midexponential phase. *P. aeruginosa* cells in TSB were introduced into 2 mL wells containing protein microstructures. Interactions between the cells and protein microstructures were observed and recorded over an 8-hour period at room temperature.

2.3 RESULTS AND DISCUSSION

2.3.1 Characterization of protogels

The development of the protogel material was spurred primarily by the desire to fabricate partially constrained and unconstrained freestanding hydrogel microstructures. A structure is classified as "partially constrained" if, as an independent structure, it is constrained by linkage with its neighbor and, ultimately, the substrate. A structure can be classified as "unconstrained" when it is free to translate and rotate without hindrance in three dimensions, and is not attached to the substrate or any other structure.

Maruo et al. have accomplished the fabrication of partially-constrained multiphoton-fabricated structures (e.g., gears on spindles) in a viscous acrylic precursor solution by special optimization of their scanning pattern [31]. Other investigators successfully used evaporative techniques to produce a solid precursor from which partially-constrained, linked chain structures could be fabricated [25, 32]. In this chapter, a more biologically relevant precursor material has been developed, using controlled drying of an aqueous solution of protein. Initial attempts resulted in a gel-like material in which unsupported structures could be fabricated, but the drying time required to produce

this material was not reproducible, being sensitive to small changes in protein concentration and ambient temperature/humidity. Furthermore, it was difficult to prevent over-drying this gel material during microstructure fabrication, as optically disruptive microdomains would form in the gel. It was found that DMSO added to the precursor solution reduced microdomain formation, both during the initial drying of the gel and during its subsequent use. Protogels made from precursor solutions containing 21% DMSO were used for hours with negligible microdomain formation.

Aqueous DMSO solutions exhibit nonlinear viscous properties [29] based on the interaction between the double-bonded oxygen in DMSO and the hydrogen atoms in water [33]. At specific molar ratios, the viscosity of the mixed solution can be nearly twice the viscosity of DMSO, and over four times that of water [34]. In addition to viscous factors, research has shown that some concentrations of DMSO, similar to the concentrations used here, enhance the hydrogen bonding of water [35], which could lower the vapor pressure and affect the quantity of water in the protogel. Finally, the presence of DMSO in aqueous solutions of the proteins BSA and lysozyme has been found to increase the hydrodynamic radius of the proteins through partial unfolding of the tertiary structure [36]. More study is required to determine the relative importance of each of these phenomena in the formation of protogels.

2.3.2 Unconstrained and partially constrained hydrogel structures

The multiphoton fabrication of structures within a protogel offers many advantages over other methods. Primarily, the high viscosity of the protogel ensures that there is no significant movement of the fabricated structure prior to rehydration of the protogel. This allows the fabrication of intricate unconstrained and partially constrained structures such as the morningstar seen in Figure 2.3. The links are free to move, and they

allow the star and chain to swing freely under oscillatory flow (Fig 2.3d). The star structure is used again without the chain in experiments below (Para. 2.3.4 and 2.3.5) in applications where an unconstrained structure is needed.

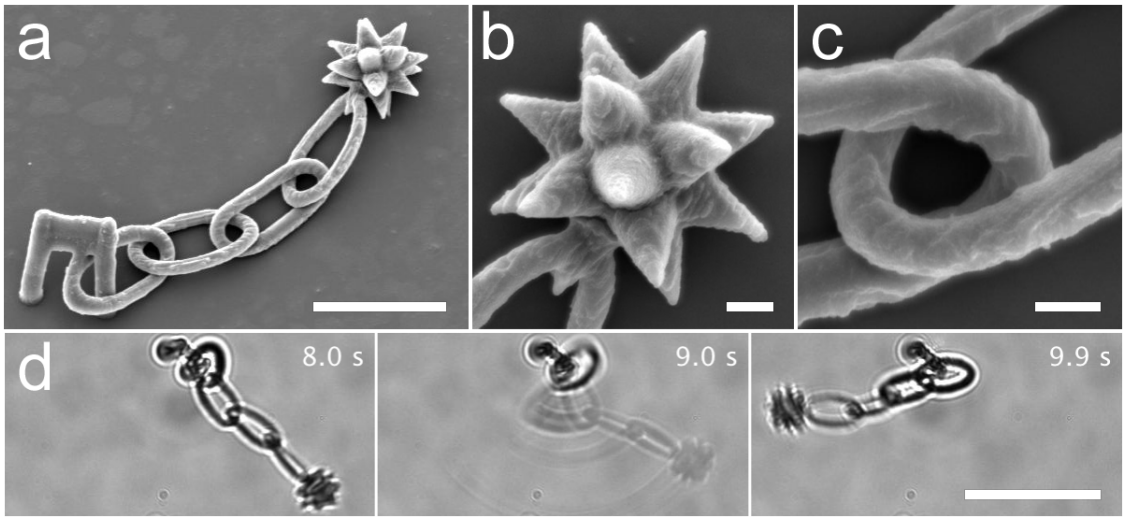

Figure 2.3 – A spiked ball and chain structure ("morningstar") fabricated from a BSA protogel. (a) Image of a morningstar structure. Note that it is not attached to substrate, but secured by a retaining structure seen on the lower left of the image. Scale bar is 20 μm. (b) Image showing detail of the star portion of the structure. Note that the radius of curvature of the points is < 1 μm. Scale bar is 3 μm. (c) Image showing detail of the chain portion of the morningstar. Note that the links are not fused. Scale bar is 2 μm. (d) Time-lapse bright-field microscope images of the morningstar structure under flow in HBS. Time stamps are in seconds. Scale bar is 30 μm.

Figure 2.3 shows a spiked ball and chain ("morningstar") fabricated using a protogel made from a solution of 29% BSA and 0.1% methylene blue (2.9 μmol g^{-1}). Following fabrication, the protogel was rehydrated with HBS to a liquid state, and then removed with a micropipette. Similar structures were fabricated using protogels made from precursor solutions containing 29% lysozyme instead of BSA (not shown). A solution of avidin was also successfully used to form a protogel, the results of which can

be found below (Paragraph 2.3.3). The total time required for fabrication of the structure in Fig. 2.3 was less than 3 minutes.

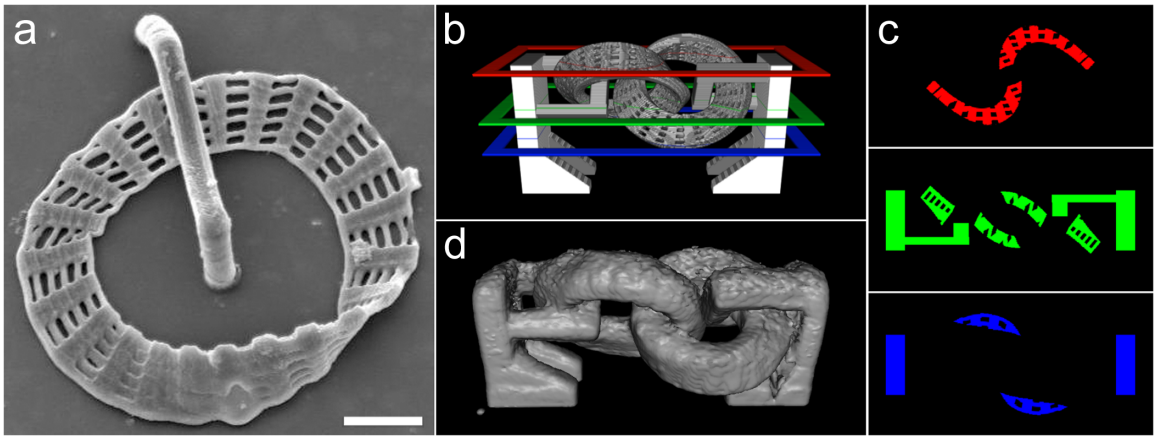

Figure 2.4 – Single and linked möbius strips fabricated from BSA protogels. (a) Scanning electron micrograph of a möbius strip formed of a single band of BSA that is not attached to the surface. The strip was anchored by fabricating a separate retaining structure (seen extending from the top of the image). Scale bar is 10 μm. (b) 3D reconstruction of the sequence of masks used to fabricate a möbius chain. Colored planes correspond to the locations of the sample masks shown in "c". The reconstruction illustrates that there is no connection between the möbius strips in the chain or their supports. (c) Selected masks from the stack of masks used to fabricate the möbius chain. Colors are only for cross-reference in "b". (d) 3D reconstruction of a stack of confocal images, showing the isosurface of a b-BSA structure functionalized with TMR-NAv conjugate. Surface detail is low due to relatively low signal/noise in the confocal imaging system.

The weight of precursor solution before drying and the weight of the resulting protogel after 30 minutes of drying were compared. Assuming that the weight lost was water evaporation, the final weight percentage of BSA in the protogel was 39.8 ±1.2% and the final weight percentage of DMSO in the protogel was 28.1 ±0.9% (n = 5 protogels). Aqueous precursor solutions of BSA (without DMSO) are commonly prepared at 48% protein; however, unconstrained structures cannot be fabricated in these solutions. Therefore, it seems possible that the DMSO in the solvent is interacting with

the other molecules to stabilize the solution and prevent excessive water evaporation and/or crystallization of the protein.

Another partially constrained structure is shown in Figure 2.4, which also illustrates the process used to fabricate a pair of linked möbius strips from a BSA protogel.

2.3.3 Effect of protogel process on protein functionality

One important reason for using proteins in these experiments is that they have inherent biological functions that may be useful when using MPL to modify the cellular microenvironment. In such applications, the fabrication process must not dramatically alter the functionality of the protein used. The protein avidin was selected as a model for testing the effect of the protogel process on the functionality of proteins. Because the biotin-binding property of avidin is dependent on its tertiary and quaternary structure, this protein should provide an indication of the general effect of the protogel fabrication process on proteins as a whole.

Figure 2.5 shows the results of an experiment that used a biotin-fluorescein conjugate to test the biotin-binding capability of a structure fabricated from an avidin protogel. The biotin binding of the avidin structures was compared to the biotin binding capabilities of structures fabricated from a BSA protogel using the same mask sequence. The mask sequence was designed so that each structure included two 10 μm cubes that did not contact the glass surface. Because the cubes in each of the different structures were the same dimensions, the wide-field fluorescence intensity of each cube could be directly compared quantitatively using mean fluorescence as an analogue to biotin binding. For each material, avidin and BSA, fluorescence images were required for two structures, and the mean fluorescence signal of the two cubes from each structure was

measured for a 70 pixel square region (approximately 60 μm^2). Results (Fig. 2.5b) show that, compared to BSA under the same conditions, avidin structures are much more efficient at binding biotin, which suggests that proteins retain their tertiary structure in the hydrogel.

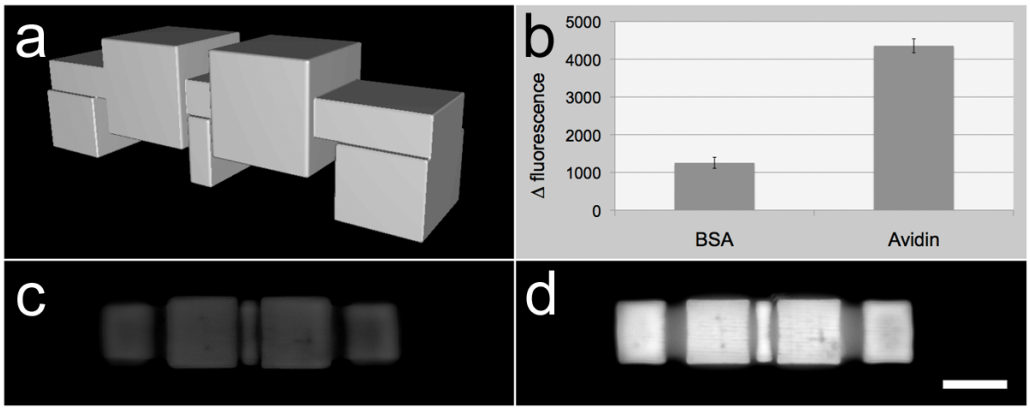

Figure 2.5 – Biotin-binding structures made from avidin protogel. (a) 3D reconstruction of the mask sequence used to fabricate test blocks for the biotin binding experiment. (b) Bar graph showing the change in fluorescence intensity of BSA and avidin blocks before and after exposure to biotin-fluorescein. Error bars show standard deviation of the difference in mean fluorescence intensity for each set of cubes (n=4). The source images are 14-bit images. (c) Wide-field fluorescence control image of a representative avidin structure in HBS, prior to incubation with biotin-fluorescein conjugate. (d) Wide-field fluorescence image of the same representative structure shown in c, after incubation in biotin-fluorescein conjugate and rinsing in HBS. Fluorescence images were acquired using a standard "green" filter set (Chroma, 42011). Scale bar is 10 μm.

2.3.4 Nested structures

Protogel can be prepared on a surface supporting pre-existing microstructures, allowing the fabrication of nested structures composed of different proteins. This result of this process is shown in Figure 2.6. In the structure shown in Fig. 2.6b, the outer circular structure is the wall of a dome-shaped cage with rectangular vent holes. The inner circular structure is a sphere with circular vent holes. The cage and sphere were both

fabricated using a single lysozyme protogel, after which the structure was rehydrated, rinsed and submerged in a biotinylated BSA solution. After allowing the BSA solution to soak into the cage structures thoroughly, the solution was dried to protogel, and the 18-point star, seen in the center of Fig. 2.6b, was fabricated in the center of the sphere. A cut-away reconstruction of the masks used to fabricate the nested structure (Fig. 2.6a) shows the relative geometries of the structure.

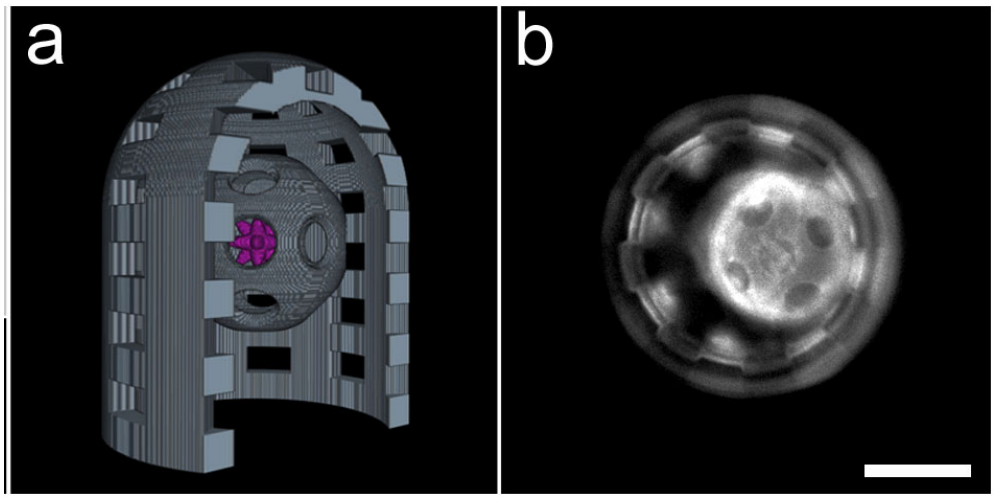

Figure 2.6 – Nested structures. (a) Cut-away reconstruction of masks used to fabricate a nested structure of lysozyme and BSA. The mask used during the lysozyme step is shown in gray, the mask used during the BSA step is shown in magenta. (b) Wide-field fluorescence image of a nested structure, using a green filter set (Chroma, 42011). Scale bar is 20 μm.

2.3.5 Interactive traps for bacteria

To illustrate the general biocompatibility of microstructures fabricated from protogels, and to demonstrate the capability of the microstructures to interact dynamically on a cellular scale, bacterial traps (Figure 2.7) were fabricated from a BSA protogel and subsequently incubated with *P. aeruginosa*.

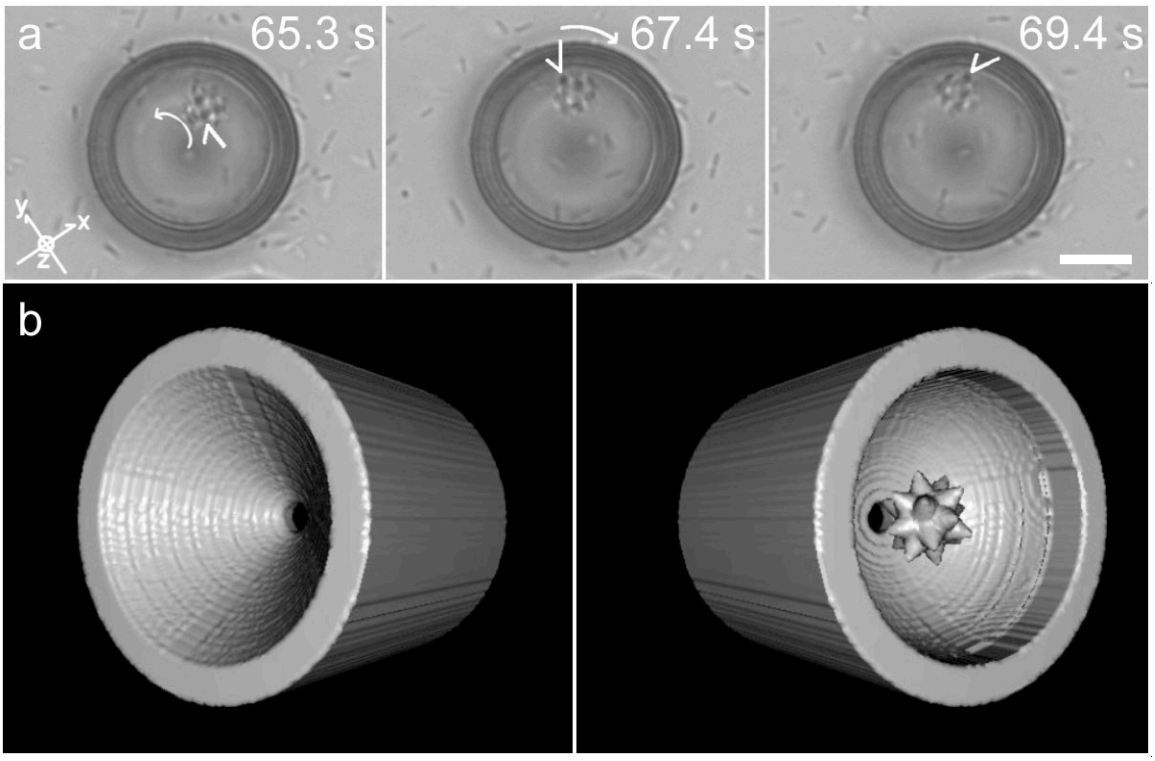

Figure 2.7 – Bacterial interaction with an unconstrained microstructure. (a) Series of three images from a time-lapse series, showing the tumbling movement of an 18-point BSA star as a result of collisions with *P. aeruginosa* and solution movement. In the left frame (65.3 s), a caret (∠) is used to indicate a single point of the star for reference. By the middle frame (67.4 s), the star has rolled around the x-axis, and the reference star point is on the opposing side of the image (the caret reflects this movement by changing its "handedness"). Two seconds later in the right frame (69.4 s), the star has rotated around the z-axis, so that the reference point is in a new position. Scale bar is 10 μm. (b) Two views of a 3D reconstruction of the masks used to fabricate the bacterial traps seen in "a". The left frame represents the view down towards the glass substrate, and shows the funnel that leads bacteria to the 3 μm entrance pore. The right frame represents the view looking up through the glass substrate, and shows the 18-point star mask in the middle of a hemispherical chamber.

The traps combined a funnel top leading down to a narrow pore entrance with a hemispherical chamber fabricated directly on the glass substrate. An unconstrained 18-

point star was fabricated in the center of the hemispherical chamber. The star was designed with a spherical interior void to give it lower mass and more neutral buoyancy. Because the bacteria could easily swim into the trap, but were less likely to swim out, they accumulated rapidly in the chamber, and the star was buffeted randomly both by direct collision with bacteria, and by flagellum-generated convective flow. Figure 2.7a shows that this buffeting generates translation and rotation in 3 dimensions.

2.3.6 Combined scan structures

The combined scan technique allows the fabrication of millimeter-length structures by extending the range of one of the fabrication axes. The result is very high aspect ratio structures that have micron-scale features. This fabrication technique was used to create the stacked microtube structure shown in Figure 2.8. The mask animation used to fabricate the structure was designed as two stacks of 9 tubes, each with overlapping walls. Each tube was designed to have a 10 μm inner diameter and to be 1.0 mm long. The structure was temporarily attached to the glass substrate using narrow strips of protein hydrogel. Once rehydrated, gentle, pulsatile rinsing was sufficient to break the strips, which allowed the transfer of the structure to the ESEM stage with forceps. Some damage was done during movement (Fig. 2.8b), but generally the structure remained intact. Analysis of the ESEM micrographs shows that the structure has elongated along the long axis, and contracted some on the short axis, causing the tubes to become smaller and somewhat more oval in cross section (Figs. 2.8c-d). While the ESEM micrographs (Figs. 2.8b-d) were acquired at 90% humidity, the humidity was as low as 5% during evacuation of the chamber, which may have caused some inelastic deformation of the structure.

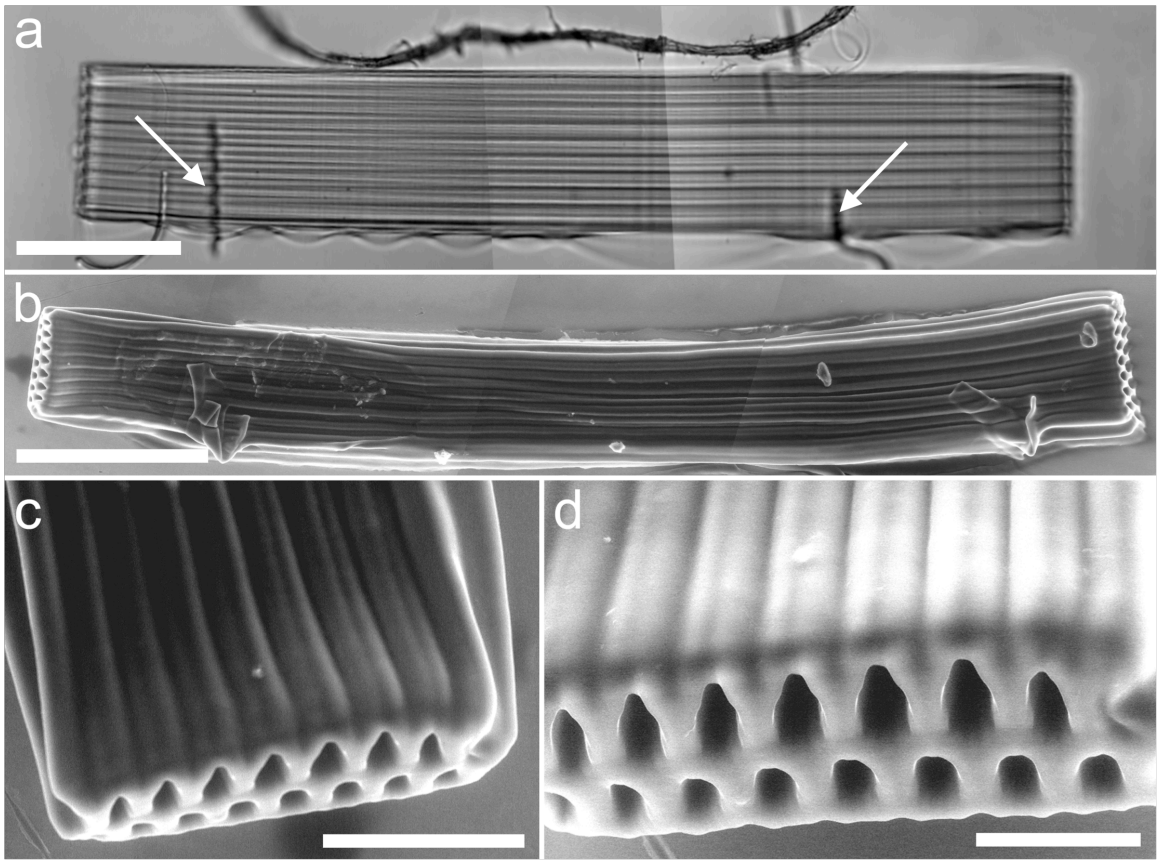

Figure 2.8 – High aspect ratio microtube structure fabricated using the combined scan method. (a) A composite image of microtubes in HBS shows the structure as a fully rehydrated hydrogel. The tube at the lower portion of the image has partially separated from the structure. The dark vertical lines shown in the image (identified with arrows) are the strips used to temporarily attach the tubes to the substrate during rehydration. Scale bar is 200 μm. (b) A composite ESEM micrograph shows the same structure at 90% humidity. Some microtubes have been lost transferring the structure to the ESEM sample stage. Scale bar is 200 μm. (c) An ESEM micrograph of the end of the structure shows the texture and alignment of the microtubes. Scale bar is 50 μm. (d) A higher magnification ESEM micrograph taken at a larger tilt-angle shows more detail of the cross section of the tubes. Scale bar is 25 μm.

Structures such as this microtube array, if scaled appropriately, could conceivably be used as a cell scaffold material in a peripheral nerve guide. However, because the cross section of the tube structure is uniform, the structure does not demonstrate the full

potential of the combined scan method. More complicated structures, such as the branched tube shown below (Figure 2.9), further demonstrates the versatility of this fabrication approach.

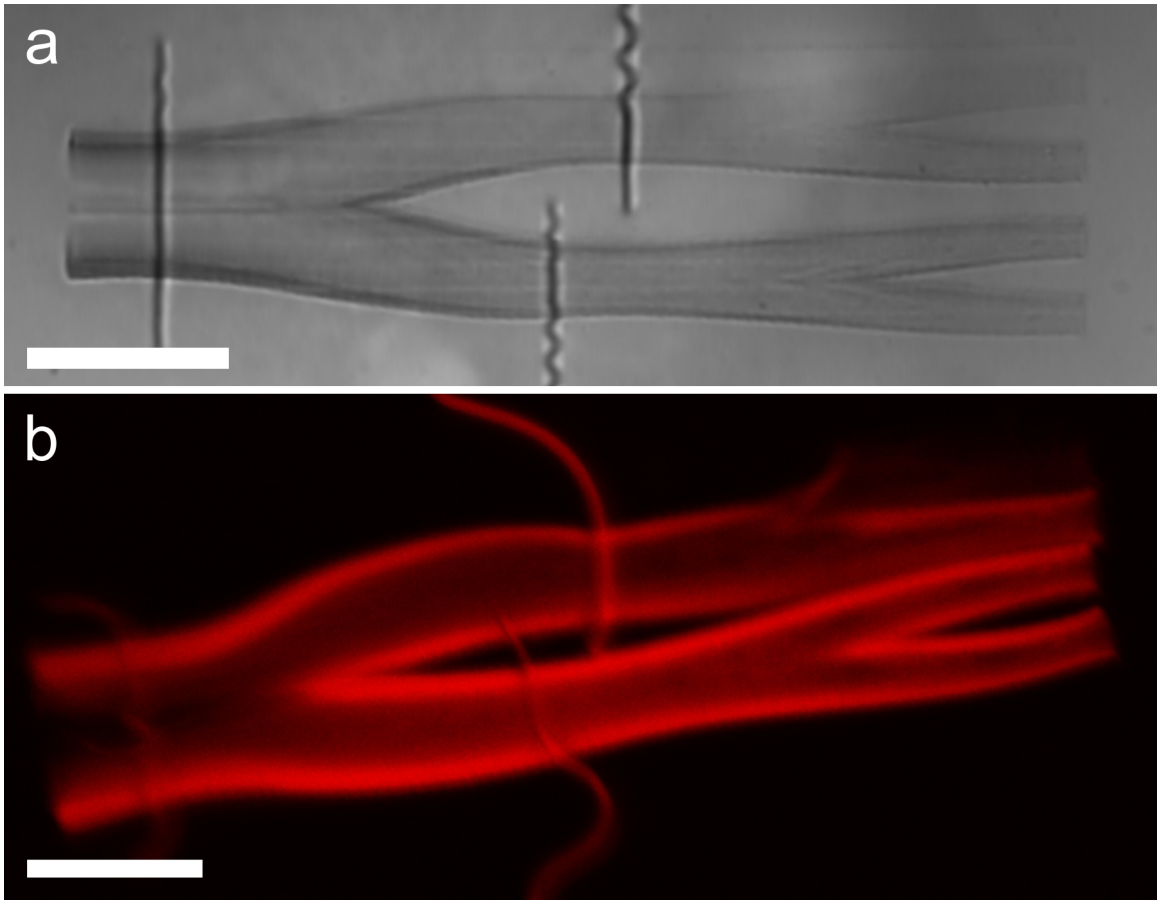

Figure 2.9 – Branched microtube fabricated using the combined scan method. (a) Image of a branched microtube in protogel prior to rehydration shows a structure similar to the example used in Figures 2.1 & 2.2. Vertical lines were fabricated after the branched microtube to retain the structure during rinsing. Scale bar is 100 μm. (b) Image generated from averaged confocal stacks shows a branched microtube after rehydration, confirming the unobstructed continuity of the interior space. Scale bar is 100 μm.

The structure was inspired by vasculature, but does not represent any particular vascular network, nor was it designed with a specific application in mind. However, as a

proof of concept, it demonstrates the possibility to use MPL for vascular engineering applications, or other biomedical applications that may require a dendritic structure. The mask sequence used was generated mathematically, with the diameter of each trunk being twice that of the two subsidiary branches. The structure as it appeared after fabrication (Fig. 2.9a) shows two full iterations of branching, from a single tube with a diameter of 40 μm, to four tubes each with a diameter of 10 μm. After rehydration, confocal imaging confirmed the unobstructed continuity of the branched structure's interior space (Fig 2.9b). Of note is the absence of the uppermost branch of the structure, which was lost during rehydration. This is most likely due to a slight misalignment in the laser optics at the time of fabrication, which is relatively easy to correct once identified.

2.4 CONCLUSIONS

The intricate unconstrained and partially-constrained protein hydrogel microstructures fabricated here represent a class of materials previously unexploited by researchers. The ability to fabricate these structures from proteins rather than resins represents a significant step in how they can interact with biological systems – protein structures are inherently biological and can be more easily used to recreate the chemical and mechanical microenvironment of specific cells and tissue. As a result, they are uniquely suitable for a range of biomedical applications. For example, unconstrained hydrogel microparticles of specific geometry could open new possibilities in the area of drug delivery, where micro- and nanoscale hydrogels are currently limited to spheroids or simple geometric shapes like disks or pyramids [37-39]. The use of more unconventional geometries could be useful both for engineering hydrogel interaction with cells and for designing new drug release profiles. Unconstrained hydrogels could also lead to more fundamental research into cell behavior like bacterial swarming, or allow researchers to

harness the forces generated by bacterial propulsion [3, 40]. Another potential application for these structures is suggested by the recent work of Khripin et al., who successfully used MPL to fabricate protein templates that were then turned into silica replicas via a relatively straightforward chemical process [41].

When protogels are used with the combined scan fabrication technique, tangible improvements to implant devices like peripheral nerve graft are easily visualized. A nerve guide made using a scaffold material similar to the structure seen in Figure 2.8 would represent a dramatic improvement over current technologies, not only in terms of micron-scale specificity, but also in terms of tuning the mechanical and chemical properties of the material, to be discussed in the next chapters.

2.5 REFERENCES

1. Bargiel S., Rabenorosoa K., Clévy C., Gorecki C., Lutz P., Towards micro-assembly of hybrid MOEMS components on a reconfigurable silicon free-space micro-optical bench. *Journal of Micromechanics and Microengineering* **20**, 045012 (2010).
2. Kershner R.J., Bozano L.D., Micheel C.M., Hung A.M., Fornof A.R., Cha J.N., Rettner C.T., Bersani M., Frommer J., Rothemund P.W.K., Wallraff G.M., Placement and orientation of individual DNA shapes on lithographically patterned surfaces. *Nature Nanotechnology* **4**, 557-561 (2009).
3. Sokolov A., Apodaca M.M., Grzybowski B.A., Aranson I.S., Swimming bacteria power microscopic gears. *Proceedings of the National Academy of Sciences of the United States of America* **107**, 969-974 (2010).
4. Caldorera-Moore M., Kang M.K., Moore Z., Singh V., Sreenivasan S.V., Shi L., Huang R., Roy K., Swelling behavior of nanoscale, shape- and size-specific, hydrogel particles fabricated using imprint lithography. *Soft Matter* **7**, 2879-2887 (2011).
5. Suri S., Han L.-H., Zhang W., Singh A., Chen S., Schmidt C.E., Solid freeform fabrication of designer scaffolds of hyaluronic acid for nerve tissue engineering. *Biomedical Microdevices*, **13**, 983-993 (2011).
6. Connell J.L., Wessel A.K., Parsek M.R., Ellington A.D., Whiteley M., Shear J.B., Probing prokaryotic social behaviors with bacterial "lobster traps". *mBio* **1**, (2010).

7. Wylie R.G., Ahsan S., Aizawa Y., Maxwell K.L., Morshead C.M., Shoichet M.S., Spatially controlled simultaneous patterning of multiple growth factors in three-dimensional hydrogels. *Nature Materials* **10**, 799-806 (2011).
8. Seidlits S.K., Khaing Z.Z., Petersen R.R., Nickels J.D., Vanscoy J.E., Shear J.B., Schmidt C.E., The effects of hyaluronic acid hydrogels with tunable mechanical properties on neural progenitor cell differentiation. *Biomaterials* **31**, 3930-3940 (2010).
9. Cuchiara M.P., Allen A.C.B., Chen T.M., Miller J.S., West J.L., Multilayer microfluidic PEGDA hydrogels. *Biomaterials* **31**, 5491-5497 (2010).
10. Leach J.B., Bivens K.A., Patrick C.W., Schmidt C.E., Photocrosslinked hyaluronic acid hydrogels: Natural, biodegradable tissue engineering scaffolds. *Biotechnology and Bioengineering* **82**, 578-589 (2003).
11. Banerjee A., Arha M., Choudhary S., Ashton R.S., Bhatia S.R., Schaffer D.V., Kane R.S., The influence of hydrogel modulus on the proliferation and differentiation of encapsulated neural stem cells. *Biomaterials* **30**, 4695-4699 (2009).
12. Hyon S.H., Cha W.I., Ikada Y., Preparation of transparent poly(vinyl alcohol) hydrogel. *Polymer Bulletin* **22**, 119-122 (1989).
13. Revzin A., Russell R.J., Yadavalli V.K., Koh W.G., Deister C., Hile D.D., Mellott M.B., Pishko M.V., Fabrication of Poly(ethylene glycol) Hydrogel Microstructures Using Photolithography. *Langmuir* **17**, 5440-5447 (2001).
14. Zawko S.A., Schmidt C.E., Crystal templating dendritic pore networks and fibrillar microstructure into hydrogels. *Acta Biomaterialia* **6**, 2415-2421 (2010).
15. Du Y., Lo E., Ali S., Khademhosseini A., Directed assembly of cell-laden microgels for fabrication of 3D tissue constructs. *Proceedings of the National Academy of Sciences of the United States of America* **105**, 9522-9527 (2008).
16. Lee S.-H., Moon J.J., West J.L., Three-dimensional micropatterning of bioactive hydrogels via two-photon laser scanning photolithography for guided 3D cell migration. *Biomaterials* **29**, 2962-2968 (2008).
17. Ji Y., Ghosh K., Shu X.Z., Li B., Sokolov J.C., Prestwich G.D., Clark R.A.F., Rafailovich M.H., Electrospun three-dimensional hyaluronic acid nanofibrous scaffolds. *Biomaterials* **27**, 3782-3792 (2006).
18. Yamada A., Niikura F., Ikuta K., A three-dimensional microfabrication system for biodegradable polymers with high resolution and biocompatibility. *Journal of Micromechanics and Microengineering* **18**, (2008).
19. Nielson R., Kaehr B., Shear J.B., Microreplication and Design of Biological Architectures Using Dynamic-Mask Multiphoton Lithography. *Small* **5**, 120-125 (2009).
20. Kaehr B., Allen R., Javier D.J., Currie J., Shear J.B., Guiding neuronal development with in situ microfabrication. *Proceedings of the National Academy of Sciences* **101**, 16104-16108 (2004).

21. Seidlits S.K., Schmidt C.E., Shear J.B., High-Resolution Patterning of Hydrogels in Three Dimensions using Direct-Write Photofabrication for Cell Guidance. *Advanced Functional Materials* **19**, 3543-3551 (2009).
22. Maruo S., Nakamura O., Kawata S., Three-dimensional microfabrication with two-photon-absorbed photopolymerization. *Optics letters* **22**, 132-134 (1997).
23. Maruo S., Ikuta K., Three-dimensional microfabrication by use of single-photon-absorbed polymerization. *Applied Physics Letters* **76**, 2656 (2000).
24. Lin C.-L., Vitrant G., Bouriau M., Casalegno R., Baldeck P.L., Optically driven Archimedes micro-screws for micropump application. *Optics Express* **19**, 8267-8276 (2011).
25. Kuebler S.M., Rumi M., Watanabe T., Braun K., Cumpston B.H., Heikal A.A., Erskine L.L., Thayumanavan S., Barlow S., Marder S.R., Perry J.W., Optimizing Two-Photon Initiators and Exposure Conditions for Three-Dimensional Lithographic Microfabrication. *Journal of Photopolymer Science and Technology* **14**, 657-668 (2001).
26. Park K., Effect of shape and size of polymer particles on cellular internalization. *Journal of controlled release : official journal of the Controlled Release Society* **147**, 313 (Nov 1, 2010).
27. Sharma G., Valenta D.T., Altman Y., Harvey S., Xie H., Mitragotri S., Smith J.W., Polymer particle shape independently influences binding and internalization by macrophages. *Journal of Controlled Release* **147**, 408-412 (2010).
28. Ritschdorff E.T., Nielson R., Shear J.B., Multi-focal multiphoton lithography. *Lab on a Chip* **12**, 867-871 (2012).
29. LeBel R.G., Goring D.A.I., Density, Viscosity, Refractive Index, and Hygroscopicity of Mixtures of Water and Dimethyl Sulfoxide. *Journal of Chemical & Engineering Data* **7**, 100-101 (1962).
30. Ritschdorff E.T., Nielson R., Shear J.B., Multi-focal multiphoton lithography. *Lab on a Chip* **12**, 867-871 (2012).
31. Maruo S., Ikuta K. Fabrication of freely movable microstructures by using two-photon three-dimensional microfabrication. *Proceedings of SPIE* **3937,** 106-112 (2000).
32. Wu D., Chen Q.D., Niu L.G., Wang J.N., Wang J., Wang R., Xia H., Sun H.B., Femtosecond laser rapid prototyping of nanoshells and suspending components towards microfluidic devices. *Lab on a Chip* **9**, 2391 (2009).
33. Soper A.K., Luzar A., Orientation of Water Molecules around Small Polar and Nonpolar Groups in Solution - A Neutron Diffraction and Computer Simulation Study. *The Journal of Physical Chemistry* **100**, 1357-1367 (1996).
34. Cowie J.M.G., Toporowski P.M., Association in the binary liquid system dymethyl sulphoxide-water. *Canadian Journal of Chemistry* **39**, 2240-2243 (1961).
35. Lai J.T.W., Lau F.W., Robb D., Westh P., Nielsen G., Trandum C., Hvidt A., Koga Y., Excess partial molar enthalpies, entropies, Gibbs energies, and volumes in aqueous dimethylsulfoxide. *Journal of Solution Chemistry* **24**, 89-102 (1995).

36. Huang A., Liu C., Ma L., Tong Z., Lin R., Effects of clustering structure on volumetric properties of amino acids in DMSO-water mixtures. *The Journal of Chemical Thermodynamics*, 1-31 (2012).
37. Dendukuri D., Tsoi K., Hatton T.A., Doyle P.S., Controlled Synthesis of Nonspherical Microparticles Using Microfluidics. *Langmuir* **21**, 2113-2116 (2005).
38. Gratton S.E.A., Ropp P.A., Pohlhaus P.D., Luft J.C., Madden V.J., Napier M.E., DeSimone J.M., The effect of particle design on cellular internalization pathways. *Proceedings of the National Academy of Sciences* **105**, 11613-11618 (2008).
39. Venkataraman S., Hedrick J.L., Ong Z.Y., Yang C., Ee P.L.R., Hammond P.T., Yang Y.Y., The effects of polymeric nanostructure shape on drug delivery. *Advanced Drug Delivery Reviews* **63**, 1228-1246 (2011).
40. Di Leonardo R., Angelani L., Dell'Arciprete D., Ruocco G., Iebba V., Schippa S., Conte M.P., Mecarini F., De Angelis F., Di Fabrizio E., Bacterial ratchet motors. *Proceedings of the National Academy of Sciences* **107**, 9541-9545 (2010).
41. Khripin C.Y., Pristinski D., Dunphy D.R., Brinker C.J., Kaehr B., Protein-Directed Assembly of Arbitrary Three-Dimensional Nanoporous Silica Architectures. *ACS Nano* **5**, 1401-1409 (2011).

Chapter 3: Multiphoton lithography of hydrogels with tunable moduli

3.1 Introduction

Cells can only develop into functional tissue and organs when they receive the correct signals and guidance from extracellular sources. Seidlits et al. have shown that the differentiation of neural progenitor cells into either neural or glial cells can be controlled by tuning the modulus of the hydrogel substrate [1]. Hydrogel moduli used in that study ranged from ~1-8 kPa, which is on the same order as neural tissue. Similar studies have shown comparable results in differentiating other types of cells using different ranges of substrate modulus, including differentiation of mesenchymal stem cells into myoblasts (~10 kPa) and osteoblasts (~50 kPa) on polyacrylamide [2], and stimulation of osteogenesis by osteoblasts (>225 kPa) on polyethelyne glycol dimethacrylate [3]. Likewise, migrating cells such as fibroblasts [4], and extending axons [5] have shown a sensitivity to substrate modulus. Young's modulus is only one of many mechanical properties of extracellular matrix (ECM). For most hydrogels, however, there are predictable correlations between Young's modulus and other relevant physical properties like pore size and density that make it a useful metric for comparison. Therefore, ECM elasticity is an important signal, even if the specific details of how cells interpret it remain unclear [6].

Multiphoton lithography (MPL) allows sub-micron control of the crosslinking chemistry required for hydrogel formation, and thus offers unique opportunities to tune the mechanical properties of the resulting hydrogel on the scale of individual cells. Nielson et al. exploited this lithographic method in combination with an optical array incorporating a digital multimirror device (DMD), which operates as a dynamic, virtual mask. The result is a method that allows layer-by-layer 3D fabrication of intricate,

micron scale hydrogels [7]. Khripin et al. have recently used this method to fabricate micron-scale cantilever structures that were used to determine the Young's modulus of MPL-fabricated protein hydrogels. The authors found that changing the laser fluence used for fabrication allowed them to tune the modulus of the hydrogel over two orders of magnitude (~30-3000 kPa) [8]. However, this range does not cover the 1-8 kPa range of neural tissue, nor does the study examine the effect on modulus of other fabrication parameters, such as the relative concentrations of constituent molecules in the precursor solution.

This chapter reports the results of modulus measurements on hydrogels fabricated using MPL. Although past studies have measured the moduli of conventional hydrogels fabricated from a wide range of biomaterials [1, 9, 10], a separate examination of the properties of multiphoton fabricated hydrogels is warranted due to the nonlinear dynamics inherent to MPE-based photochemistry, and the number of other variables that ultimately affect crosslinking. The dynamic masking method was used to fabricate hydrogels from hybrid solutions of commonly used natural and synthetic biomaterials: bovine serum albumin (BSA), glycidyl methacrylate hyaluronic acid (GMHA), and polyethylene glycol diacrylate (PEGDA). The Young's moduli of these hydrogels were then estimated from force measurements acquired with an atomic force microscope (AFM).

BSA, GMHA and PEGDA were used for this study, due to a combination of their availability, utility with respect to MPL, and their minimal impact on cells. As such, they provide a good starting point for examining the Young's modulus of hydrogels fabricated using MPL, and serve as general representatives of a larger range of potentially useful biomaterials.

Serum albumin is a blood plasma protein that is primarily used to transport low-solubility molecules in the circulatory system. As such, it has low toxicity and immunogenicity, and is often used in studies where biocompatibility is an issue [11, 12]. It has also been used for multiphoton lithography to fabricate cell scaffold-like hydrogel structures [13, 14].

Hyaluronic acid is a highly-conserved glycosaminoglycan found in the extracellular matrix (ECM) of mammals, it is nonimmunogenic and not cell-adhesive [15]. When functionalized with glycidyl methacrylate, it can be photocrosslinked to form a hydrogel [16]. It has also been shown to be useful as a cell scaffold material [17, 18].

Polyethylene glycol (PEG) is a synthetic biopolymer that represents something of a biological "blank slate" with regards to its effect on living systems. It is non-toxic, non-immunogenic, non cell-adhesive, and has been approved for medical use [19]. When functionalized with terminal acrylate groups, it can be photocrosslinked to form hydrogels. When further functionalized with bioactive molecules, or mixed with other polymers, PEGDA has been used as a cell scaffold material [18, 20].

3.2 INDENTATION MODELING

Hertz-based indentation modeling provides a useful method for measuring the Young's modulus of soft surfaces [21, 22], allowing accurate measurements with micron-scale resolution and relatively little *a priori* knowledge. In particular, this model does not require detailed knowledge of the geometry of the surface (other than its thickness), only knowledge of the probe geometry (usually a rigid sphere).

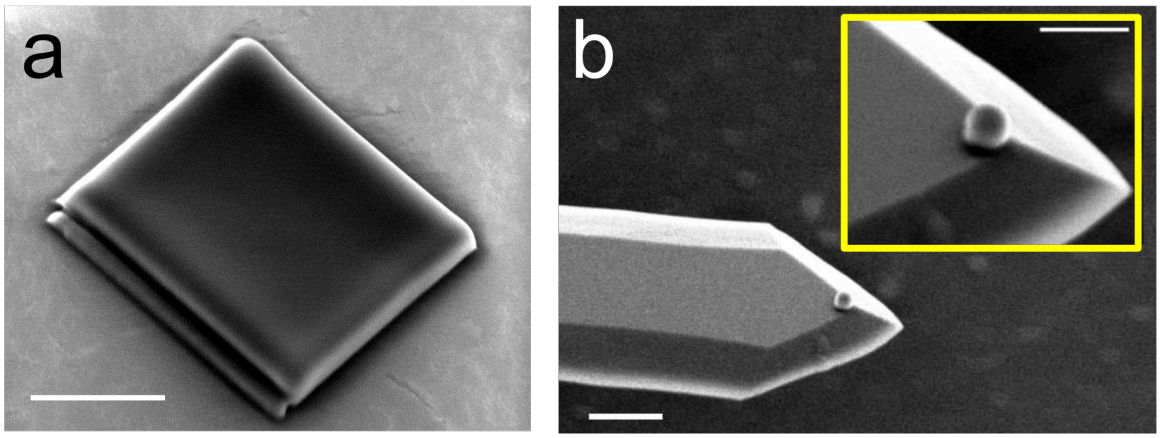

Figure 3.1 – Indentation modeling geometries. (a) Scanning electron micrograph of a typical hydrogel block used for modulus studies. Note the relatively smooth, even surface of the hydrogel. Scale bar is 20 μm. (b) Micrograph of a bead-tipped atomic force microscope (AFM) cantilever. Scale bar is 10 μm. Inset shows detail of the bead tip. Inset scale bar is 5 μm.

The Hertz model was originally developed to describe the normal contact between two spheres [23]. Later researchers adapted it to describe the contact between a spherical object of infinite modulus and a planar surface of unknown modulus [24]. As such, one can describe the force (F) of a normal interaction between the surface and a sphere of radius R as a function of the indentation (δ), where the Young's modulus (E) is a constant, and where ν is the Poisson ratio* of the surface.

$$F = E \cdot \left(\frac{4}{3(1-\nu^2)} \right) \sqrt{R \cdot \delta^3} \qquad (3.1)$$

If we assume that the hydrogel is a linear-elastic material, then $\nu = 0.5$, and Eq. 1 simplifies to $F = (16/9)*E(R\delta^3)^{1/2}$. In the context of measuring micron-scale hydrogels

* Poisson's ratio (ν) is the ratio of expansion/contraction (due to strain) in one dimension to the resulting expansion/contraction in an orthogonal dimension. In the context of bead indentation of a hydrogel, it is the expansion of the material in a radial direction away from the bead along the surface of the hydrogel, over the contraction of the thickness of the hydrogel in the axial direction due to the indentation. For an ideal anisotropic hydrogel, this value can be assumed to be 0.5 (sign convention makes it positive). Studies of similar hydrogels return values between 0.42 and 0.45 [Johnson, et al., 2004]

with an atomic force microscope (AFM), this means that as long as care is taken to fabricate relatively flat and even hydrogel surfaces (Figure 3.1a), the only geometry needed is an accurate measurement of the tip of the AFM probe, which can be easily determined using a scanning electron microscope (Figure 3.1b). This approach therefore allows one to examine a single layer of fabricated material, which obviates the need to make thicker, multilayer structures and introduce additional variables (layer thickness, layer spacing, etc) into the system.

One of the consequences of adapting the Hertz model to describe the interaction between a sphere and a surface is that the surface in question (in this case, a hydrogel) is assumed to be infinitely thick with respect to the radius of the sphere. In practical terms, Dimitriadis et al. suggest that the thickness (h) must be greater than 12.8 * R in order for this assumption to be satisfied*. If h does not satisfy this limitation, the calculated value for E will represent some integration of the actual value with the modulus of the underlying surface. For the system measured in this study, where the substrate (glass) has a much higher modulus, and much greater thickness than the hydrogel, the modulus and thickness of the glass can both be assumed as infinite. Further analysis of this problem has led to a numerical solution, such that if the thickness h of the hydrogel is known, then

$$F_m = (16/9)E\sqrt{R\cdot\delta^3}\left[1 + 1.133\chi + 1.283\chi^2 + 0.769\chi^3 + 0.0975\chi^4\right], \qquad (3.2)$$

where F_m is the measured force and χ is a dimensionless variable equal to $(R\delta)^{1/2} * h^{-1}$ [26]. This means that for the single layer hydrogels examined in this study, as long as the thickness is known, a correction can be made for the measured value of E to return a value closer to the actual value.

* Back-calculation using Equations 3.1 and 3.2 shows that for h > 12.8*R, the difference between the value of E found using Equation 3.1 and the value found using Equation 3.2 is less than 10%. Dimitriadis suggests this as the threshold for use of thickness correction as a result.

Another important limitation of the Hertz model is that it assumes infinitesimal strain, which effectively translates to infinitesimal indentation. Since acquiring physical measurements with the AFM requires applying enough force to generate a measureable indentation, this limitation cannot be satisfied. Nevertheless, common practice suggests that at maximum axial strains $(\varepsilon_{zz})^*$ less than 0.2, the underlying linear elastic assumptions of the Hertz model are maintained [26]. Therefore, all data presented here disregard portions of the curve that represent $\varepsilon_{zz} > 0.2$, in order to maintain the assumption of elastic linearity.

3.3 MATERIALS AND METHODS

3.3.1 Hydrogel precursor solutions

All solutions used a simplified HEPES buffered saline (HBS) solution, containing 0.02 M HEPES (Sigma, H3375) and 0.1 M NaCl, as the solvent. HBS was adjusted using pH 7.3 prior to use. PEGDA with molecular weight 700 Da (Aldrich, 455008), BSA (Equitech Bio, BAH64), and rose bengal (RB, Aldrich, 330000) were used as received. GMHA was synthesized using 16 kDa hyaluronic acid (Lifecore Biomed., HA10K), triethylamine (Sigma, T0886), and glycidyl methacrylate (Fluka, 64161), as described in Seidlits et al. [1], although dialysis against deionized water was used (instead of acetone precipitation) to purify the synthesized GMHA prior to lyophilization. A nuclear magnetic resonance spectrum of the GMHA indicated 11% methacrylation of the polymer.

* ε_{zz} is used to denote the maximum axial strain. Because axial strain ε_z is a function of the area of the sphere in contact with the hydrogel surface, ε_{zz} is used to denote the axial strain at the point where the z-axis intersects the contact surface, which is the point at which the system experiences the maximum force and largest strain. For the purposes of calculating the Young's modulus, this is the only strain of importance.

3.3.2 MPL fabrication of hydrogels

The dynamic mask-based multiphoton lithography (MPL) technique used in this chapter is described in detail in Ritschdorff et al. [27]. The system described in that study produced overlapping laser scan fields – in this chapter only one scan field was used. Figure 1.2 in the previous chapter illustrates the process. Briefly, the collimated output beam of a mode-locked titanium:sapphire laser, tuned to 740 nm (Coherent Mira 900), was focused onto an electrically actuated scan mirror that scanned the beam in a raster pattern through a series of lenses onto a 800 x 600 (SVGA) digital micromirror device (DMD). The DMD was controlled by a computer displaying binary mask images, where micromirrors on the DMD corresponding to the white pixels of the mask image directed the beam into the back aperture of a 100X (1.3 NA) Zeiss Fluar oil microscope objective. Due to this selective exposure, only the areas of the focal plane corresponding to the white areas of the mask resulted in photocrosslinking within the precursor solution and resulted in the fabrication of a hydrogel replicate of the mask image.

One-layer thick, 30 x 35 μm rectangular slabs of hydrogel from several precursor solutions were fabricated, using a #1 glass coverslip as the substrate. The laser wavelength was tuned to 740 nm and the power was adjusted to 15-25 mW, measured at the back aperture of the objective. Each slab area was scanned 2 or more times with the fabricating laser to ensure a crosslink density high enough to form a solid structure. After fabrication, all structures were rinsed 10 times with 50 μL HBS to remove the precursor solution.

3.3.3 Atomic force microscopy measurements

An Asylum MFD-3D-BIO AFM was used to acquire deflection vs. displacement curves representing the contact between a bead-tipped silicon cantilever and the hydrogel slabs (Figure 3.2). The cantilevers used were primarily Mikromasch NSC12 tipless

silicon cantilevers with a Cr-Au coating to provide additional reflectivity. The spring constants of the cantilevers used were typically 3-15 N/m. Also used were some higher spring constant cantilevers, Nanosensors TL-NCH-SPL tipless cantilevers, with typical spring constant 20-40 N/m. A silica bead with diameter 2-5 μm was attached to the end of each cantilever using UV-curable cement (Adhesive 61, Norland Optical).

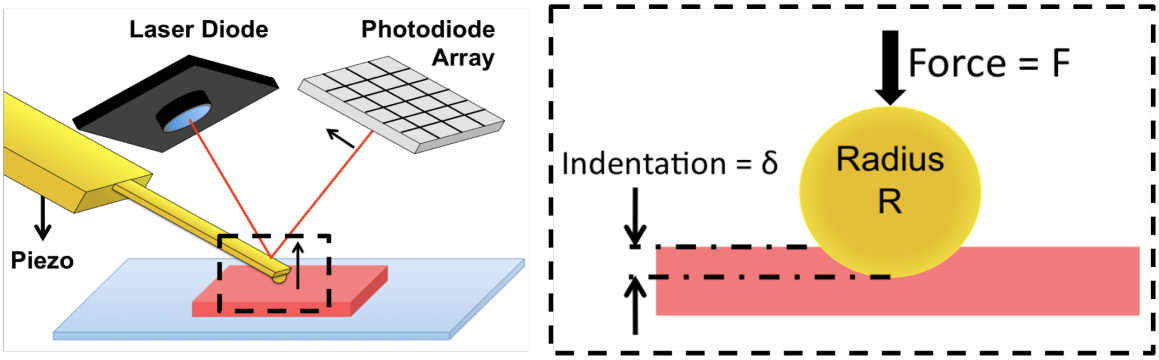

Figure 3.2 – Acquisition of deflection vs. displacement curves on the AFM. Left: Schematic of force measurements. The laser beam is reflected off of a bead-tipped cantilever onto a photodiode array. As the z-axis piezoactuator drives the bead down into the sample, the cantilever is deflected. This deflection is sensed by the photodiode array as a voltage signal that (with the proper calibration constants) can be used to derive the force applied by the bead to the gel, and the resulting indentation (δ) of the gel. Right: Indentation and force are used, along with the radius of the bead, to calculate the Young's modulus (E) of the sample via the Hertz model, which states force (F) as a function of $\delta^{(3/2)}$, where the modulus is a proportionality constant.

Deflection vs. displacement curves were acquired in triplicate at four separate locations on each hydrogel slab to determine modulus. Reference curves were also acquired at four corresponding locations on the glass substrate next to the slab, and were used to determine cantilever sensitivity and hydrogel slab thickness.

3.3.4 Calculation of Young's moduli

A Hertz-based indentation model was applied to the deflection vs. displacement curves, using MATLAB to apply Eq. 2 as discussed above. Three curves from each location were averaged to reduce point-to-point variation; the averaged curves were then fitted to the thickness-adjusted Hertz equation. Because the model is dependent on correct identification of the point of contact, an iterative fitting approach was applied, in which the user identified a range of likely contact points, and the program returned a goodness-of-fit (r^2) value for each assumed contact point. These r^2 values aided the selection of the correct contact point. All modulus data presented here are derived from fits with $r^2 > 0.99$.

3.3.5 Validation of system

The system was validated with a test hydrogel formed using 80 mg mL^{-1} polyvinyl alcohol (PVA, Sigma P-1763) solution crosslinked with glutaraldehyde (GDA, Ted Pella 18426) at a 100:1 PVA monomer to GDA molar concentration in HBS. The liquid polymer was used to fill a ~1 mm deep well, and also applied to a poly-D-lysine (PDL) coated glass coverslip held at a near-vertical angle, so that the glass-hydrogel boundary formed a gradual slope. Chemical gelation occurred over ~1.5 hours, during which the nascent hydrogels were stored at room temperature in sealed containers with 100% humidity. After gelation, hydrogels were kept submerged in HBS.

Selecting sample regions that included the glass-hydrogel boundary, measurements were acquired on a gel of uniform composition at different thicknesses (Figure 3.3) using the AFM. Measurements were acquired in two regions. Each region had 16 points from which measurements were acquired. At each point, three curves were acquired and averaged to reduce noise in the measurement. The measurements were used to calculate the Young's modulus at each of the points using both an uncorrected Hertz

model (based on equation 3.1) and a Hertz model with the finite-thickness correction applied (based on equation 3.2). Measurements acquired from points where the gel thickness was not allowed by the model ($h \geq 12.8*R$ or $h \leq 0.1*R$), measurements where it was clear that the no-slip assumption did not hold, and measurements where $r^2 < 0.99$ were not considered. Statistical analyses (f-test and t-test) were performed using Microsoft Excel.

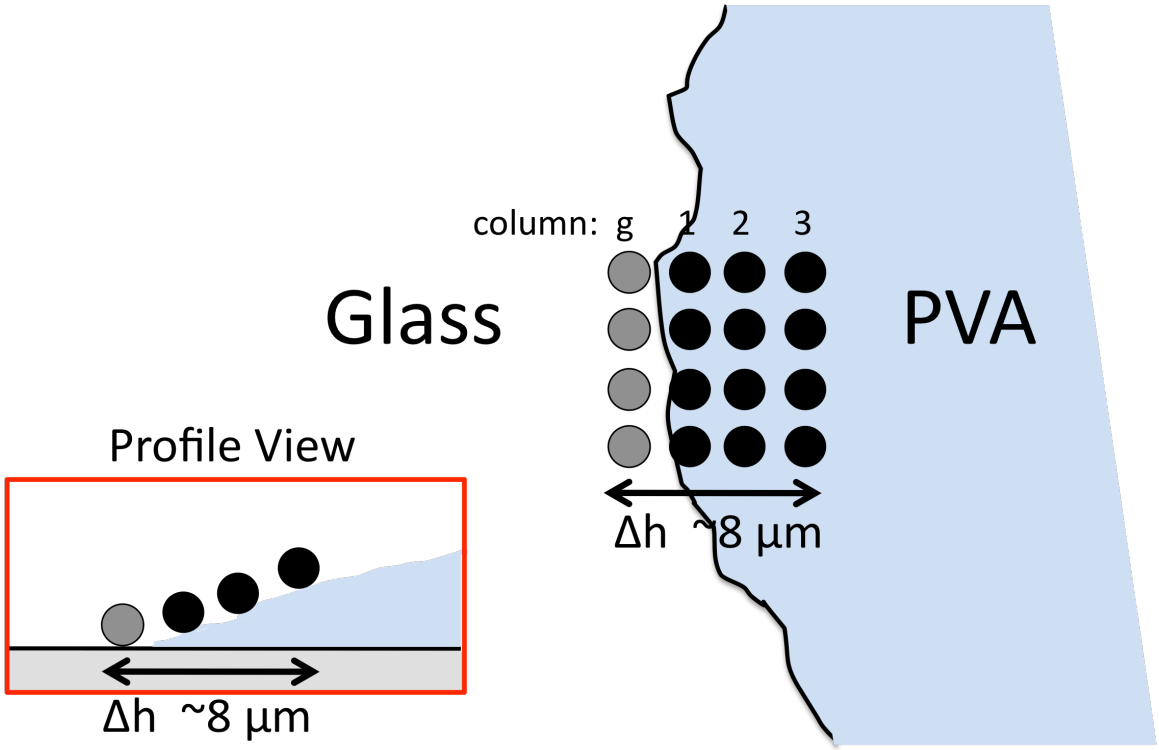

Figure 3.3 – Schematic showing acquisition of validation data for the finite-thickness Hertz model. A square region ~8 μm on a side was selected and 16 points (● or ○) were selected for force curve acquisition. One column of points (○, column *g*) was positioned to contact the glass substrate, providing a reference point for thickness measurements. Each succeeding column of points (●, columns *1-3*) was positioned so that measurements were acquired from a region where the hydrogel was thicker than the preceeding column. Inset shows the profile of the glass-hydrogel boundary, with a representative contact point from each column.

3.4 RESULTS AND DISCUSSION

When the precursor solution used in multiphoton lithography contains more than one type of crosslinking molecule, a hybrid hydrogel is fabricated, assuming that the crosslinking chemistry is not incompatible between the molecules in solution. Because of the different spatial arrangements of molecules made possible by a mixed solution, it can be hypothesized that both molecular packing and crosslink density would be affected in a hydrogel fabricated from this solution.

By altering the weight ratio of GMHA in aqueous precursor solutions of BSA or PEGDA, the Young's modulus values of the resulting hydrogel structures were tuned over values generally found in biological tissue (~1-1000 kPa).

3.4.1 Validation of finite-thickness Hertz model

The validation study showed that for finite hydrogel thicknesses ($0.1*R < h < 12.8*R$), application of the finite-thickness correction resulted in more accurate measurements of the Young's modulus of the PVA hydrogel (Figure 3.4).

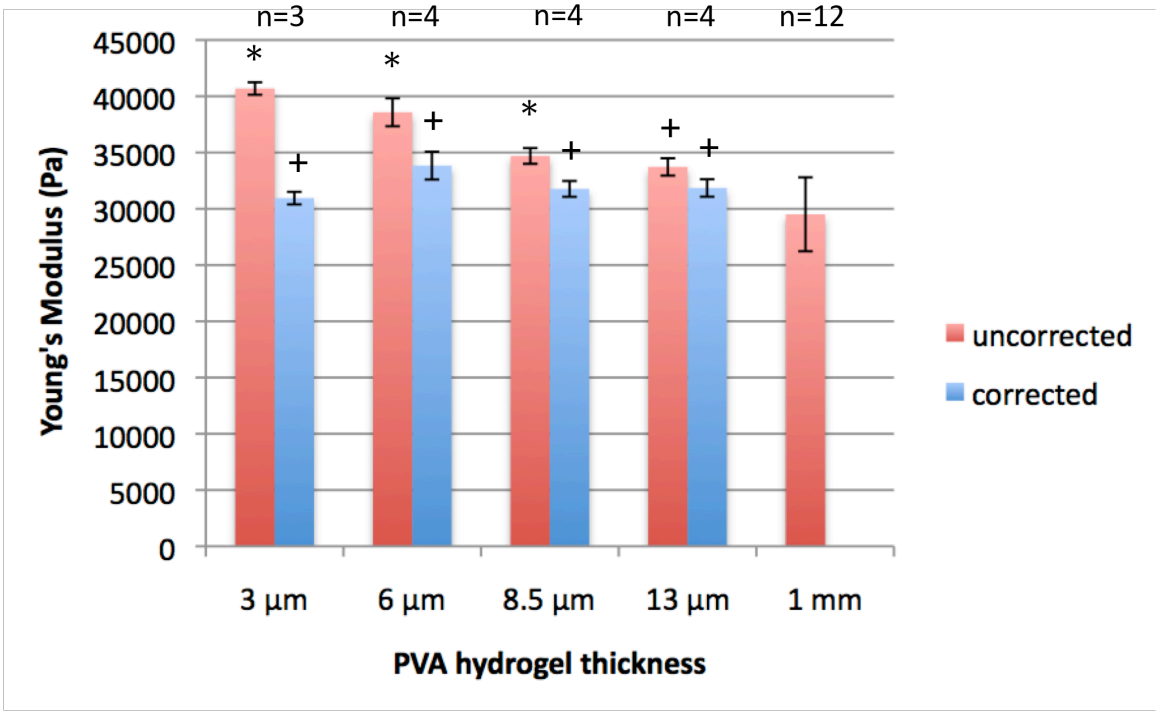

Figure 3.4 – Validation of finite thickness model. Young's modulus measured for different thicknesses (h) of PVA hydrogel, using an indenter (bead) with R = 1 μm. Uncorrected values are calculated using equation 3.1, corrected values are calculated using the same data and equation 3.2. When compared with 1 mm measurement, "+" denotes $p > 0.01$, "*" denotes $p < 0.01$. Error bars are standard deviation of the Young's modulus for a given group.

Data for the 1 mm thick hydrogel are not corrected because the sample can be considered to have semi-infinite thickness ($h >> R$). Using the 1 mm measurement as a standard, statistical analysis shows that corrected values at all other thicknesses are not significantly different (+, $p > 0.01$) from the standard, while uncorrected values for most other thicknesses are significantly different (*, $p < 0.01$), when a two-tailed t-test is applied. All corrected moduli are calculated using the thickness of the gel at the point of bead contact, however each labeled thickness on the graph is the mean thickness for a group of similar points, rounded to the nearest 0.5 μm. Actual mean and standard deviation values are: 2.91 ± 0.04 μm; 5.79 ± 0.35; 8.43 ± 0.10 μm; 12.82 ± 0.26 μm.

3.4.2 Effect of GMHA on the moduli of BSA-GMHA hydrogels

Initial attempts to alter the modulus of MPL-fabricated hydrogels focused on BSA hydrogels, due to the prevalence of BSA in previous work using MPL. Figure 3.5 shows the moduli of 20%* BSA hydrogels made with differing percentages of GMHA (0-5%) and 0.5% Rose Bengal (or approximately 5 μmol g^{-1}) as the photosensitizer. All hydrogels were fabricated at constant power (18 mW as measured at the back aperture), using scan parameters that ensured uniform fabrication.

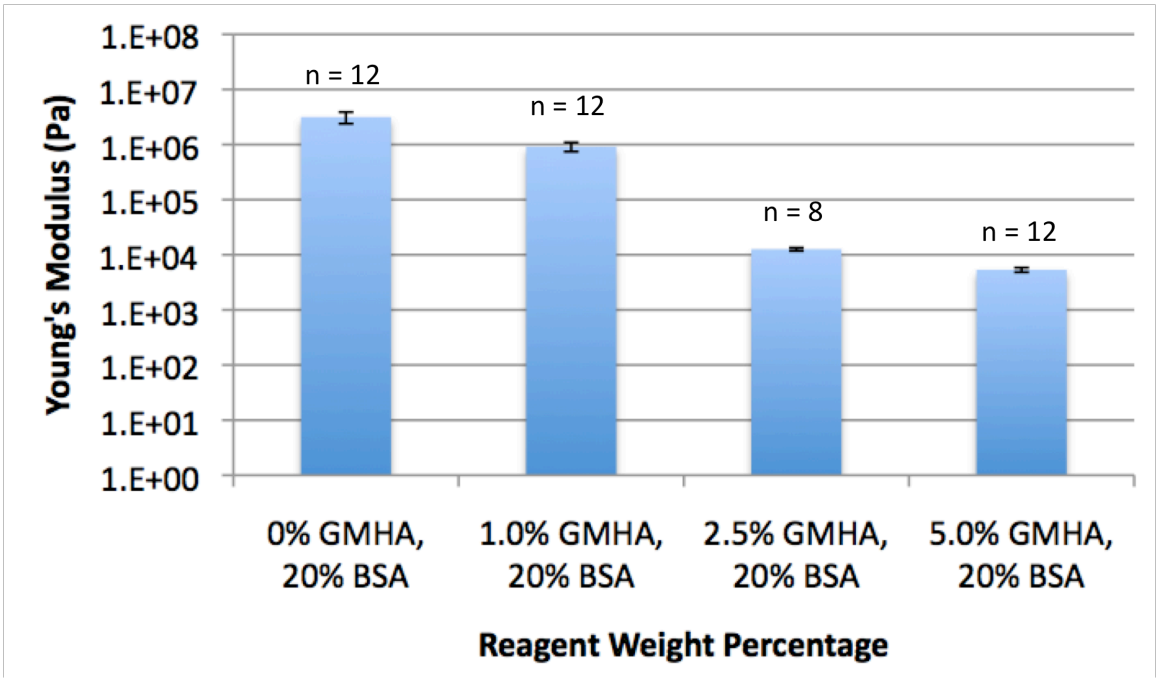

Figure 3.5 – Moduli of BSA hydrogels containing differing concentrations of GMHA. Hyaluronic acid has been found to form low modulus (1-10 kPa) hydrogels, and these results suggest that it lowers the moduli of BSA hydrogels when the polymers are mixed in solution prior to fabrication. All error bars represent the standard deviation in the Young's modulus for the samples used. Vertical axis is on a logarithmic scale.

* All following percentages represent the weight of the stated solute divided by the weight of the solution (w/w) x 100%, unless otherwise noted

As anticipated, increasing weight percentage of GMHA decreased the modulus of the resulting MPL-fabricated hydrogel. Under the particular fabrication parameters used, the addition of just 5% of GMHA resulted in a nearly 3 order-of-magnitude decrease in Young's modulus. This dramatic change in modulus is likely indicative of substantial changes in the arrangement of molecules and density of cross-links in the hydrogel.

BSA is a globular protein with a net negative charge under physiological conditions. While it possesses many binding pockets for hydrophobic molecules [11], overall it is highly water-soluble. At concentrations like those used in this dissertation, BSA is close to saturation in HBS. In contrast to BSA, GMHA is a repeating disaccharide chain with few hydrophobic regions. It has less inherent rigidity than BSA, and the presence of GMHA molecules in a precursor solution likely cause changes in the orientation of the BSA molecules closest to them. This could affect the type and quantity of crosslinks found in the resulting hydrogel, and may explain why the modulus decreases with the addition of GMHA.

3.4.3 Effect of GMHA on the moduli of PEG-GMHA hydrogels

PEG is a biomaterial that has generated interest as a scaffold material [20, 28] because it is non-toxic, non-immunogenic, non cell-adhesive, and has been approved for medical use [19]. It can be modified with proteins or other biomolecules using relatively straightforward chemistry, and is available in a large range of molecular weights and branching configurations. The modulus of PEG hydrogels can be adjusted to some degree by changing the molecular weight of the PEG molecule used [9]. However, PEGDA is often used for tissue engineering applications in conjunction with other biomolecules [28-30], so it is useful to know how the combination of PEGDA with other molecules affects

the modulus when used in MPL. Because the PEGDA used in this study was only 700 Da, it was anticipated that the modulus of the resulting hydrogels would be high.

The structures shown in Figure 3.6 were all fabricated using a precursor solution with 28% PEGDA, and a much lower percentage of BSA (2.6%). The BSA was included so that the hydrogel microstructures would adhere to the glass substrate. Although the inclusion of BSA may have changed the overall modulus of the structures, the low effective molar concentration corresponding to the weight percentage used (0.4 μmol g^{-1}) suggests that this would be a small change, and constant throughout the experiment.

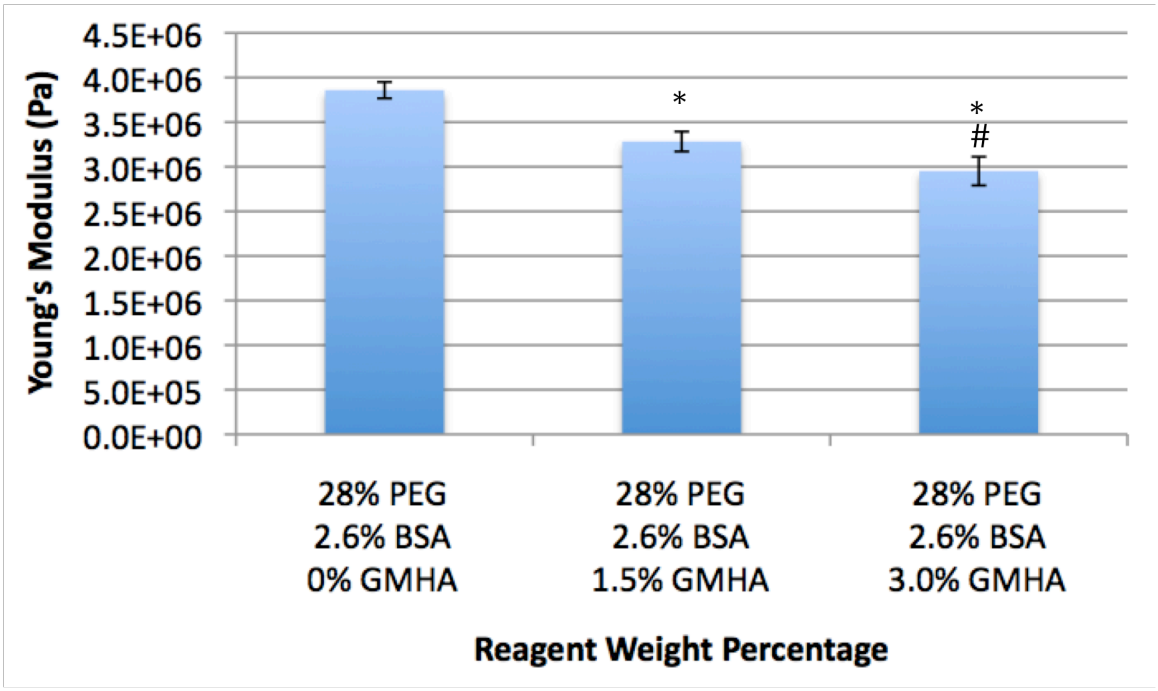

Figure 3.6 – Moduli of PEG hydrogels with differing concentrations of GMHA. Addition of GMHA reduces the moduli of PEG hydrogels. Hydrogels fabricated from solutions containing 1.5% or 3.0% GMHA had moduli that were significantly less than hydrogels with no GMHA ("*" denotes $p < 0.01$ relative to 0% GMHA). Hydrogels fabricated using 3.0% GMHA also had moduli significantly lower than hydrogels fabricated using 1.5% GMHA ("#" denotes $p < 0.05$ relative to 1.5% GMHA). A sample size of $n = 12$ was used for each hydrogel type, error bars represent the standard deviation from the mean modulus.

The inclusion of GMHA in the solutions proved difficult, due to the poor co-solubility of PEGDA and GMHA. The maximum weight percentage that could be attained in a solution of 28% PEGDA was 3% GMHA. This equates to 1.8 μmol g^{-1}, and, considering the high degree of methacrylation of the GMHA, proved a high enough concentration to significantly effect the modulus of the hydrogel. In fact, compared to the PEG hydrogel with no GMHA, hydrogels with either 1.5% or 3.0% GMHA had significantly lower moduli ($p < 0.01$ in a two-tailed, equal variance t-test). When compared to each other, the two PEG hydrogels with GMHA also had significantly

different moduli ($p < 0.05$ in a two-tailed, equal variance t-test). Taken together, it is clear that the addition of GMHA to the PEGDA precursor solution affects the modulus of the resulting hydrogel. It is interesting to note that the decrease in modulus noted from the addition of GMHA to the PEGDA hydrogels is much less, in relative terms, than the decrease noted from comparable proportions of GMHA in BSA hydrogels. This disparity could be explained by considering, once again, the arrangement of molecules at the time of fabrication. Because the PEGDA molecules are so small (700 Da) relative to the GMHA molecule (17 kDa), and because the density of potential crosslink sites on PEGDA is so much higher relative to BSA, we can expect the GMHA to affect the number and type of crosslinks between PEGDA molecules to a lesser degree than between BSA molecules.

3.5 Conclusions

These studies demonstrate the ability to significantly change the moduli of MPL-fabricated hydrogels based on relatively small changes to the concentration of GMHA in the precursor solution, and also the ability to detect these changes using AFM data via a finite-thickness Hertz model. By accounting for the thickness of the measured hydrogel, this method allows the rapid and accurate determination of hydrogel modulus at a scale that is not possible using most other testing methods, and is valid for a larger range of modulus values compared to the alternate AFM cantilever method used previously. Although the experiments completed here only begin to explore the possible parameter space, the PEGDA hydrogels are potentially quite useful, given that PEGDA has been previously used in so many biomedical applications [31-33]. The problems experienced in this chapter with the cosolubility of PEGDA and GMHA were primarily due to the high molar concentration of the low molecular weight PEGDA. Using a lower

concentration of PEGDA in the precursor solution would have the double benefit of reducing the density of the resulting hydrogel, and allowing more GMHA in the solution. PEGDA could also be used in solution with other proteins such as gelatin. The ability to tune BSA hydrogel moduli from 10^3-10^6 Pa is a promising start to fabricating more biomimetic scaffold materials. Other parameters of interest (e.g., HA molecular weight, sensitizer concentration, laser fluence) remain to be examined.

3.6 REFERENCES

1. Seidlits S.K., Khaing Z.Z., Petersen R.R., Nickels J.D., Vanscoy J.E., Shear J.B., Schmidt C.E., The effects of hyaluronic acid hydrogels with tunable mechanical properties on neural progenitor cell differentiation. *Biomaterials* **31**, 3930-3940 (2010).
2. Engler A.J., Sen S., Sweeney H.L., Discher D.E., Matrix elasticity directs stem cell lineage specification. *Cell* **126**, 677-689 (2006).
3. Chatterjee K., Lin-Gibson S., Wallace W.E., Parekh S.H., Lee Y.J., Cicerone M.T., Young M.F., Simon Jr C.G., The effect of 3D hydrogel scaffold modulus on osteoblast differentiation and mineralization revealed by combinatorial screening. *Biomaterials* **31**, 5051-5062 (2010).
4. Hadjipanayi E., Mudera V., Brown R.A., Guiding cell migration in 3D: a collagen matrix with graded directional stiffness. *Cell Motility and the Cytoskeleton* **66**, 121-128 (Mar, 2009).
5. Kostic A., Sap J., Sheetz M.P., RPTPalpha is required for rigidity-dependent inhibition of extension and differentiation of hippocampal neurons. *Journal of Cell Science* **120**, 3895-3904 (2007).
6. Moore S.W., Sheetz M.P., Biophysics of substrate interaction: Influence on neural motility, differentiation, and repair. *Developmental Neurobiology* **71**, 1090-1101 (2011).
7. Nielson R., Kaehr B., Shear J.B., Microreplication and Design of Biological Architectures Using Dynamic-Mask Multiphoton Lithography. *Small* **5**, 120-125 (2009).
8. Khripin C.Y., Brinker C.J., Kaehr B., Mechanically tunable multiphoton fabricated protein hydrogels investigated using atomic force microscopy. *Soft Matter* **6**, 2842-2848 (2010).
9. Temenoff J.S., Athanasiou K.A., Lebaron R.G., Mikos A.G., Effect of poly (ethylene glycol) molecular weight on tensile and swelling properties of oligo (poly (ethylene glycol) fumarate) hydrogels for cartilage tissue engineering. *Journal of Biomedical Materials Research Part B: Applied Biomaterials* **59**, 429-437 (2002).

10. Saha K., Keung A.J., Irwin E.F., Li Y., Little L., Schaffer D.V., Healy K.E., Substrate modulus directs neural stem cell behavior. *Biophysical Journal* **95**, 4426-4438 (2008).
11. He X.M., Carter D.C., Atomic structure and chemistry of human serum albumin. *Nature* **358**, 209-215 (1992).
12. Carter D.C., Chang B., Ho J.X., Keeling K., Krishnasami Z., Preliminary crystallographic studies of four crystal forms of serum albumin. *European journal of biochemistry / FEBS* **226**, 1049-1052 (1994).
13. Kaehr B., Allen R., Javier D.J., Currie J., Shear J.B., Guiding neuronal development with in situ microfabrication. *Proceedings of the National Academy of Sciences* **101**, 16104-16108 (2004).
14. Seidlits S.K., Schmidt C.E., Shear J.B., High-Resolution Patterning of Hydrogels in Three Dimensions using Direct-Write Photofabrication for Cell Guidance. *Advanced Functional Materials* **19**, 3543-3551 (2009).
15. Allison D.D., Grande-Allen K.J., Review. Hyaluronan: a powerful tissue engineering tool. *Tissue Engineering* **12**, 2131-2140 (2006).
16. Leach J., Schmidt C., Austin T., Photocrosslinkable Hyaluronic Acid Hydrogels for Tissue Engineering. *Materials Research Society Symposium Proceedings*, (2004).
17. Leach J.B., Bivens K.A., Patrick C.W., Schmidt C.E., Photocrosslinked hyaluronic acid hydrogels: Natural, biodegradable tissue engineering scaffolds. *Biotechnology and Bioengineering* **82**, 578-589 (2003).
18. Park Y.D., Tirelli N., Hubbell J.A., Photopolymerized hyaluronic acid-based hydrogels and interpenetrating networks. *Biomaterials* **24**, 893-900 (2003).
19. Peppas N.A., Keys K.B., Torres-Lugo M., Lowman A.M., Poly (ethylene glycol)-containing hydrogels in drug delivery. *Journal of Controlled Release* **62**, 81-87 (1999).
20. Miller J.S., Shen C.J., Legant W.R., Baranski J.D., Blakely B.L., Chen C.S., Bioactive hydrogels made from step-growth derived PEG-peptide macromers. *Biomaterials* **31**, 3736-3743 (2010).
21. Nowatzki P.J., Franck C., Maskarinec S.A., Ravichandran G., Tirrell D.A., Mechanically tunable thin films of photosensitive artificial proteins: preparation and characterization by nanoindentation. *Macromolecules* **41**, 1839-1845 (2008).
22. Lin D.C., Dimitriadis E.K., Horkay F., Elasticity of rubber-like materials measured by AFM nanoindentation. *eXPRESS Polymer Letters* **1**, 576-584 (2007).
23. Hertz H., Ueber die Berührung fester elastischer Körpe. *Journal für die reine und angewandte Mathematik*, (1882).
24. Johnson K.L., *Contact mechanics*. (Cambridge University Press, 1987).
25. Johnson B.D., Beebe D.J., Crone W.C., Effects of swelling on the mechanical properties of a pH-sensitive hydrogel for use in microfluidic devices. *Materials Science and Engineering: C* **24**, 575-581 (2004).

26. Dimitriadis E.K., Horkay F., Maresca J., Chadwick R.S., Determination of elastic moduli of thin layers of soft material using the atomic force microscope. *Biophysical Journal* **82**, 2798-2810 (2002).
27. Ritschdorff E.T., Nielson R., Shear J.B., Multi-focal multiphoton lithography. *Lab on a Chip* **12**, 867-871 (2012).
28. Leach J.B., Bivens K.A., Collins C.N., Schmidt C.E., Development of photocrosslinkable hyaluronic acid-polyethylene glycol-peptide composite hydrogels for soft tissue engineering. *Journal of Biomedical Materials Research Part B: Applied Biomaterials* **70**, 74-82 (2004).
29. Leach J.B., Schmidt C.E., Characterization of protein release from photocrosslinkable hyaluronic acid-polyethylene glycol hydrogel tissue engineering scaffolds. *Biomaterials* **26**, 125-135 (2005).
30. Gittard S.D., Ovsianikov A., Akar H., Chichkov B., Monteiro-Riviere N.A., Stafslien S., Chisholm B., Shin C.-C., Shih C.-M., Lin S.-J., Su Y.-Y., Narayan R.J., Two Photon Polymerization-Micromolding of Polyethylene Glycol-Gentamicin Sulfate Microneedles. *Advanced Engineering Materials* **12**, B77-B82 (2010).
31. Kutty J.K., Cho E., Soo Lee J., Vyavahare N.R., Webb K., The effect of hyaluronic acid incorporation on fibroblast spreading and proliferation within PEG-diacrylate based semi-interpenetrating networks. *Biomaterials* **28**, 4928-4938 (2007).
32. Larsson A., Ekblad T., Andersson O., Liedberg B., Photografted poly (ethylene glycol) matrix for affinity interaction studies. *Biomacromolecules* **8**, 287-295 (2007).
33. Zamanian B., Masaeli M., Nichol J.W., Khabiry M., Hancock M.J., Bae H., Khademhosseini A., Interface-Directed Self-Assembly of Cell-Laden Microgels. *Small* **6**, 937-944 (2010).

Chapter 4: Functionalization of hydrogels fabricated using multiphoton lithography

4.1 Introduction

Researchers have systematically studied the effect of specific biomolecules on animal cells for well over 100 years [1], and in that time have made discoveries that have not only improved scientific understanding of biological systems, but also contributed to revolutionary improvements in the practice of medicine and public health. Nevertheless, there are areas of medical treatment that have not benefitted in proportion to the increase in general knowledge, usually due to the absence of an efficient delivery method. Although "drug delivery" is generally understood as a sub-field within biomedical engineering, the meaning here is much broader. While often thought of as a question of getting a mobile drug safely, and in sufficient quantity, to a specific location in the body, it can also be applied to describe the problem of placing a given biomolecule in its proper spatial context, so that cells recognize it as an integral part of their microenvironment. In this broader sense, many unresolved tissue engineering problems can be thought of as delivery problems, including some of the challenges associated with developing an effective peripheral nerve guide. While the Schwann cell basal laminae provide uninterrupted topography to guide extending axons [2], they also provide axons with important chemical cues [3]. Therefore, when considering multiphoton lithography (MPL) for tissue engineering applications of this sort, techniques must be developed that enable fabricated structures to present chemical cues in conjunction with the topographical and mechanical cues already discussed. Two strategies to achieve this goal are presented here.

The first strategy includes the desired target biomolecule (or a variant that has been made photolabile) in the hydrogel precursor solution. The amount of target biomolecule in the resulting hybrid hydrogel is adjusted by varying either the concentration of the target molecule in the precursor solution, or by varying the laser fluence used to fabricate the hydrogel. In a fundamental demonstration of this approach, Kaehr et al. fabricated functional structures using biotinylated BSA (b-BSA) as the target molecule in hydrogels consisting mostly of non-biotinylated BSA. They demonstrated that immobilized gradients of b-BSA could be produced by altering the laser fluence during the fabrication process [4]. Unfortunately, this change in laser fluence during fabrication also results in morphological and mechanical changes in the hydrogel. In the work presented below (Paragraph 4.3.1), this general approach is used to fabricate BSA hydrogels functionalized with GMHA. In this case gradients were not desired, the goal was rather to fabricate hybrid hydrogels using fundamentally different biomolecules as building blocks. The question of gradients, and how they can be established without otherwise significantly affecting the topography or elasticity of the hydrogel is an important one [5] however, so a second strategy was conceived.

The second strategy is a two-step process that decouples functionalization from fabrication. It selectively immobilizes target biomolecules on an MPL-fabricated hydrogel with micron-scale spatial resolution, and without significant changes to the micron-scale topography of the hydrogel. This approach allows independent design of the topographical features and chemical gradients of the MPL-fabricated hydrogels. Both steps of this procedure require the use of a pulsed laser beam to generate multiphoton excitation. However, since the two steps require different ranges of laser fluence, and use different photolabile molecules in solution, they are essentially independent processes. The first step of the procedure is the fabrication of a micron-scale hydrogel, described in

earlier chapters and in the literature [6, 7]. In the second step of the process, a tunable pattern of the target biomolecule (here, biotin) is immobilized on the surface of the microstructure using a biotin conjugate, benzophenone-biotin (BP-biotin), which is attached to the pre-existing hydrogel using multiphoton excitation. Because BP can insert itself into C-H bonds [8], it is particularly suitable for the functionalization of biological hydrogels, given the number of C-H bonds available. Although this general approach has been previously demonstrated with different chemistries [9-11], this is the first attempt to combine the technique with MPL-fabricated microstructures. This approach allows independent control over both the physical and chemical microenvironment of cells.

Here, functionalization of hydrogels is demonstrated using each method. First, hybrid hydrogels of BSA, functionalized with glycidyl methacrylate hyaluronic acid (GMHA), were tested for tunability and stability over time. Next, both BSA and polyethylene glycol diacrylate (PEGDA) hydrogels were selectively functionalized with biotin. Each functionalization approach has unique challenges and benefits, which are discussed in the context of tissue engineering applications.

4.2 MATERIALS AND METHODS

All solutions were prepared in a simplified HEPES buffered saline (HBS) solution, containing 0.02 M HEPES (Sigma, H3375) and 0.1 M NaCl, as the solvent. All materials were used as received, with the exception of b-BSA, GMHA and fluorescein-GMHA (f-GMHA) conjugate. BSA (Equitech Bio, BAH64) was conjugated to biotin using a commercial biotin-succinimide (Marker Gene Tech., M0785) and standard protocols. 17 kDa hyaluronic acid (HA10K, Lifecore Biomed.) was methacrylated to GMHA using the protocol described previously [12], except that dialysis against deionized water was used instead of acetone precipitation to purify the synthesized

GMHA prior to lyophilization. A nuclear magnetic resonance spectrum of the GMHA indicated 10-15% methacrylation of the polymer. Fluorescein was conjugated to carboxyl groups on GMHA using aminofluorescein (Molecular Probes, A-6255) in a 1-ethyl-3-(3-dimethylaminopropyl)carbodiimide (EDC, Aldrich, 161462) mediated reaction described in Leach et al. for the conjugation of peptides to GMHA [13].

4.2.1 Fabrication of GMHA functionalized BSA hydrogels

A stock solution of flavin adenosine dinucleotide (FAD, Acros Organics, 347212500) was prepared in HBS at a weight percentage of 4.0%*. A stock solution of BSA was prepared at a weight percentage of 29% in HBS. The BSA used was a 10:1 mixture of BSA:b-BSA. A stock solution of GMHA was prepared at 17% in HBS. The GMHA used in this stock was a 10:1 mixture of GMHA:f-GMHA.

From these three stock solutions, three experimental precursor solutions were prepared. The control solution contained 19% BSA, 0.60% FAD (7.6 μmol g^{-1}) and no GMHA. A high GMHA concentration solution was prepared that contained 19% BSA, 0.60% FAD and 3% GMHA. A low GMHA concentration solution was prepared that contained 19% BSA, 0.60% FAD and half the concentration of GMHA as the high concentration solution (~1.5%). The three soulutions were used to fabricate single-layer rectangular hydrogel slabs, 10 μm by 250 μm, using the stage scanning fabrication method. A Q-switched, doubled (532 nm) Nd:YAG laser (JDS Uniphase, NG 10320-110) at 5 mW average power (as measured before entering the microscope) was used for fabrication, and a 60X (1.4 NA) objective was used to focus the light. A nanopositioning stage (Physik Instrumente, E-710) mounted on a Nikon Eclipse TE2000 inverted microscope, was programmed using LabView (National Instruments) to move in a raster

* All following percentages represent the weight of the stated solute divided by the weight of the solution (w/w) x 100%, unless otherwise noted.

pattern at a velocity of either 25 or 50 μm s^{-1}. The raster dimensions were selected so that succeeding lines of the pattern overlapped (1 μm step between lines), creating a relatively continuous surface. Three slabs were fabricated at each scan velocity using each precursor solution.

4.2.2 Wide field fluorescence microscopy of GMHA functionalized BSA hydrogels

All hydrogel slabs were rinsed 10 times with 250 μL HBS and initial fluorescence images were visualized using a Zeiss Axiovert 135 micoscope with a 40X (0.75 NA) objective (Olympus, UPlanFl). Standard red (Chroma, 49004) and green (Chroma, 49011) filter sets were used with an attached Zeiss HBO-100 mercury arc lamp to generate fluorescence. A Hamamatsu C4742-98 14-bit digital camera was used to acquire images, which were saved as tagged image files (.tif) using Metamorph software (Universal Imaging Corp.). The camera binning was set to 1 and exposure time was 250 ms for all fluorescence images.

After initial images were acquired, all hydrogel slabs were incubated at room temperature for 18 hours in ~2 μM NeutrAvidin-TMR conjugate (NAv-TMR, Invitrogen, A6373), in order to fluorescently lable the b-BSA. The hydrogel slabs were then rinsed 10 times with 250 μL HBS, and fluorescence images were once again acquired. Hydrogel slabs were stored at 4°C, and fluorescence images were acquired periodically. At every time point, "blank" images were acquire with no sample on the stage for each filter set. This was used to ensure that there was no significant change in the combined noise and background of the images.

4.2.3 Analysis and quantification of fluorescence images of GMHA-functionalized BSA hydrogels

Image files were analyzed using ImageJ software (Wayne Rasband, Natl. Inst. Health). A central region of each slab measuring 25 pixels by 500 pixels was selected, and the mean pixel value (between 0 and 16,383 for a 14 bit image) of each region was recorded for each of the slabs at each time point, for each filter set. The mean values were entered into a Microsoft Excel spreadsheet for statistical analysis and to generate graphs. All hydrogel slabs were fabricated using identical parameters (except for fabrication scan velocity and the concentration of GMHA in the precursor solution), and all fluorescence images were acquired using identical light and camera settings. Therefore, green channel fluorescence intensity was used as a measure of the relative amount of GMHA in a hydrogel, and red channel fluorescence was used as a measure of the relative amount of BSA. All raw pixel values were normalized relative to saturation (16,384 counts) for ease of presentation.

4.2.4 Fabrication of BSA and PEGDA hydrogels for biotin functionalization

Solutions of either 14% BSA with 0.20% (7.3 μmol g^{-1}) FAD or 16% BSA with 0.50% (10 μmol g^{-1}) FAD were made in HBS. A solution of 52% PEGDA with 0.20% (9.4 μmol g^{-1}) benzophenone (BP, Acros Organics, 219680) in HBS was also made. Fabrication was accomplished using the apparatus described in Section 4.2.1 above, with the laser power set to 5 mW. The scan velocity was 50 μm s^{-1} for BSA structures and 100 μm s^{-1} for PEGDA structures. Number 1 glass coverslips were used as the substrate for all hydrogels, and coverslips for PEGDA hydrogels were passivated prior to fabrication by soaking in a 0.01% poly-L-lysine (PLL, Sigma, P8920) solution. All hydrogel slabs were rinsed 10 times with 250 μL HBS after fabrication to remove uncrosslinked precursor solution.

4.2.5 Selective functionalization of BSA and PEGDA hydrogels with biotin

For the BSA hydrogel experiment, BP-biotin (Quanta Biodesign, 10267) was solubilized at 100 mM in DMSO, then diluted to 2.0 mM in HBS. This solution was added to wells containing some of the BSA hydrogel slabs, and selected regions of the slabs were exposed to the doubled Nd:YAG laser in a raster pattern, as during fabrication. The same apparatus was used for fabrication and functionalization, except that a 40X (0.65 NA) objective was used for functionalization. For some functionalization scans, power was held constant (1 mW) while the stage scan velocity was varied (20-120 μm s^{-1}). In other cases, the stage scan velocity was held constant (80 μm s^{-1}) while power was varied (between 1-4 mW). Control slabs were left in the HBS solution and exposed to the same laser scan patterns as the experimental structures. All structures were then rinsed 10 times with 250 μL HBS and incubated at room temperature for ~18 hours in 1 μg mL^{-1} NAv-TMR so that the regions with bound biotin could be analyzed using fluorescence microscopy. Prior to imaging, all structures were once again rinsed 10 times with 250 μL HBS solution to remove unbound NAv-TMR.

For the PEGDA hydrogel experiment, BP-biotin at 100 mM in DMSO was diluted to 10 mM in HBS, and then added to wells containing some of the PEGDA hydrogels. As with the BSA hydrogels, selected regions of the slabs were exposed to the doubled Nd:YAG laser light in a raster pattern. For the PEGDA hydrogel slabs, the stage scan velocity was held constant (100 μm s^{-1}) while average laser power was varied (between 2-5 mW). Control slabs were left in the HBS solution and exposed to the same laser scan patterns as the experimental structures. All structures were then rinsed 10 times with 250 μL HBS and incubated at room temperature for ~18 hours in 1 μg mL^{-1} NAv-TMR allowing the regions with bound biotin to be analyzed using fluorescence

microscopy. Prior to imaging, all structures were once again rinsed 10 times with 250 μL HBS solution to remove unbound NAv-TMR.

Images of the functionalized BSA and PEGDA hydrogels were acquired as described in section 4.2.2 above, using the red filter set.

4.2.6 Analysis of fluorescence images

Images were analyzed using ImageJ. An area of the image representing the biotin functionalized region of each hydrogel slab was selected, and a fluorescence profile was constructed by averaging the pixel values for each pixel column* in the selected area. This profile was exported to Microsoft Excel, where the data were used to construct scaled plots of normalized fluorescence. The data were normalized by dividing the pixel value by the pixel saturation value (16,464).

4.3 RESULTS

4.3.1 GMHA functionalized BSA hydrogels

When a scaffold does not require any spatial patterning or gradient of a desired target molecule, but may require specific average surface concentrations of the molecule, fabricating a hybrid hydrogel is the simplest course of action to accomplish functionalization. BSA and GMHA were selected to test hybrid hydrogel fabrication because they generally have low cytotoxicity and low immunogenicity, represent two common biomolecular classes (globular protein and linear polysaccharide), and have both proven reletively easy to photocrosslink in the past. As discussed in the methods section (paragraph 4.2.3), the experiments were designed so that red or green fluorescence could

* A pixel column is a vertical column of pixels from an image. If a line were drawn vertically through the center of any pixel on the top edge of an image, all the pixels that the line crossed would belong to one pixel column

be used as an indication of the relative concentration of BSA or GMHA (respectively) in the hydrogel.

4.3.1.1 Control structures without GMHA

The stability of BSA structures and the contributions from BSA and FAD autofluorescence to the green signal were assessed using structures fabricated without GMHA. Figure 4.1 shows that the amount of NAv-TMR bound to the b-BSA in the hydrogel slabs remains constant for at least 30 days post-fabrication for both scan velocities (Fig. 4.1 a), and that the intensity of BSA and FAD autofluorescence is low compared to the fluorescence emitted by the f-GMHA (Fig 4.1 b).

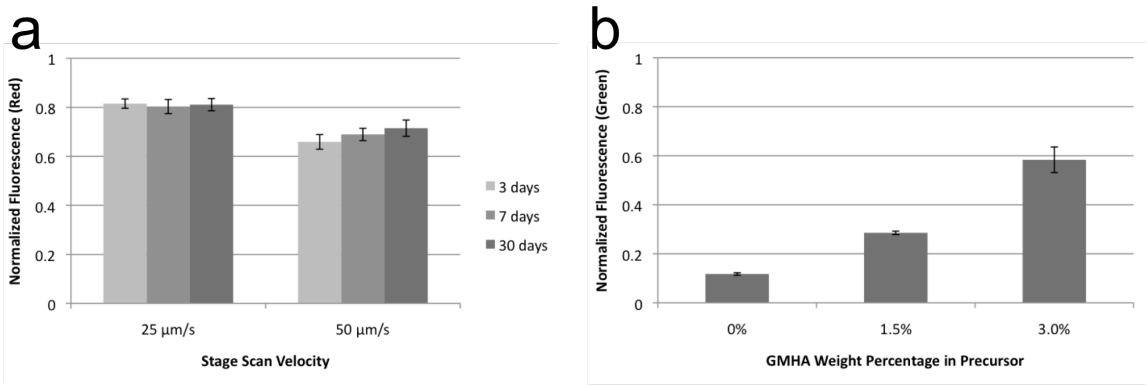

Figure 4.1 – Validation of fluorescence method for evaluating hydrogel stability. (a) Normalized intensity values of fluorescence images acquired using the red filter set show that, over the period examined, hydrogel slabs did not experience a significant reduction in fluorescence from the NAv-TMR bound to the b-BSA, indicating that the hydrogel mostly remained intact. (b) Normalized intensity values of fluorescence images acquired using the green filter set show that the contribution to the fluorescence signal from BSA and FAD autofluorescence (0%) is small relative to the signal from f–GMHA (1.5% and 3.0% in precursor). Fabrication velocity for "b" is 25 μm s^{-1}. All error bars represent the standard deviation of the sample set where n=3.

From this data, it is concluded that the green filter fluorescence is a reasonable way to monitor the presence of GMHA in the hydrogel slabs over time.

4.3.1.2 Concentration and stability of GMHA in BSA hydrogels

Results from the analysis of fluorescence images indicate that the fluorescein-labeled GMHA is incorporated into the structures, and that the GMHA remains in the structures for at least 30 days (Figure 4.2).

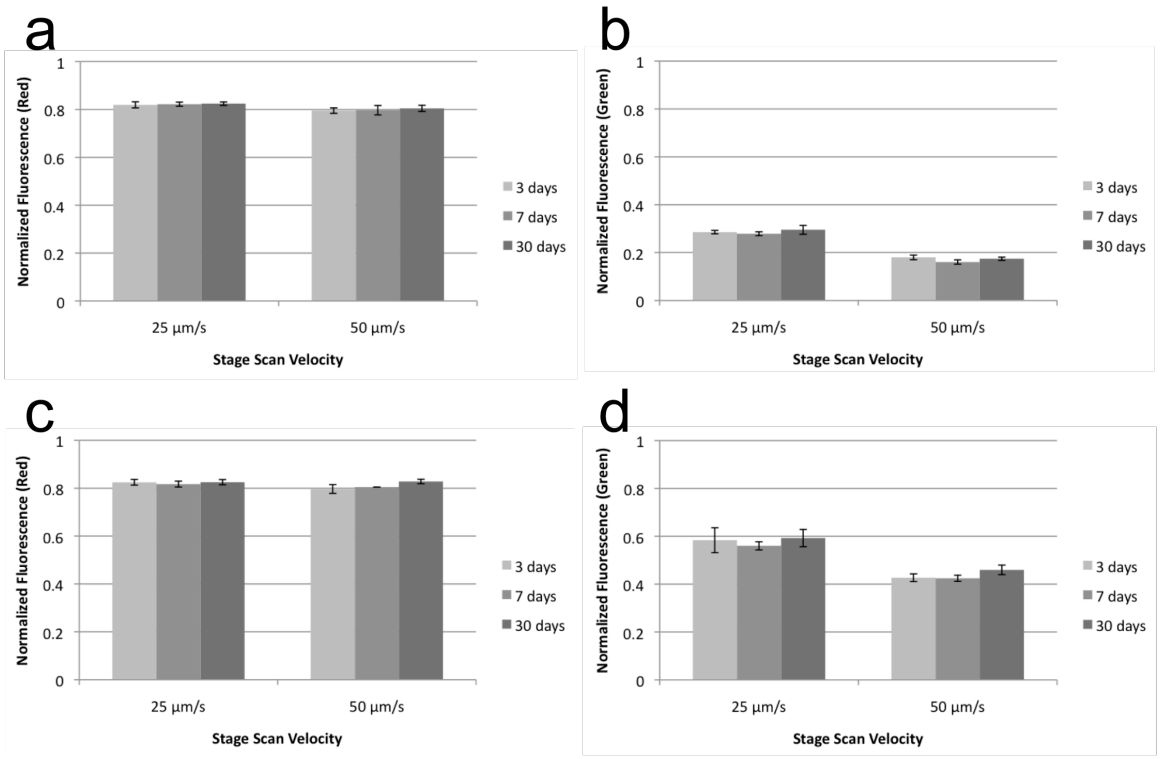

Figure 4.2 – Stability and tunability of GMHA functionalized BSA hydrogels. (a & c) Red filter fluorescence of NAv-TMR in BSA hydrogels fabricated with solutions of 1.5% (a) and 3% (c) GMHA, over a 30 day period post-fabrication. Because NAv-TMR is bound to b-BSA, it can be used to monitor degradation of the hydrogel slab. (b & d)Normalized green filter fluorescence of BSA hydrogels fabricated with solutions of 1.5% (b) and 3% (d) GMHA, over a 30 day period post-fabrication. This value is proporational to the amount of GMHA in a given hydrogel. Error bars represent standard deviation from the mean value (n=3).

Fluorescence acquired using the red filter was used to analyze the integrity of the structures over 30 days (Fig 4.2a and c). These measurements indicate that the hydrogel slabs did not degrade significantly over that time period.

Fluorescence acquired using the green filter was used to study the effect of fabrication scan velocity and precursor solution GMHA concentration on the presence of f-GMHA in the hydrogel slabs over 30 days (Fig 4.2b and d). When comparing the

amount of GMHA in slabs fabricated from a precursor solution of 1.5% GMHA (Fig 4.2.b) to those fabricated from 3% GMHA (Fig 4.2.d), the normalized green fluorescence signal indicates that the concentration of GMHA in the 3% slabs is still approximately twice the concentration of GMHA in the corresponding 1.5% slab. Therefore, the results show that for a given fabrication laser fluence, the amount of GMHA in the hydrogel can be tuned by changing the concentration of GMHA in the precursor solution. Furthermore, for a given concentration of GMHA in the precursor solution, the amount of GMHA in the hydrogel can be tuned by changing the fabrication laser fluence.

4.3.2 Tunable functionalization of BSA hydrogels

Although the selective and tunable binding of BP-biotin conjugate to hydrogel slabs is ultimately a function of laser fluence, it is accomplished in practical terms by varying either the stage scanning velocity or the laser power during functionalization. Due to the initial uncertainty associated with this parameter space, experiments were conducted both by varying the velocity (holding power constant) and by varying power (holding velocity constant) when functionalizing the slabs.

By stepping the functionalization scan velocity in 10 μm s^{-1} increments, while holding the average laser at 2 mW, an almost linear increase in biotin binding was achieved (Figure 4.3). It is important to note that there is no noticeable effect of the functionalization scan on the brightfield images of the hydrogel slab. Although this does not necessarily mean that the functionalization scan has no unintended effect on the hydrogel (in terms of topography or elasticity), it at least suggests that the changes, if any, are minor.

BSA slabs functionalized using the same range of scan velocities, but with constant 1 mW and 3 mW scan powers (not shown) show similar results over different

normalized fluorescence scales. Predictably, with the lower power (1 mW) series, there is a maximum scan velocity above which there is no biotin binding detected, although biotin binding may be occurring at a threshold too low to detect. At the other end of the scale, the higher power (3 mW) series, there is a scan velocity below which there is no noticeable increase in biotin binding. This is not a result of pixel saturation – it is most likely due to the fact that as more possible BP-biotin binding sites in the hydrogel are used, fewer are available for additional binding (although it is unlikely that all possible sites are used).

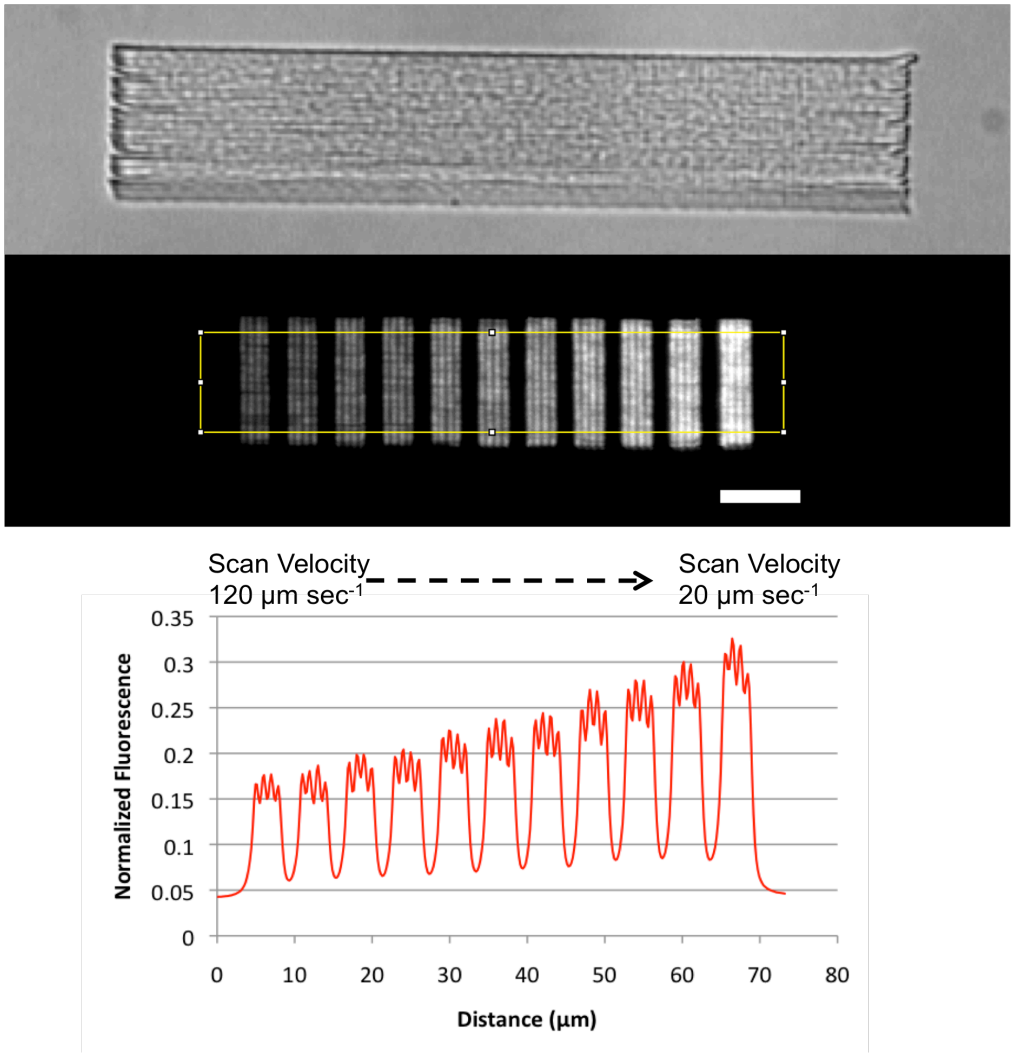

Figure 4.3 – Variable functionalization of a BSA hydrogel with biotin: varying scan velocity. Top: Slab of biotin functionalized BSA hydrogel imaged using brightfield microscopy. Middle: The same slab shown using wide field fluorescence imaging. Illuminated regions are biotin functionalized regions made visible by exposure to NAv-TMR. The degree of functionalization increases from left to right, as the functionalization scan speed increases from 20-120 μm s^{-1}. Bottom: Normalized fluorescence intensity from the boxed region of the middle image. Values represent the average value of each pixel column of the box, normalized by the maximum possible pixel value. Scale bar is 10 μm.

This hypothesis is partially validated by the results of the variable laser power functionalization experiment, conducted using a constant stage velocity (Figure 4.4). In this experiment, the stage velocity was 80 μm s^{-1} during the functionalization scans, while the average power of the laser was adjusted from 1-4 mW in 1 mW increments. It is interesting to note that while no change to brightfield image of the BSA slab is evident at 1 mW or 2 mW, there is slight vertical banding noticeable in the 3 mW region of the bright field image, and heavier vertical banding evident in the 4 mW region, indicative of physical changes to the hydrogel.

These experiments demonstrate that for BSA hydrogel, there is a range of stage scanning velocities (above the range that results in obvious physical changes to the hydrogel) where there is a near-linear relationship between stage scanning velocity and BP-biotin binding. Therefore, with the proper tools for patterning available, it should be possible to establish engineered patterns of arbitrary target molecules with micron-scale resolution.

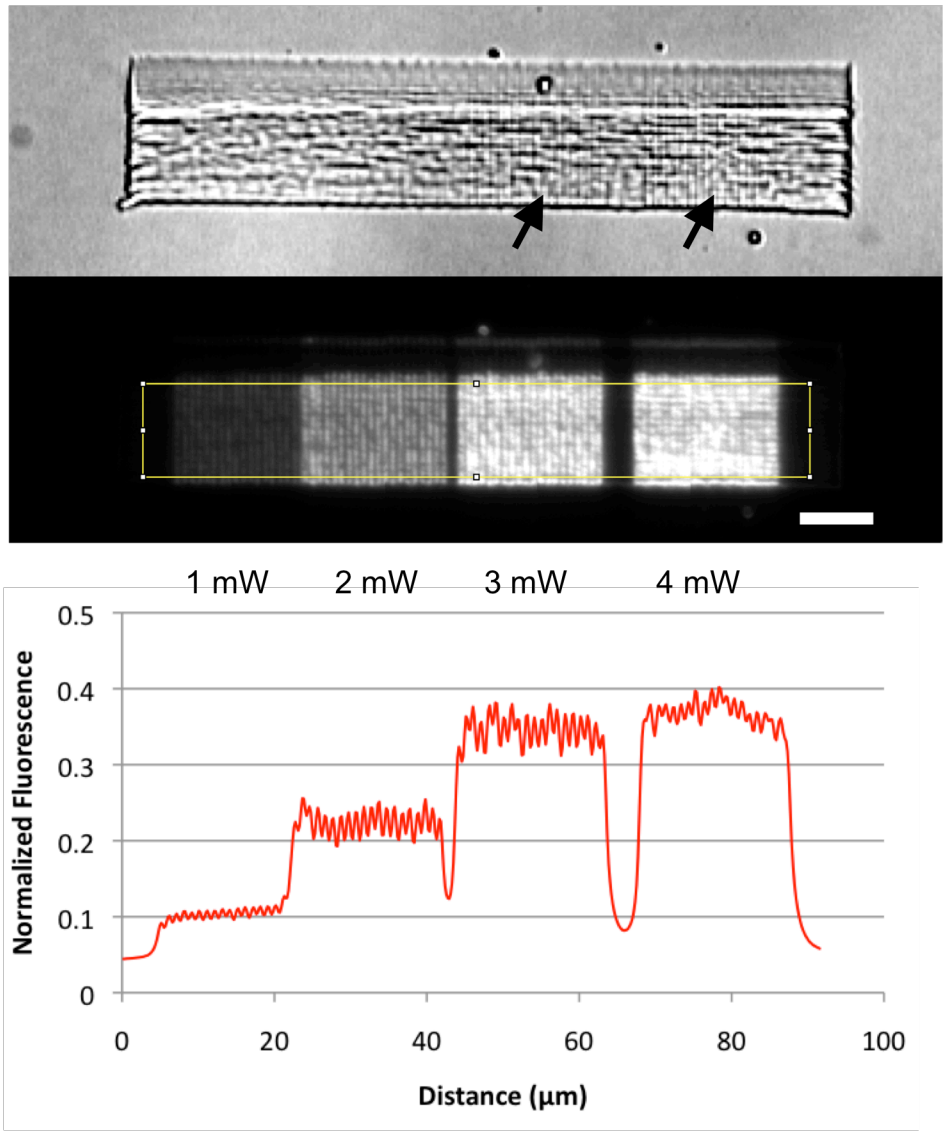

Figure 4.4 – Variable functionalization of a BSA hydrogel with biotin: varying scan power. Top: Block of biotin-functionalized BSA hydrogel imaged using brightfield microscopy. Black arrows indicate regions of hydrogel deformation due to functionalization scan. Middle: The same block shown using wide field fluorescence imaging. Illuminated regions are biotin-functionalized regions made visible by exposure to NAv-TMR. The degree of functionalization increases from left to right as the functionalization scan power increases from 1-4 mW. Bottom: Normalized fluorescence intensity from the boxed region of the middle image. Values represent the average value of each pixel column of the box, normalized by the maximum possible pixel value. Scale bar is 10 μm.

4.3.3 Tunable functionalization of PEGDA hydrogels

BSA is a useful biomaterial in many ways, and is generally considered appropriate for medical applications because it has low immunogenicity and is useful for binding and transporting a wide range of low-solubility molecules [14]. In some circumstances, however (including some tissue engineering applications), it may not be appropriate to use a protein that binds molecules present at low concentration in the body so efficiently. The high, localized concentration of BSA found in BSA hydrogels could cause a gradual accumulation of low solubility molecules in the hydrogel, with unknown outcome. As a result, other biomaterials have been studied as candidates for MPL, most notably PEGDA [15].

In this study, a low molecular weight (700 Da) version of PEGDA was selected in order to ensure a high concentration of crosslinking acryl groups. Solutions with weight percentages of PEGDA as low as 20% and as high as 60% have been used with various concentrations of different photosensitizers to fabricate micron-scale hydrogel structures. For the experiments described here, precursor solution with a weight percentage of 52% PEGDA and 0.2% BP as the photosensitizer was used.

When BP-biotin was used to functionalize PEGDA (Figure 4.5), it resulted in thorough, fluence-dependent functionalization of the hydrogel slab. Because all regions were scanned using 100 μm s^{-1}, the results suggest that with an average power of 4 mW, there is probably a range of scan velocities where a linear relationship between scan velocity and biotin binding exists. Additional experiments would elucidate this relationship between laser fluence and biotin binding for PEGDA hydrogels, as was

demonstrated above using BSA. There was no photodamage evident in the brightfield image of the PEGDA slab as a result of the functionalization scan.

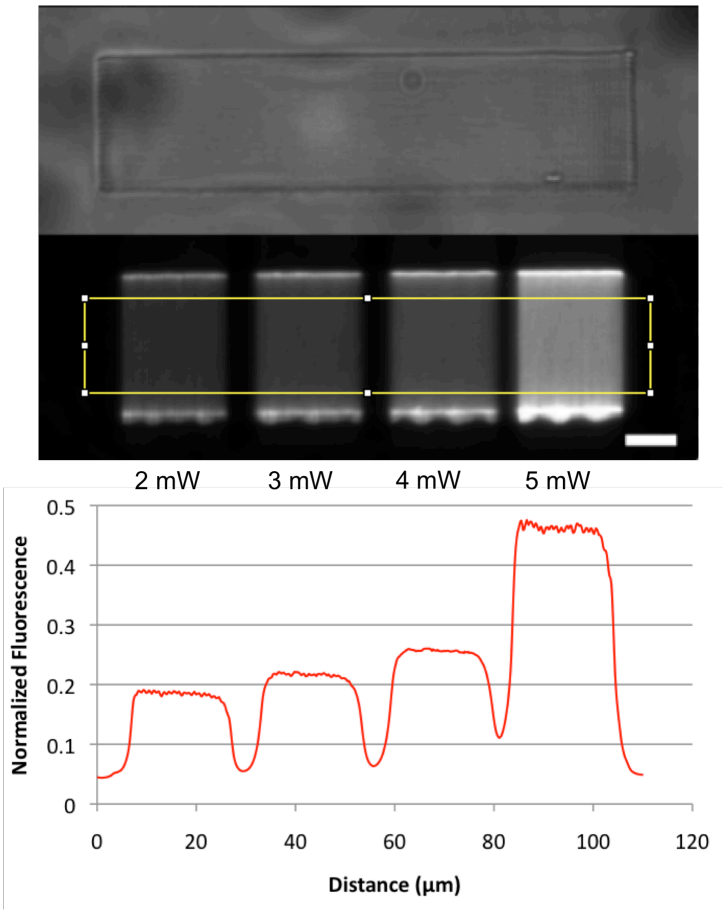

Figure 4.5 – Variable functionalization of PEGDA hydrogel with biotin: varying scan power. Top: Block of biotin-functionalized PEGDA hydrogel imaged using brightfield microscopy. Middle: The same block shown using wide field fluorescence imaging. Illuminated regions are biotin functionalized regions made visible by exposure to NAv-TMR. The degree of functionalization increases from left to right as the functionalization scan power increases from 2-5 mW. Bottom: Normalized fluorescence intensity from the boxed region of the middle image. Values represent the average value of each pixel column of the box, normalized by the maximum possible pixel value. Scale bar is 10 μm.

4.4 Conclusion

The ability to functionalize MPL-fabricated hydrogels extends the usefulness of these materials for a range of biomedical applications, including tissue engineering. This chapter shows that the functionalization of MPL-fabricated hydrogels can be tuned, both uniformly and with micron-scale patterning. This capability has been evaluated on MPL-fabricated BSA and PEGDA hydrogels using an indirect, fluorescence-based assay. While this assay is useful for demonstrating the capabilities of the functionalization methods, significant challenges remain with respect to using these methods to produce biologically relevant concentrations (or surface densities) of desired biomolecules on hydrogel structures of arbitrary geometry. Optical methods such as two-photon microscopy may be used to quantify the concentrations of fluorescently labeled functional molecules [11]. However, uncertainty in these measurements, combined with uncertainty as to the requirements of the cells involved, will necessitate an iterative approach to fully optimize the functionalization of hydrogel scaffolds for specific tissue engineering applications.

4.5 References

1. Ramon y Cajal S., *Histology of the nervous system of man and the vertebrates*. (Oxford University Press, New York, 1995), vol. 1. orig. pub. 1892, trans. N. Swanson, L. Swanson.
2. Nguyen Q.T., Sanes J.R., Lichtman J.W., Pre-existing pathways promote precise projection patterns. *Nature Neuroscience* **5**, 861-867 (2002).
3. Wang G.Y., Hirai K.I., Shimada H., The Role of Laminin, a Component of Schwann-Cell Basal Lamina, in Rat Sciatic-Nerve Regeneration Within Antiserum-Treated Nerve Grafts. *Brain Research* **570**, 116-125 (1992).
4. Kaehr B., Shear J.B., Mask-directed multiphoton lithography. *Journal of the American Chemical Society* **129**, 1904-1905 (2007).
5. Dertinger S.K.W., Jiang X., Li Z., Murthy V.N., Whitesides G.M., Gradients of substrate-bound laminin orient axonal specification of neurons. *Proceedings of the National Academy of Sciences* **99**, 12542-12547 (2002).

6. Kaehr B., Allen R., Javier D.J., Currie J., Shear J.B., Guiding neuronal development with in situ microfabrication. *Proceedings of the National Academy of Sciences* **101**, 16104-16108 (2004).
7. Nielson R., Kaehr B., Shear J.B., Microreplication and Design of Biological Architectures Using Dynamic-Mask Multiphoton Lithography. *Small* **5**, 120-125 (2009).
8. Dorman G., Prestwich G.D., Benzophenone photophores in biochemistry. *Biochemistry* **33**, 5661-5673 (1994).
9. Wosnick J.H., Shoichet M.S., Three-dimensional Chemical Patterning of Transparent Hydrogels. *Chemistry of Materials* **20**, 55-60 (2008).
10. Lee S.H., Moon J.J., West J.L., Three-dimensional micropatterning of bioactive hydrogels via two-photon laser scanning photolithography for guided 3D cell migration. *Biomaterials* **29**, 2962-2968 (2008).
11. Wylie R.G., Ahsan S., Aizawa Y., Maxwell K.L., Morshead C.M., Shoichet M.S., Spatially controlled simultaneous patterning of multiple growth factors in three-dimensional hydrogels. *Nature Materials* **10**, 799-806 (2011).
12. Seidlits S.K., Khaing Z.Z., Petersen R.R., Nickels J.D., Vanscoy J.E., Shear J.B., Schmidt C.E., The effects of hyaluronic acid hydrogels with tunable mechanical properties on neural progenitor cell differentiation. *Biomaterials* **31**, 3930-3940 (2010).
13. Leach J., Schmidt C., Austin T., Photocrosslinkable Hyaluronic Acid Hydrogels for Tissue Engineering. *Materials Research Society Symposium Proceedings*, (2004).
14. Carter D.C., Chang B., Ho J.X., Keeling K., Krishnasami Z., Preliminary crystallographic studies of four crystal forms of serum albumin. *European journal of biochemistry / FEBS* **226**, 1049-1052 (1994).
15. Jhaveri S.J., McMullen J.D., Sijbesma R., Tan L.S., Zipfel W., Ober C.K., Direct three-dimensional microfabrication of hydrogels via two-photon lithography in aqueous solution. *Chemistry of Materials* **21**, 2003-2006 (2009).

Chapter 5: Review and future work

5.1 Review of work

The techniques presented in this dissertation demonstrate that multiphoton lithography (MPL) can be used to fabricate intricate unconstrained and partially-constrained protein hydrogel microstructures. Fabricating these structures from proteins enhances their ability to interact with biological systems, making them uniquely suitable for a range of biomedical applications. Unconstrained hydrogel microparticles of specific geometry could open new possibilities in the area of drug delivery, where micron-scale hydrogels are currently limited to spheroids or simple geometric shapes like disks or pyramids [1-3]. The use of more unconventional geometries could be useful both for direct interaction with cells, and for designing new drug release profiles. When protogels are used with the combined scan fabrication technique, the fabrication of millimeter-scale hydrogels with micron-scale features is possible. These hydrogel structures could ultimately be used as scaffolds for tissue engineering, specifically in applications where cell-scale guidance is required over millimeter and centimeter distances, as it is in peripheral nerve guides [4].

The moduli of MPL-fabricated hydrogels can be adjusted by changing the relative weight percentages of crosslinking reagents in the precursor solution. These differences in moduli can be detected using atomic force microscopy (AFM) data via a finite-thickness Hertz model, which allows the rapid and accurate determination of hydrogel moduli at the micron scale. Although the experiments completed here only begin to explore the possible parameter space, the PEGDA hydrogels in particular may prove useful, given that PEGDA has been previously used in many biomedical applications [5-7].

MPL-fabricated hydrogels can be selectively functionalized, both as a whole and with micron-scale resolution. This capability was evaluated on BSA and PEGDA using an indirect, fluorescence-based assay, however these methods could eventually be used to produce biologically relevant concentrations of desired biomolecules on MPL-fabricated hydrogels. This would extend the usefulness of these hydrogels for many applications, including tissue engineering. Various studies have reported increased glial migration speed and neuronal outgrowth in the presence of biochemical cues [8, 9], including immobilized extracellular matrix (ECM) components. Although the simple presence of these cues in a regeneration matrix can enhance outgrowth, there is strong evidence that gradients of biomolecules also stimulate neurite outgrowth [10] and glial migration [11].

5.2 FUTURE WORK

Although future work has been discussed in each of the preceding chapters, other areas of work not directly related to the topics previously presented have been identified. In some of these areas, preliminary experiments have been conducted to gauge the feasibility of further study.

5.2.1 Lyophilization of hydrogels fabricated using multiphoton lithography

Given current limitations, MPL processes are not likely to improve to the point where a hypothetical therapeutic hydrogel could be fabricated "on demand" at the hospital bedside. It may be necessary to prepare such materials well in advance of need. For other potential applications of MPL-fabricated hydrogels, such as for drug delivery or in biosensors, the time between fabrication and use may be longer than the 30 day period over which some elements of hydrogel stability have already been evaluated (Paragraph 4.3.1 above). It is therefore necessary to consider the longer-term preservation and stability of MPL-fabricated hydrogels.

One way that the "shelf-life" of MPL-fabricated hydrogels could be extended is though the process of lyophilization. To assess this, a preliminary study was conducted that examined the ability of protein-based hydrogels to maintain both their function and original architecture after lyophilization and subsequent rehydration. The results of this study are presented in Figure 5.1. Specifically, a series of single-layer protein slabs comprised of either BSA or biotinylated-BSA (b-BSA) were fabricated, lyophilized, and rehydrated. One set of b-BSA hydrogels (Figure 5.1, Group 1) was incubated in a solution of NeutrAvidin-tetramethylrhodamine (NAv-TMR, 10 μg mL^{-1}) overnight prior to lyophilization, then lyophilized, and subsequently rehydrated. Conversely, a different set of b-BSA hydrogels (Figure 5.1, Group 2) were fabricated, lyophilized, then rehydrated and subsequently incubated in NAv-TMR (10 μg mL^{-1}) overnight.

From the data shown in Figure 5.1, it can be seen that the hydrogels conserve their architecture after lyophilization. In addition, biotin-BSA hydrogels that were exposed to NAv-TMR prior to lyophilization (Figure 5.1, Group 1) show the ability to retain NAv-TMR in the bound state through both lyophilization and rehydration. Finally, biotin-BSA hydrogels that were lyophilized, rehydrated, and then exposed to NAv-TMR maintained their ability to bind NAv-TMR (Figure 5.1, Group 2).

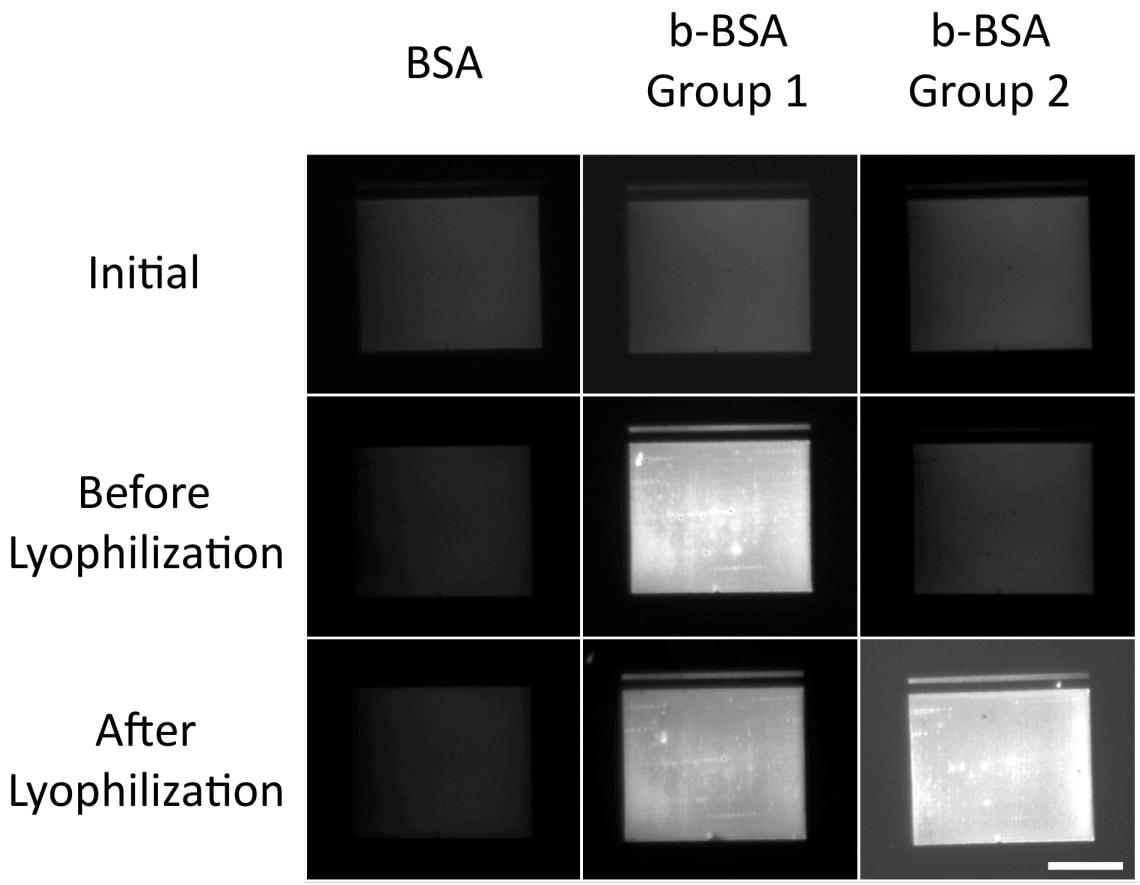

Figure 5.1 – Effect of lyophilization on biotin binding by an avidin derivative. All images are widefield fluorescence images acquired using a standard "red" filter set (Chroma 49004). Three groups of slabs were fabricated, one group of BSA slabs, and two groups of b-BSA slabs. The top row shows initial images of a representative slab from each group. The middle row shows the same blocks after the BSA slabs and b-BSA Group 1 slabs were exposed to 10 μg mL^{-1} NeutrAvidin-tetramethylrhodamine (NAv-TMR) conjugate. All groups were then lyophilized and left desiccated for 24 hours, after which all were rehydrated in HBS buffer for 18 hours. During rehydration, b-BSA Group 2 slabs were exposed to 10 μg mL^{-1} NAv-TMR. Scale bar is 20 μm.

Future work in this area will focus on examining the preservation of more intricate structures and features, including partially constrained structures of the type described in Chapter 2. Also, further studies on hydrogel functionality after lyophilization will be conducted, in some cases, using different proteins such as lysozyme. The effect of

lyophilization on the mechanical properties of MPL-fabricated hydrogels will also be examined by way of a comparison of the Young's modulus of a given hydrogel before and after lyophilization. This will provide insight into how the structures may physically change during and after lyophilization.

5.2.2 Cell experiments

Several studies that use MPL-fabricated hydrogels to alter the cellular microenvironment have been conducted in the Shear Lab [12-14]. These studies mostly focused on generating an artificial environment for cells in order to test the functionality of the materials used and/or some behavior of the cells.

A related area of particular interest to the scientific and medical communities is the study of cancer cells in controlled environments [15]. Investigators have used confining microenvironments to study cancer cell migration and gene expression to better understand metastatic behavior [16-18], due to the correlation between metastasis and cancer recurrence/mortality [19]. The ability to monitor both the gene and protein expression of a cancer cell under explicitly controlled conditions would be a valuable tool for researchers. This could lead to a better understanding of how a given cancer line propagates, spreads, and survives *in vivo*, which could potentially lead to new cancer treatment options.

The MPL fabrication techniques and hydrogel materials demonstrated in this dissertation have been used for preliminary experiments examining the migration of Neuroblastoma-Glioma (NG108) cells. PEGDA trap structures* were fabricated on a polyvinyl coverslip and plated with NG108 cells at low density ($< 5x10^4$ cells mL^{-1}).

* Trap mask design courtesy of Eric T. Ritschdorff

After 18 hours of incubation, a single cell migrated into the central chamber of the trap shown in Figure 5.2; other cells were clustered around one of the entrances.

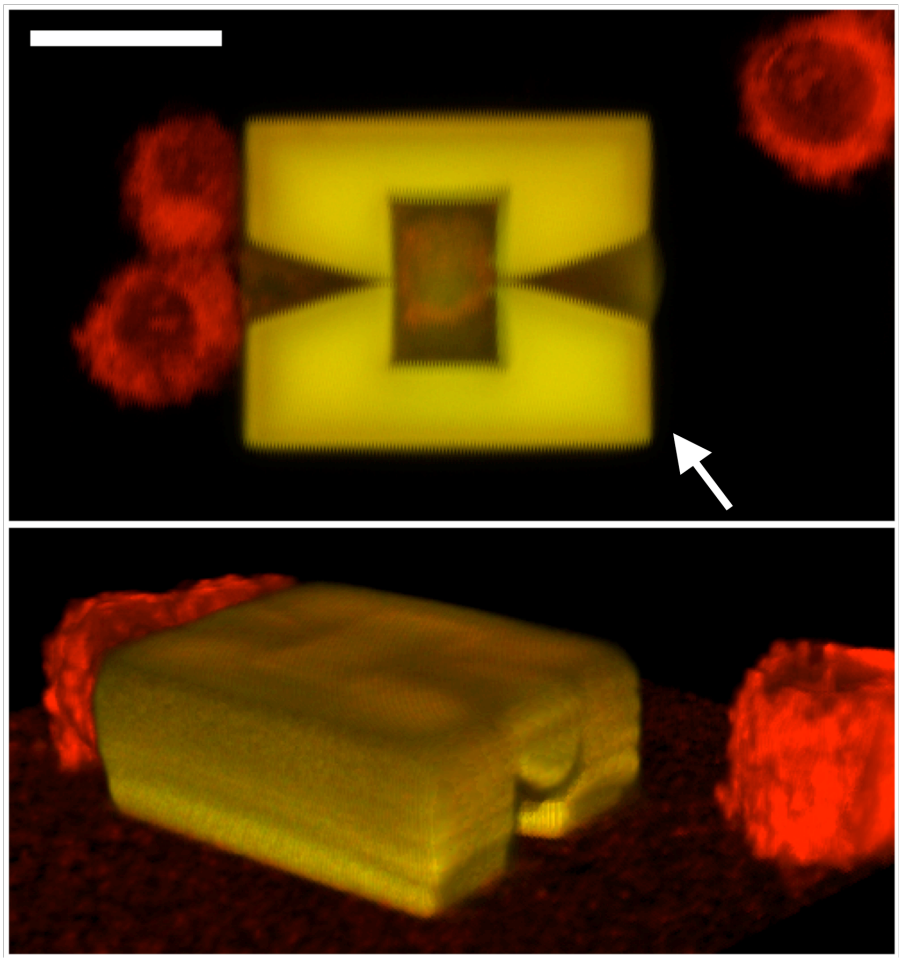

Figure 5.2 – PEGDA cell trap with NG108 cells. Cells are stained with Mitotracker Deep Red (Invitrogen, M22426). The top frame shows an optical-axis projection of a stack of confocal images, showing cells clustered around an MPL-fabricated PEGDA structure. One cell has migrated into the central cavity of the structure. The arrow shows the viewing direction of the 3D reconstruction shown in the lower frame. Scale bar is 25 μm.

These results indicate that cancer cells may be induced by the geometry of the hydrogel structures to migrate to specified locations within a structure. In future work, traps could be designed to promote cancer cell migration to locations where their

interactions with other cells or materials could be closely controlled and monitored. Work in this area has been ongoing by several members of the Shear Lab with a range of trap geometries and materials, including gelatin and BSA.

Other future work with cells will focus on potential tissue engineering applications. Structures resembling the stacked tube structure shown in Figure 2.8, with multiple layers of ~10 μm diameter tubes extending for 1 mm, will be incubated with primary cells from rat dorsal root ganglia to examine the effect of the structures on cell migration and neurite extension. Additional proteins and biomolecules such as gelatin, GMHA, and laminin will be used to fabricate the tube structures. Also, other stacked tube structures with different tube diameters and cross-sectional shapes will be fabricated to study the effect of these parameters on cell migration or neurite extension.

5.2.3 Microneedles for drug delivery

A major challenge associated with the treatment of gliomas is the efficient delivery of drugs to the cells requiring treatment [20]. Due to the general difficulties encountered when attempting to administer drugs across the blood-brain barrier, and the location of these tumors in areas with poor intrinsic circulation, delivering effective doses through traditional means is not practical. In the case of glioblastoma multiforme, a brain tumor, treatment is made even more difficult by the plasticity and motility of one of the gliomal cell types, the glioma stem cell (GSC) [21]. Although effective drugs have been developed to prevent the proliferation of GSC and the related metastasis of the tumor, these drugs are toxic to other non-cancer cells, and so must be administered locally [22]. Several alternative localized delivery methods have been proposed and tested [20, 23]; however, none of the tested solutions are both minimally invasive and biodegradable. This means that patients are more likely to experience significant inflammation at the

surgery site, which has been correlated with reduced treatment efficacy and metastasis [24]. Therefore, a microfluidic drug delivery system has been proposed that uses an array of biodegradable microneedles to deliver drugs to the glioma. Deployed on the surface of the brain, the microneedles could project into the brain tissue, terminating in the stroma of the glioma.

In a proof of concept experiment, microneedles (Figure 5.3) were fabricated using a mixture of BSA (29% w/w) and PEGDA (5% w/w) with Rose Bengal (0.5% w/w) as the photosensitizer. This solution was used to make a protogel, and a system similar to that referenced in Chapter 2 for Figures 2.8 and 2.9 was used for fabrication. The microneedle was designed with an internal channel that could be mated to channels on neighboring structures to form a microfluidic network.

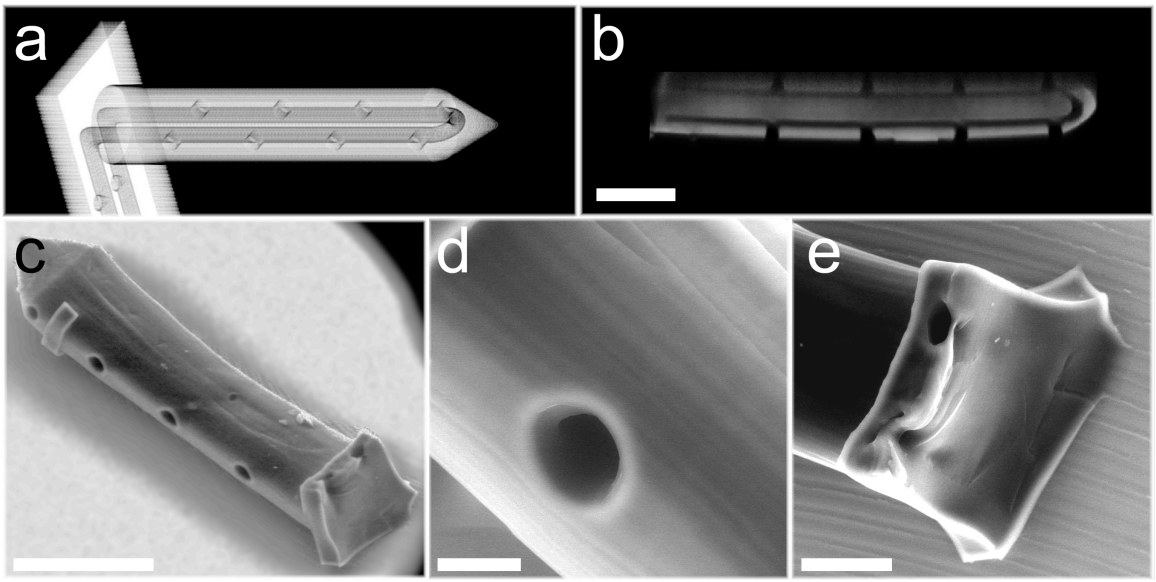

Figure 5.3 – BSA microneedle for microfluidic applications. (a) 3D projection of a stack of masks used to fabricate the microneedles. Interior channels and ports are visible. (b) Cross-section of a BSA microneedle acquired from a confocal image stack. Interior channel and ports generally appear to be open. Scale bar is 100 μm. (c) A larger microneedle; image acquired using an environmental scanning electron microscope (ESEM). Scale bar is 200 μm. (d) Detail of one of the microfluidic ports on the microneedle shown in "c." Ports appeared to be open and connected to interior channels, in accordance with the design. Scale bar is 25 μm. (e) Detail of the base of the microneedle shown in "c." Scale bar is 50 μm

In future studies, microneedles will be evaluated for mechanical and mass-transport properties using standard techniques. BSA structures made using MPL have tunable Young's moduli, dependent on laser fabrication parameters [25]. Moduli ranging from 0.03 to 3 MPa were achieved, values significantly stiffer than brain tissue. Using fixed samples, other studies will verify that microneedles made from BSA (and other potential components) can be inserted into brain tissue. Fabrication conditions will then be modified as needed. Permeability of hydrogel microstructures [14] can also be tuned by changing fabrication parameters. In some instances, it may be desirable to achieve

some drug release along the entire barrel of a needle, in which case the crosslinked hydrogel will be fabricated to allow more diffusion.

5.3 Conclusion

This dissertation demonstrates that MPL techniques have the potential to be applied to a range of biomedical research areas, including drug delivery, biosensor development, and tissue engineering. By examining a specific application – that of developing an improved peripheral nerve guide – a clearer view emerges of the required characteristics of materials used to define the cellular microenvironment. A material that physically and chemically interacts with cells on the cellular scale, as the extracellular matrix (ECM) does in tissue, is most effective for inducing cells to behave as they would *in vivo*. MPL enables the fabrication of such materials by enabling micron-scale control of scaffold topography, modulus and functionality.

5.4 References

1. Dendukuri D., Tsoi K., Hatton T.A., Doyle P.S., Controlled Synthesis of Nonspherical Microparticles Using Microfluidics. *Langmuir* **21**, 2113-2116 (2005).
2. Gratton S.E.A., Ropp P.A., Pohlhaus P.D., Luft J.C., Madden V.J., Napier M.E., DeSimone J.M., The effect of particle design on cellular internalization pathways. *Proceedings of the National Academy of Sciences* **105**, 11613-11618 (2008).
3. Venkataraman S., Hedrick J.L., Ong Z.Y., Yang C., Ee P.L.R., Hammond P.T., Yang Y.Y., The effects of polymeric nanostructure shape on drug delivery. *Advanced Drug Delivery Reviews* **63**, 1228-1246 (2011).
4. Spivey E.C., Khaing Z.Z., Shear J.B., Schmidt C.E., The fundamental role of subcellular topography in peripheral nerve repair therapies. *Biomaterials* **33**, 4264-4276 (2012).
5. Kutty J.K., Cho E., Soo Lee J., Vyavahare N.R., Webb K., The effect of hyaluronic acid incorporation on fibroblast spreading and proliferation within PEG-diacrylate based semi-interpenetrating networks. *Biomaterials* **28**, 4928-4938 (2007).
6. Larsson A., Ekblad T., Andersson O., Liedberg B., Photografted poly (ethylene glycol) matrix for affinity interaction studies. *Biomacromolecules* **8**, 287-295 (2007).

7. Zamanian B., Masaeli M., Nichol J.W., Khabiry M., Hancock M.J., Bae H., Khademhosseini A., Interface-Directed Self-Assembly of Cell-Laden Microgels. *Small* **6**, 937-944 (2010).
8. Anton E., Weskamp G., Reichardt L., Matthew W., Nerve growth factor and its low-affinity receptor promote Schwann cell migration. *Proceedings of the National Academy of Sciences* **91**, 2795 (1994).
9. Bailey S., Eichler M., Villadiego A., Rich K., The influence of fibronectin and laminin during Schwann cell migration and peripheral nerve regeneration through silicon chambers. *Journal of neurocytology* **22**, 176-184 (1993).
10. Dertinger S., Jiang X., Li Z., Murthy V., Whitesides G., Gradients of substrate-bound laminin orient axonal specification of neurons. *Proceedings of the National Academy of Sciences* **99**, 12542-12547 (2002).
11. McCarthy J., Palm S., Furcht L., Migration by haptotaxis of a Schwann cell tumor line to the basement membrane glycoprotein laminin. *Journal of Cell Biology* **97**, 772 (1983).
12. Seidlits S.K., Schmidt C.E., Shear J.B., High-Resolution Patterning of Hydrogels in Three Dimensions using Direct-Write Photofabrication for Cell Guidance. *Advanced Functional Materials* **19**, 3543-3551 (2009).
13. Kaehr B., Allen R., Javier D.J., Currie J., Shear J.B., Guiding neuronal development with in situ microfabrication. *Proceedings of the National Academy of Sciences* **101**, 16104-16108 (2004).
14. Connell J.L., Wessel A.K., Parsek M.R., Ellington A.D., Whiteley M., Shear J.B., Probing prokaryotic social behaviors with bacterial "lobster traps". *mBio* **1**, (2010).
15. Ngalim S.H., Magenau A., Le Saux G., Gooding J.J., Gaus K., How Do Cells Make Decisions: Engineering Micro- and Nanoenvironments for Cell Migration. *Journal of Oncology* **2010**, 363106 (2010).
16. Irimia D., Toner M., Spontaneous migration of cancer cells under conditions of mechanical confinement. *Integrative Biology* **1**, 506-512 (2009).
17. Rolli C.G., Seufferlein T., Kemkemer R., Spatz J.P., Impact of Tumor Cell Cytoskeleton Organization on Invasiveness and Migration: A Microchannel-Based Approach. *PLoS ONE* **5**, (2010).
18. Liu L., Sun B., Pedersen J.N., Aw Yong K.M., Getzenberg R.H., Stone H.A., Austin R.H., Probing the invasiveness of prostate cancer cells in a 3D microfabricated landscape. *Proceedings of the National Academy of Sciences* **108**, 6853-6856 (2011).
19. Chambers A.F., Goss P.E., Putative growth characteristics of micrometastatic breast cancer. *Breast cancer research : BCR* **10**, 114 (2008).
20. Lesniak M.S., Brem H., Targeted therapy for brain tumours. *Nature reviews. Drug discovery* **3**, 499-508 (2004).
21. Van Meir E.G., Hadjipanayis C.G., Norden A.D., Shu H.K., Wen P.Y., Olson J.J., Exciting New Advances in Neuro-Oncology: The Avenue to a Cure for Malignant Glioma. *CA: a cancer journal for clinicians* **60**, 166-193 (2010).

22. Bar E.E., Chaudhry A., Lin A., Fan X., Schreck K., Matsui W., Piccirillo S., Vescovi A.L., DiMeco F., Olivi A., Eberhart C.G., Cyclopamine-mediated hedgehog pathway inhibition depletes stem-like cancer cells in glioblastoma. *Stem Cells* **25**, 2524-2533 (2007).
23. Brem H., Piantadosi S., Burger P., Walker M., Selker R., Vick N., Black K., Sisti M., Brem S., Mohr G., Placebo-controlled trial of safety and efficacy of intraoperative controlled delivery by biodegradable polymers of chemotherapy for recurrent gliomas. *The Lancet* **345**, 1008-1012 (1995).
24. Balkwill F., Mantovani A., Inflammation and cancer: back to Virchow? *The Lancet* **357**, 539-545 (2001).
25. Khripin C.Y., Brinker C.J., Kaehr B., Mechanically tunable multiphoton fabricated protein hydrogels investigated using atomic force microscopy. *Soft Matter* **6**, 2842-2848 (2010).

Bibliography

Allen R., Nielson R., Wise D.D., Shear J.B., Catalytic three-dimensional protein architectures. *Analytical Chemistry* **77**, 5089-5095 (2005).

Allison D.D., Grande-Allen K.J., Review. Hyaluronan: a powerful tissue engineering tool. *Tissue Engineering* **12**, 2131-2140 (2006).

Anton E., Weskamp G., Reichardt L., Matthew W., Nerve growth factor and its low-affinity receptor promote Schwann cell migration. *Proceedings of the National Academy of Sciences* **91**, 2795 (1994).

Anton E.S., Weskamp G., Reichardt L.F., Matthew W.D., Nerve growth factor and its low-affinity receptor promote Schwann cell migration. *Proceedings of the National Academy of Sciences* **91**, 2795 (1994).

Bailey S., Eichler M., Villadiego A., Rich K., The influence of fibronectin and laminin during Schwann cell migration and peripheral nerve regeneration through silicon chambers. *Journal of neurocytology* **22**, 176-184 (1993).

Bailey S.B., Eichler M.E., Villadiego A., Rich K.M., The influence of fibronectin and laminin during Schwann cell migration and peripheral nerve regeneration through silicon chambers. *Journal of Neurocytology* **22**, 176-184 (1993).

Balkwill F., Mantovani A., Inflammation and cancer: back to Virchow? *The Lancet* **357**, 539-545 (2001).

Banerjee A., Arha M., Choudhary S., Ashton R.S., Bhatia S.R., Schaffer D.V., Kane R.S., The influence of hydrogel modulus on the proliferation and differentiation of encapsulated neural stem cells. *Biomaterials* **30**, 4695-4699 (2009).

Bar E.E., Chaudhry A., Lin A., Fan X., Schreck K., Matsui W., Piccirillo S., Vescovi A.L., DiMeco F., Olivi A., Eberhart C.G., Cyclopamine-mediated hedgehog pathway inhibition depletes stem-like cancer cells in glioblastoma. *Stem Cells* **25**, 2524-2533 (2007).

Bargiel S., Rabenorosoa K., Clévy C., Gorecki C., Lutz P., Towards micro-assembly of hybrid MOEMS components on a reconfigurable silicon free-space micro-optical bench. *Journal of Micromechanics and Microengineering* **20**, 045012 (2010).

Basu S., Campagnola P.J., Properties of crosslinked protein matrices for tissue engineering applications synthesized by multiphoton excitation. *Journal of Biomedical Materials Research Part B: Applied Biomaterials* **71**, 359-368 (2004).

Borschel G.H., Kia K.F., Kuzon W.M., Dennis R.G., Mechanical properties of acellular peripheral nerve. *Journal of Surgical Research* **114**, 133-139 (2003).

Bozkurt A., Brook G.A., Möllers S., Lassner F., Sellhaus B., Weis J., Wöltje M., Tank J., Beckmann C., Fuchs P., Damink L.O., Schügner F., Heschel I., Pallua N., In Vitro Assessment of Axonal Growth Using Dorsal Root Ganglia Explants in a Novel Three-Dimensional Collagen Matrix. *Tissue Engineering* **13**, 2971-2979 (2007).

Bozkurt A., Deumens R., Beckmann C., Olde Damink L., Schügner F., Heschel I., Sellhaus B., Weis J., Jahnen-Dechent W., Brook G.A., In vitro cell alignment

obtained with a Schwann cell enriched microstructured nerve guide with longitudinal guidance channels. *Biomaterials* **30**, 169-179 (2009).
Bozkurt A., Lassner F., O'Dey D., Deumens R., Böcker A., Schwendt T., Janzen C., Suschek C.V., Tolba R., Kobayashi E., Sellhaus B., Tholl S., Eummelen L., Schügner F., Olde Damink L., Weis J., Brook G.A., Pallua N., The role of microstructured and interconnected pore channels in a collagen-based nerve guide on axonal regeneration in peripheral nerves. *Biomaterials* **33**, 1363-1375 (2012).
Brem H., Piantadosi S., Burger P., Walker M., Selker R., Vick N., Black K., Sisti M., Brem S., Mohr G., Placebo-controlled trial of safety and efficacy of intraoperative controlled delivery by biodegradable polymers of chemotherapy for recurrent gliomas. *The Lancet* **345**, 1008-1012 (1995).
Brooks D.N., Weber R.V., Chao J.D., Rinker B.D., Zoldos J., Robichaux M.R., Ruggeri S.B., Anderson K.A., Bonatz E.E., Wisotsky S.M., Cho M.S., Wilson C., Cooper E.O., Ingari J.V., Safa B., Parrett B.M., Buncke G.M., Processed nerve allografts for peripheral nerve reconstruction: A multicenter study of utilization and outcomes in sensory, mixed, and motor nerve reconstructions. *Microsurgery* **32**, 1-14 (2011).
Brown R.A., Phillips J.B., Cell responses to biomimetic protein scaffolds used in tissue repair and engineering. *International Review of Cytology* **262**, 75-150 (2007).
Caldorera-Moore M., Kang M.K., Moore Z., Singh V., Sreenivasan S.V., Shi L., Huang R., Roy K., Swelling behavior of nanoscale, shape- and size-specific, hydrogel particles fabricated using imprint lithography. *Soft Matter* **7**, 2879-2887 (2011).
Campagnola P.J., Delguidice D.M., Epling G.A., Hoffacker K.D., Howell A.R., Pitts J.D., Goodman S.L., 3-dimensional submicron polymerization of acrylamide by multiphoton excitation of xanthene dyes. *Macromolecules* **33**, 1511-1513 (2000).
Cao J., Sun C., Zhao H., Xiao Z., Chen B., Gao J., Zheng T., Wu W., Wu S., Wang J., Dai J., The use of laminin modified linear ordered collagen scaffolds loaded with laminin-binding ciliary neurotrophic factor for sciatic nerve regeneration in rats. *Biomaterials* **32**, 3939-3948 (2011).
Carter D.C., Chang B., Ho J.X., Keeling K., Krishnasami Z., Preliminary crystallographic studies of four crystal forms of serum albumin. *European journal of biochemistry / FEBS* **226**, 1049-1052 (1994).
Chambers A.F., Goss P.E., Putative growth characteristics of micrometastatic breast cancer. *Breast cancer research : BCR* **10**, 114 (2008).
Chan V., Jeong J.H., Bajaj P., Collens M., Saif T., Kong H., Bashir R., Multi-material bio-fabrication of hydrogel cantilevers and actuators with stereolithography. *Lab on a Chip* **12**, 88 (2012).
Chatterjee K., Lin-Gibson S., Wallace W.E., Parekh S.H., Lee Y.J., Cicerone M.T., Young M.F., Simon Jr C.G., The effect of 3D hydrogel scaffold modulus on osteoblast differentiation and mineralization revealed by combinatorial screening. *Biomaterials* **31**, 5051-5062 (2010).

Clements I.P., Kim Y.-t., English A.W., Lu X., Chung A., Bellamkonda R.V., Thin-film enhanced nerve guidance channels for peripheral nerve repair. *Biomaterials* **30**, 3834-3846 (2009).

Connell J.L., Wessel A.K., Parsek M.R., Ellington A.D., Whiteley M., Shear J.B., Probing prokaryotic social behaviors with bacterial "lobster traps". *mBio* **1**, (2010).

Corey J.M., Lin D.Y., Mycek K.B., Chen Q., Samuel S., Feldman E.L., Martin D.C., Aligned electrospun nanofibers specify the direction of dorsal root ganglia neurite growth. *Journal of Biomedical Materials Research Part B: Applied Biomaterials* **83A**, 636-645 (2007).

Cowie J.M.G., Toporowski P.M., Association in the binary liquid system dymethyl sulphoxide-water. *Canadian Journal of Chemistry* **39**, 2240-2243 (1961).

Cuchiara M.P., Allen A.C.B., Chen T.M., Miller J.S., West J.L., Multilayer microfluidic PEGDA hydrogels. *Biomaterials* **31**, 5491-5497 (2010).

Culotti J.G., Kolodkin A.L., Functions of netrins and semaphorins in axon guidance. *Current Opinion in Neurobiology* **6**, 81-88 (1996).

Dendukuri D., Tsoi K., Hatton T.A., Doyle P.S., Controlled Synthesis of Nonspherical Microparticles Using Microfluidics. *Langmuir* **21**, 2113-2116 (2005).

Dertinger S., Jiang X., Li Z., Murthy V., Whitesides G., Gradients of substrate-bound laminin orient axonal specification of neurons. *Proceedings of the National Academy of Sciences* **99**, 12542-12547 (2002).

Dertinger S.K.W., Jiang X., Li Z., Murthy V.N., Whitesides G.M., Gradients of substrate-bound laminin orient axonal specification of neurons. *Proceedings of the National Academy of Sciences* **99**, 12542-12547 (2002).

Deumens R., Bozkurt A., Meek M.F., Marcus M.A.E., Joosten E.A.J., Weis J., Brook G.A., Repairing injured peripheral nerves: Bridging the gap. *Progress in Neurobiology* **92**, 245-276 (2010).

Di Leonardo R., Angelani L., Dell'Arciprete D., Ruocco G., Iebba V., Schippa S., Conte M.P., Mecarini F., De Angelis F., Di Fabrizio E., Bacterial ratchet motors. *Proceedings of the National Academy of Sciences* **107**, 9541-9545 (2010).

Dimitriadis E.K., Horkay F., Maresca J., Chadwick R.S., Determination of elastic moduli of thin layers of soft material using the atomic force microscope. *Biophysical Journal* **82**, 2798-2810 (2002).

Dodd J., Jessell T.M., Axon guidance and the patterning of neuronal projections in vertebrates. *Science* **242**, 692-699 (1988).

Dorman G., Prestwich G.D., Benzophenone photophores in biochemistry. *Biochemistry* **33**, 5661-5673 (1994).

Doyle A.D., Wang F.W., Matsumoto K., Yamada K.M., One-dimensional topography underlies three-dimensional fibrillar cell migration. *The Journal of Cell Biology* **184**, 481-490 (2009).

Du Y., Lo E., Ali S., Khademhosseini A., Directed assembly of cell-laden microgels for fabrication of 3D tissue constructs. *Proceedings of the National Academy of Sciences of the United States of America* **105**, 9522-9527 (2008).

Engler A.J., Sen S., Sweeney H.L., Discher D.E., Matrix elasticity directs stem cell lineage specification. *Cell* **126**, 677-689 (2006).

Foote C.S., Definition of type I and type II photosensitized oxidation. *Photochemistry and Photobiology* **54**, 659-659 (1991).

Forman D.S., McQuarrie I.G., Labore F.W., Wood D.K., Stone L.S., Braddock C.H., Fuchs D.A., Time course of the conditioning lesion effect on axonal regeneration. *Brain Research* **182**, 180-185 (1980).

Führmann T., Hillen L.M., Montzka K., Wöltje M., Brook G.A., Cell-Cell interactions of human neural progenitor-derived astrocytes within a microstructured 3D-scaffold. *Biomaterials* **31**, 7705-7715 (2010).

Gittard S.D., Ovsianikov A., Akar H., Chichkov B., Monteiro-Riviere N.A., Stafslien S., Chisholm B., Shin C.-C., Shih C.-M., Lin S.-J., Su Y.-Y., Narayan R.J., Two Photon Polymerization-Micromolding of Polyethylene Glycol-Gentamicin Sulfate Microneedles. *Advanced Engineering Materials* **12**, B77-B82 (2010).

Gomez N., Lu Y., Chen S., Schmidt C.E., Immobilized nerve growth factor and microtopography have distinct effects on polarization versus axon elongation in hippocampal cells in culture. *Biomaterials* **28**, 271-284 (2007).

Gratton S.E.A., Ropp P.A., Pohlhaus P.D., Luft J.C., Madden V.J., Napier M.E., DeSimone J.M., The effect of particle design on cellular internalization pathways. *Proceedings of the National Academy of Sciences* **105**, 11613-11618 (2008).

Hadjipanayi E., Mudera V., Brown R.A., Guiding cell migration in 3D: a collagen matrix with graded directional stiffness. *Cell Motility and the Cytoskeleton* **66**, 121-128 (Mar, 2009).

He X.M., Carter D.C., Atomic structure and chemistry of human serum albumin. *Nature* **358**, 209-215 (1992).

Hertz H., Ueber die Berührung fester elastischer Körpe. *Journal für die reine und angewandte Mathematik*, (1882).

Hill R.T., Shear J.B., Enzyme-Nanoparticle Functionalization of Three-Dimensional Protein Scaffolds. *Analytical Chemistry* **78**, 7022-7026 (2006).

Hoffman-Kim D., Mitchel J.A., Bellamkonda R.V., Topography, Cell Response, and Nerve Regeneration. *Annual Review of Biomedical Engineering* **12**, 203-231 (2010).

Hong Y., Krsko P., Libera M., Protein surface patterning using nanoscale PEG hydrogels. *Langmuir* **20**, 11123-11126 (2004).

Hu X., Huang J., Ye Z., Xia L., Li M., Lv B., Shen X., Luo Z., A Novel Scaffold with Longitudinally Oriented Microchannels Promotes Peripheral Nerve Regeneration. *Tissue Engineering Part A* **15**, 3297-3308 (2009).

Huang A., Liu C., Ma L., Tong Z., Lin R., Effects of clustering structure on volumetric properties of amino acids in DMSO-water mixtures. *The Journal of Chemical Thermodynamics*, 1-31 (2012).

Hudson T.W., Liu S.Y., Schmidt C.E., Engineering an improved acellular nerve graft via optimized chemical processing. *Tissue Engineering* **10**, 1346-1358 (2004).

Hudson T.W., Zawko S., Deister C., Lundy S., Hu C.Y., Lee K., Schmidt C.E., Optimized Acellular Nerve Graft Is Immunologically Tolerated and Supports Regeneration. *Tissue Engineering* **10**, 1641-1651 (2004).

Hurtado A., Cregg J.M., Wang H.B., Wendell D.F., Oudega M., Gilbert R.J., McDonald J.W., Robust CNS regeneration after complete spinal cord transection using aligned poly-l-lactic acid microfibers. *Biomaterials* **32**, 6068-6079 (2011).

Hyon S.H., Cha W.I., Ikada Y., Preparation of transparent poly(vinyl alcohol) hydrogel. *Polymer Bulletin* **22**, 119-122 (1989).

Ichihara S., Inada Y., Nakada A., Endo K., Azuma T., Nakai R., Tsutsumi S., Kurosawa H., Nakamura T., Development of New Nerve Guide Tube for Repair of Long Nerve Defects. *Tissue Engineering Part C: Methods* **15**, 387-402 (2009).

Irimia D., Toner M., Spontaneous migration of cancer cells under conditions of mechanical confinement. *Integrative Biology* **1**, 506-512 (2009).

Jhaveri S.J., McMullen J.D., Sijbesma R., Tan L.S., Zipfel W., Ober C.K., Direct three-dimensional microfabrication of hydrogels via two-photon lithography in aqueous solution. *Chemistry of Materials* **21**, 2003-2006 (2009).

Ji Y., Ghosh K., Shu X.Z., Li B., Sokolov J.C., Prestwich G.D., Clark R.A.F., Rafailovich M.H., Electrospun three-dimensional hyaluronic acid nanofibrous scaffolds. *Biomaterials* **27**, 3782-3792 (2006).

Johnson B.D., Beebe D.J., Crone W.C., Effects of swelling on the mechanical properties of a pH-sensitive hydrogel for use in microfluidic devices. *Materials Science and Engineering: C* **24**, 575-581 (2004).

Johnson K.L., *Contact mechanics*. (Cambridge University Press, 1987).

Kaehr B., Allen R., Javier D.J., Currie J., Shear J.B., Guiding neuronal development with in situ microfabrication. *Proceedings of the National Academy of Sciences* **101**, 16104-16108 (2004).

Kaehr B., Shear J.B., Mask-directed multiphoton lithography. *Journal of the American Chemical Society* **129**, 1904 (2007).

Kehoe S., Zhang X.F., Boyd D., FDA approved guidance conduits and wraps for peripheral nerve injury: A review of materials and efficacy. *Injury* (in press), 1-20 (2011).

Kershner R.J., Bozano L.D., Micheel C.M., Hung A.M., Fornof A.R., Cha J.N., Rettner C.T., Bersani M., Frommer J., Rothemund P.W.K., Wallraff G.M., Placement and orientation of individual DNA shapes on lithographically patterned surfaces. *Nature Nanotechnology* **4**, 557-561 (2009).

Khripin C.Y., Brinker C.J., Kaehr B., Mechanically tunable multiphoton fabricated protein hydrogels investigated using atomic force microscopy. *Soft Matter* **6**, 2842-2848 (2010).

Khripin C.Y., Pristinski D., Dunphy D.R., Brinker C.J., Kaehr B., Protein-Directed Assembly of Arbitrary Three-Dimensional Nanoporous Silica Architectures. *ACS Nano* **5**, 1401-1409 (2011).

Klaassen E.H., Petersen K., Noworolski J.M., Logan J., Maluf N.I., Brown J., Storment C., McCulley W., Kovacs G.T.A., Silicon fusion bonding and deep reactive ion

etching: a new technology for microstructures. *Sensors and Actuators A: Physical* **52**, 132-139 (1996).

Kostic A., Sap J., Sheetz M.P., RPTPalpha is required for rigidity-dependent inhibition of extension and differentiation of hippocampal neurons. *Journal of Cell Science* **120**, 3895-3904 (2007).

Krych A.J., Rooney G.E., Chen B., Schermerhorn T.C., Ameenuddin S., Gross L., Moore M.J., Currier B.L., Spinner R.J., Friedman J.A., Yaszemski M.J., Windebank A.J., Relationship between scaffold channel diameter and number of regenerating axons in the transected rat spinal cord. *Acta Biomaterialia* **5**, 2551-2559 (2009).

Kuan C.Y.K., Tannahill D., Cook G.M.W., Keynes R.J., Somite polarity and segmental patterning of the peripheral nervous system. *Mechanisms of Development* **121**, 1055-1068 (2004).

Kuebler S.M., Rumi M., Watanabe T., Braun K., Cumpston B.H., Heikal A.A., Erskine L.L., Thayumanavan S., Barlow S., Marder S.R., Perry J.W., Optimizing Two-Photon Initiators and Exposure Conditions for Three-Dimensional Lithographic Microfabrication. *Journal of Photopolymer Science and Technology* **14**, 657-668 (2001).

Kutty J.K., Cho E., Soo Lee J., Vyavahare N.R., Webb K., The effect of hyaluronic acid incorporation on fibroblast spreading and proliferation within PEG-diacrylate based semi-interpenetrating networks. *Biomaterials* **28**, 4928-4938 (2007).

Lai J.T.W., Lau F.W., Robb D., Westh P., Nielsen G., Trandum C., Hvidt A., Koga Y., Excess partial molar enthalpies, entropies, Gibbs energies, and volumes in aqueous dimethylsulfoxide. *Journal of Solution Chemistry* **24**, 89-102 (1995).

Larsson A., Ekblad T., Andersson O., Liedberg B., Photografted poly (ethylene glycol) matrix for affinity interaction studies. *Biomacromolecules* **8**, 287-295 (2007).

Leach J., Schmidt C., Austin T., Photocrosslinkable Hyaluronic Acid Hydrogels for Tissue Engineering. *Materials Research Society Symposium Proceedings*, (2004).

Leach J.B., Bivens K.A., Patrick C.W., Schmidt C.E., Photocrosslinked hyaluronic acid hydrogels: Natural, biodegradable tissue engineering scaffolds. *Biotechnology and Bioengineering* **82**, 578-589 (2003).

Leach J.B., Bivens K.A., Collins C.N., Schmidt C.E., Development of photocrosslinkable hyaluronic acid-polyethylene glycol-peptide composite hydrogels for soft tissue engineering. *Journal of Biomedical Materials Research Part B: Applied Biomaterials* **70**, 74-82 (2004).

Leach J.B., Schmidt C.E., Characterization of protein release from photocrosslinkable hyaluronic acid-polyethylene glycol hydrogel tissue engineering scaffolds. *Biomaterials* **26**, 125-135 (2005).

Leach J.B., Brown X.Q., Jacot J.G., Dimilla P.A., Wong J.Y., Neurite outgrowth and branching of PC12 cells on very soft substrates sharply decreases below a threshold of substrate rigidity. *Journal of Neural Engineering* **4**, 26-34 (2007).

LeBel R.G., Goring D.A.I., Density, Viscosity, Refractive Index, and Hygroscopicity of Mixtures of Water and Dimethyl Sulfoxide. *Journal of Chemical & Engineering Data* **7**, 100-101 (1962).

Lee S.-H., Moon J.J., West J.L., Three-dimensional micropatterning of bioactive hydrogels via two-photon laser scanning photolithography for guided 3D cell migration. *Biomaterials* **29**, 2962-2968 (2008).
Lesniak M.S., Brem H., Targeted therapy for brain tumours. *Nature reviews. Drug discovery* **3**, 499-508 (2004).
Li L., Gattass R.R., Gershgoren E., Hwang H., Fourkas J.T., Achieving λ/20 Resolution by One-Color Initiation and Deactivation of Polymerization. *Science*, (2009).
Lin C.-L., Vitrant G., Bouriau M., Casalegno R., Baldeck P.L., Optically driven Archimedes micro-screws for micropump application. *Optics Express* **19**, 8267-8276 (2011).
Lin D.C., Dimitriadis E.K., Horkay F., Elasticity of rubber-like materials measured by AFM nanoindentation. *eXPRESS Polymer Letters* **1**, 576-584 (2007).
Liu L., Sun B., Pedersen J.N., Aw Yong K.M., Getzenberg R.H., Stone H.A., Austin R.H., Probing the invasiveness of prostate cancer cells in a 3D microfabricated landscape. *Proceedings of the National Academy of Sciences* **108**, 6853-6856 (2011).
Lohmeyer J.A., Shen Z.L., Walter G.F., Berger A., Bridging extended nerve defects with an artifcial nerve graft containing Schwann cells pre-seeded on polyglactin filaments. *International journal of artificial organs* **30**, 64-74 (2007).
Long Y., Zhang N., Huang Y., Wen X., Formation of Highly Aligned Grooves on Inner Surface of Semipermeable Hollow Fiber Membrane for Directional Axonal Outgrowth. *Journal of Manufacturing Science and Engineering* **130**, 021011 (2008).
Lu X., Richardson P.M., Inflammation near the nerve cell body enhances axonal regeneration. *The Journal of Neuroscience* **11**, 972-978 (1991).
Maruo S., Nakamura O., Kawata S., Three-dimensional microfabrication with two-photon-absorbed photopolymerization. *Optics letters* **22**, 132-134 (1997).
Maruo S., Ikuta K., Three-dimensional microfabrication by use of single-photon-absorbed polymerization. *Applied Physics Letters* **76**, 2656 (2000).
Maruo S., Ikuta K. Fabrication of freely movable microstructures by using two-photon three-dimensional microfabrication. *Proceedings of SPIE* **3937,** 106-112 (2000).
McCarthy J., Palm S., Furcht L., Migration by haptotaxis of a Schwann cell tumor line to the basement membrane glycoprotein laminin. *Journal of Cell Biology* **97**, 772 (1983).
McCarthy J.B., Palm S.L., Furcht L.T., Migration by haptotaxis of a Schwann cell tumor line to the basement membrane glycoprotein laminin. *Journal of Cell Biology* **97**, 772 (1983).
Miller J.S., Shen C.J., Legant W.R., Baranski J.D., Blakely B.L., Chen C.S., Bioactive hydrogels made from step-growth derived PEG-peptide macromers. *Biomaterials* **31**, 3736-3743 (2010).
Möllers S., Heschel I., Damink L.H.H.O., Schügner F., Deumens R., Müller B., Bozkurt A., Nava J.G., Noth J., Brook G.A., Cytocompatibility of a Novel, Longitudinally

Microstructured Collagen Scaffold Intended for Nerve Tissue Repair. *Tissue Engineering Part A* **15**, 461-472 (2009).
Moore S.W., Sheetz M.P., Biophysics of substrate interaction: Influence on neural motility, differentiation, and repair. *Developmental Neurobiology* **71**, 1090-1101 (2011).
Nakamura T., Inada Y., Fukuda S., Yoshitani M., Nakada A., Itoi S.-i., Kanemaru S.-i., Endo K., Shimizu Y., Experimental study on the regeneration of peripheral nerve gaps through a polyglycolic acid-collagen (PGA-collagen) tube. *Brain Research* **1027**, 18-29 (2004).
Ngalim S.H., Magenau A., Le Saux G., Gooding J.J., Gaus K., How Do Cells Make Decisions: Engineering Micro- and Nanoenvironments for Cell Migration. *Journal of Oncology* **2010**, 363106 (2010).
Nguyen Q.T., Sanes J.R., Lichtman J.W., Pre-existing pathways promote precise projection patterns. *Nature Neuroscience* **5**, 861-867 (2002).
Nielson R., Kaehr B., Shear J.B., Microreplication and Design of Biological Architectures Using Dynamic-Mask Multiphoton Lithography. *Small* **5**, 120-125 (2009).
Norman L.L., Aranda-Espinoza H., Cortical Neuron Outgrowth is Insensitive to Substrate Stiffness. *Cellular and Molecular Bioengineering* **3**, 398-414 (2010).
Nowatzki P.J., Franck C., Maskarinec S.A., Ravichandran G., Tirrell D.A., Mechanically tunable thin films of photosensitive artificial proteins: preparation and characterization by nanoindentation. *Macromolecules* **41**, 1839-1845 (2008).
Park K., Effect of shape and size of polymer particles on cellular internalization. *Journal of controlled release : official journal of the Controlled Release Society* **147**, 313 (Nov 1, 2010).
Park Y.D., Tirelli N., Hubbell J.A., Photopolymerized hyaluronic acid-based hydrogels and interpenetrating networks. *Biomaterials* **24**, 893-900 (2003).
Parker R.J., Auld V.J., Signaling in glial development: differentiation migration and axon guidance. *Biochemistry and Cell Biology* **82**, 694-707 (2004).
Peppas N.A., Keys K.B., Torres-Lugo M., Lowman A.M., Poly (ethylene glycol)-containing hydrogels in drug delivery. *Journal of Controlled Release* **62**, 81-87 (1999).
Perry V.H., Brown M.C., Gordon S., The macrophage response to central and peripheral nerve injury. A possible role for macrophages in regeneration. *The Journal of Experimental Medicine* **165**, 1218-1223 (1987).
Pitts J., Howell A., Taboada R., Banerjee I., Wang J., Goodman S., Campagnola P., New Photoactivators for Multiphoton Excited Three-dimensional Submicron Cross-linking of Proteins: Bovine Serum Albumin and Type 1 Collagen. *Photochemistry and Photobiology* **76**, 135-144 (2002).
Ramon y Cajal S., *Histology of the nervous system of man and the vertebrates*. (Oxford University Press, New York, 1995), vol. 1. orig. pub. 1892, trans. N. Swanson, L. Swanson.

Revzin A., Russell R.J., Yadavalli V.K., Koh W.-G., Deister C., Hile D.D., Mellott M.B., Pishko M.V., Fabrication of Poly(ethylene glycol) Hydrogel Microstructures Using Photolithography. *Langmuir* **17**, 5440-5447 (2001).

Richardson P.M., Issa V.M., Peripheral injury enhances central regeneration of primary sensory neurones. *Nature* **309**, 791-793 (1984).

Richardson P.M., Verge V.M.K., Axonal regeneration in dorsal spinal roots is accelerated by peripheral axonal transection. *Brain Research* **411**, 406-408 (1987).

Ritschdorff E.T., Shear J.B., Multiphoton Lithography Using a High-Repetition Rate Microchip Laser. *Analytical Chemistry* **82**, 8733-8737 (2010).

Ritschdorff E.T., Nielson R., Shear J.B., Multi-focal multiphoton lithography. *Lab on a Chip* **12**, 867-871 (2012).

Rolli C.G., Seufferlein T., Kemkemer R., Spatz J.P., Impact of Tumor Cell Cytoskeleton Organization on Invasiveness and Migration: A Microchannel-Based Approach. *PLoS ONE* **5**, (2010).

Rundqvist J., Hoh J.H., Haviland D.B., Directed immobilization of protein-coated nanospheres to nanometer-scale patterns fabricated by electron beam lithography of poly (ethylene glycol) self-assembled monolayers. *Langmuir* **22**, 5100-5107 (2006).

Saha K., Keung A.J., Irwin E.F., Li Y., Little L., Schaffer D.V., Healy K.E., Substrate modulus directs neural stem cell behavior. *Biophysical Journal* **95**, 4426-4438 (2008).

Schlosshauer B., Dreesmann L., Schaller H.-E., Sinis N., Synthetic Nerve Guide Implants in Humans: A Comprehensive Survey. *Neurosurgery* **59**, 740-748 (2006).

Schmidt C.E., Leach J.B., Neural tissue engineering: Strategies for repair and regeneration. *Annual Review of Biomedical Engineering* **5**, 293-347 (2003).

Schoof H., Apel J.r., Heschel I., Rau G.n., Control of pore structure and size in freeze-dried collagen sponges. *Journal of Biomedical Materials Research Part B: Applied Biomaterials* **58**, 352-357 (2001).

Seidlits S.K., Schmidt C.E., Shear J.B., High-Resolution Patterning of Hydrogels in Three Dimensions using Direct-Write Photofabrication for Cell Guidance. *Advanced Functional Materials* **19**, 3543-3551 (2009).

Seidlits S.K., Khaing Z.Z., Petersen R.R., Nickels J.D., Vanscoy J.E., Shear J.B., Schmidt C.E., The effects of hyaluronic acid hydrogels with tunable mechanical properties on neural progenitor cell differentiation. *Biomaterials* **31**, 3930-3940 (2010).

Sharma G., Valenta D.T., Altman Y., Harvey S., Xie H., Mitragotri S., Smith J.W., Polymer particle shape independently influences binding and internalization by macrophages. *Journal of Controlled Release* **147**, 408-412 (2010).

Shear J.B., Multiphoton-excited fluorescence in bioanalytical chemistry. *Analytical Chemistry* **71**, 598A-605A (1999).

Shen H.R., Spikes J.D., Kopečeková P., Kopeček J., Photodynamic crosslinking of proteins. I. Model studies using histidine-and lysine-containing N-(2-hydroxypropyl) methacrylamide copolymers. *Journal of Photochemistry and Photobiology B: Biology* **34**, 203-210 (1996).

Shen H.R., Spikes J.D., Smith C.J., Kopeček J., Photodynamic cross-linking of proteins V. Nature of the tyrosine,Äìtyrosine bonds formed in the FMN-sensitized intermolecular cross-linking of N-acetyl-l-tyrosine. *Journal of Photochemistry & Photobiology, A: Chemistry* **133**, 115-122 (2000).

Shen H.R., Spikes J.D., Smith C.J., Kopeček J., Photodynamic cross-linking of proteins IV. Nature of the His-His bond (s) formed in the rose bengal-photosensitized cross-linking of N-benzoyl-L-histidine. *Journal of Photochemistry & Photobiology, A: Chemistry* **130**, 1-6 (2000).

Smeal R.M., Rabbitt R., Biran R., Tresco P.A., Substrate Curvature Influences the Direction of Nerve Outgrowth. *Annals of Biomedical Engineering* **33**, 376-382 (2005).

Sokolov A., Apodaca M.M., Grzybowski B.A., Aranson I.S., Swimming bacteria power microscopic gears. *Proceedings of the National Academy of Sciences of the United States of America* **107**, 969-974 (2010).

Sondell M., Lundborg G., Kanje M., Regeneration of the rat sciatic nerve into allografts made acellular through chemical extraction. *Brain Research* **795**, 44-54 (1998).

Soper A.K., Luzar A., Orientation of Water Molecules around Small Polar and Nonpolar Groups in Solution - A Neutron Diffraction and Computer Simulation Study. *The Journal of Physical Chemistry* **100**, 1357-1367 (1996).

Spikes J.D., Shen H.R., Kopečeková P., Kopeček J., Photodynamic crosslinking of proteins. III. Kinetics of the FMN- and rose bengal-sensitized photooxidation and intermolecular crosslinking of model tyrosine-containing N-(2-Hydroxypropyl) methacrylamide copolymers. *Photochemistry and Photobiology* **70**, 130-137 (1999).

Spivey E.C., Khaing Z.Z., Shear J.B., Schmidt C.E., The fundamental role of subcellular topography in peripheral nerve repair therapies. *Biomaterials* **33**, 4264-4276 (2012).

Sunderland I.R.P., Brenner M.J., Singham J., Rickman S.R., Hunter D.A., Mackinnon S.E., Effect of Tension on Nerve Regeneration in Rat Sciatic Nerve Transection Model. *Annals of Plastic Surgery* **53**, 382 (2004).

Sunderland S., A classification of peripheral nerve injuries producing loss of function. *Brain : a journal of neurology* **74**, 491-516 (1951).

Suri S., Han L.-H., Zhang W., Singh A., Chen S., Schmidt C.E., Solid freeform fabrication of designer scaffolds of hyaluronic acid for nerve tissue engineering. *Biomedical Microdevices*, **13**, 983-993 (2011).

Temenoff J.S., Athanasiou K.A., Lebaron R.G., Mikos A.G., Effect of poly (ethylene glycol) molecular weight on tensile and swelling properties of oligo (poly (ethylene glycol) fumarate) hydrogels for cartilage tissue engineering. *Journal of Biomedical Materials Research Part B: Applied Biomaterials* **59**, 429-437 (2002).

Toba T., Nakamura T., Shimizu Y., Matsumoto K., Ohnishi K., Fukuda S., Yoshitani M., Ueda H., Hori Y., Endo K., Regeneration of canine peroneal nerve with the use of a polyglycolic acid-collagen tube filled with laminin-soaked collagen sponge: a comparative study of collagen sponge and collagen fibers as filling materials for

nerve conduits. *Journal of Biomedical Materials Research Part B: Applied Biomaterials* **58**, 622-630 (2001).
Van Meir E.G., Hadjipanayis C.G., Norden A.D., Shu H.K., Wen P.Y., Olson J.J., Exciting New Advances in Neuro-Oncology: The Avenue to a Cure for Malignant Glioma. *CA: a cancer journal for clinicians* **60**, 166-193 (2010).
Venkataraman S., Hedrick J.L., Ong Z.Y., Yang C., Ee P.L.R., Hammond P.T., Yang Y.Y., The effects of polymeric nanostructure shape on drug delivery. *Advanced Drug Delivery Reviews* **63**, 1228-1246 (2011).
Wang G.Y., Hirai K.I., Shimada H., The Role of Laminin, a Component of Schwann-Cell Basal Lamina, in Rat Sciatic-Nerve Regeneration Within Antiserum-Treated Nerve Grafts. *Brain Research* **570**, 116-125 (1992).
Wangensteen K.J., Kalliainen L.K., Collagen Tube Conduits in Peripheral Nerve Repair: A Retrospective Analysis. *Hand* **5**, 273-277 (2009).
Whitlock E.L., Tuffaha S.H., Luciano J.P., Yan Y., Hunter D.A., Magill C.K., Moore A.M., Tong A.Y., Mackinnon S.E., Borschel G.H., Processed allografts and type I collagen conduits for repair of peripheral nerve gaps. *Muscle & Nerve* **39**, 787-799 (2009).
Wosnick J.H., Shoichet M.S., Three-dimensional Chemical Patterning of Transparent Hydrogels. *Chemistry of Materials* **20**, 55-60 (2008).
Wu D., Chen Q.-D., Niu L.-G., Wang J.-N., Wang J., Wang R., Xia H., Sun H.-B., Femtosecond laser rapid prototyping of nanoshells and suspending components towards microfluidic devices. *Lab on a Chip* **9**, 2391 (2009).
Wylie R.G., Ahsan S., Aizawa Y., Maxwell K.L., Morshead C.M., Shoichet M.S., Spatially controlled simultaneous patterning of multiple growth factors in three-dimensional hydrogels. *Nature Materials* **10**, 799-806 (2011).
Yamada A., Niikura F., Ikuta K., A three-dimensional microfabrication system for biodegradable polymers with high resolution and biocompatibility. *Journal of Micromechanics and Microengineering* **18**, (2008).
Yao L., de Ruiter G.C.W., Wang H., Knight A.M., Spinner R.J., Yaszemski M.J., Windebank A.J., Pandit A., Controlling dispersion of axonal regeneration using a multichannel collagen nerve conduit. *Biomaterials* **31**, 5789-5797 (2010).
Yoshii S., Oka M., Shima M., Taniguchi A., Akagi M., Bridging a 30-mm nerve defect using collagen filaments. *Journal of Biomedical Materials Research Part B: Applied Biomaterials* **67A**, 467-474 (2003).
Zamanian B., Masaeli M., Nichol J.W., Khabiry M., Hancock M.J., Bae H., Khademhosseini A., Interface-Directed Self-Assembly of Cell-Laden Microgels. *Small* **6**, 937-944 (2010).
Zawko S.A., Schmidt C.E., Crystal templating dendritic pore networks and fibrillar microstructure into hydrogels. *Acta Biomaterialia* **6**, 2415-2421 (2010).

Vita

Eric Spivey grew up in Charleston, South Carolina. His academic interests led him to attend the South Carolina Governor's School for Science and Mathematics, where the curriculum encouraged active and early participation in scientific research. Through this curriculum, he was introduced to Prof. Kathryn Meier at the Medical University of South Carolina, who served as his mentor and inspired him to continue in research.

Eric attended Duke University, where he earned a Bachelor of Science in Biomedical Engineering, and studied under the supervision of Prof. George Truskey. He attended Duke on an Army ROTC scholarship, and upon graduation was commissioned in the Army Medical Service Corps (MSC), and entered active duty.

After attending the MSC Officer Basic Course, Eric was selected for flight training, after which he served as a MEDEVAC pilot and team leader at Ft. Benning, Georgia. He deployed to Bosnia for a peacekeeping tour, and then returned to the US for training as a maintenance manager and UH-60A (Blackhawk) maintenance test pilot. He was assigned to Wiesbaden, Germany as the Maintenance Platoon Leader of the 159th Medical Company (Air Ambulance). He deployed with his company to Kuwait at the beginning of Operation Iraqi Freedom and served 11 months in combat in and around Baghdad, supporting the life-saving MEDEVAC mission there.

Completing his service commitment, Eric moved to Austin, Texas, where he began this research and, more importantly, met and fell in love with his future wife. They now have a son, and he is awesome. That is all.

Permanent email address: eric.spivey@gmail.com

This dissertation was typed by the author